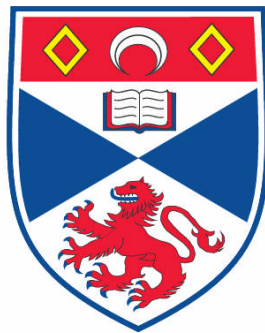


NANOMATERIALS FOR ENERGY STORAGE

Feng Jiao

**A Thesis Submitted for the Degree of PhD
at the
University of St. Andrews**



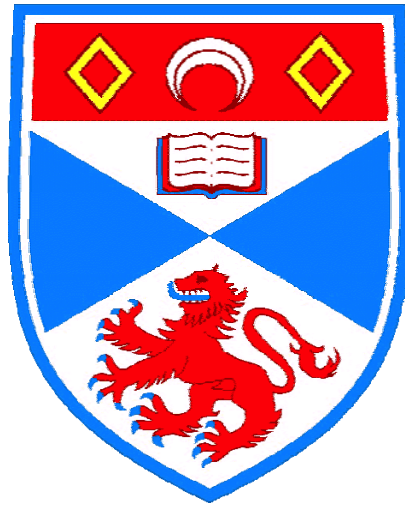
2008

**Full metadata for this item is available in the St Andrews
Digital Research Repository
at:
<https://research-repository.st-andrews.ac.uk/>**

**Please use this identifier to cite or link to this item:
<http://hdl.handle.net/10023/487>**

This item is protected by original copyright

**This item is licensed under a
[Creative Commons License](#)**



Nanomaterials for Energy Storage

A Thesis presented for the degree of
Doctor of Philosophy
in the Faculty of Science of the University of St. Andrews
by Feng Jiao

September 2007

School of Chemistry
St. Andrews

Declaration

I, Feng Jiao, hereby certify that this thesis, which is approximately 29, 600 words in length, has been written by me, that it is the record of work carried out by me and that it has not been submitted in any previous application for a higher degree.

Date..... Signature of Candidate.....

I was admitted as a research student in January 2004 and as a candidate for the degree of Doctor of Philosophy in January 2005; the higher study for which this is a record was carried out in the University of St. Andrews between 2004 and 2007.

Date..... Signature of Candidate.....

Certification

I hereby certify that the candidate has fulfilled the conditions of the Resolution and Regulations appropriate for the degree of Doctor of Philosophy in the University of St. Andrews and that the candidate is qualified to submit this thesis in application for that degree.

Date..... Signature of Supervisor.....

Library Declaration

In submitting this thesis to the University of St. Andrews I understand that I am giving permission for it to be made available for use in accordance with the regulations of the University Library for the time being in Force, subject to any copyright vested in the work not being affected thereby. I also understand that the title and the abstract will be published, and that a copy of the work of the work may be made and supplied to any *bona fide* library or research worker.

Date.....

Signature of Candidate.....

Acknowledgements

I would like to thank my supervisor, Prof. Peter Bruce, for his invaluable ideas and guidance throughout the work, which are essential to make this thesis possible.

I express special thanks to Prof. Andrew Harrison, Prof. Alan Chadwick, and Prof. Jean-Claude Jumas for their idea and time to collaborate on the work presented in this thesis.

Thanks to all the people who help me on many things: Mrs. Sylvia Williamson for measuring nitrogen adsorption and chemical analysis, Dr. Aurelie Debart for demonstrating the assembly of coin and Swagelok type cells, Mr. Adrian Hill for collecting SQUID and neutron data, and other people in PGB group for their help.

Also, I would like to thank my friends, Dr. Zhuojia Lin, Ms. Jianli Bao, Mrs. Li Meng and Mr. Dengke Xiao, who have made my time at St Andrews so enjoyable.

Finally I would like to thank my family, especially my wife, Lingzhen Wang, for their understanding, support and love, to make all these possible.

Contents	Page
Abstract	i-ii
Chapter 1. Introduction	1-24
Chapter 2. Routine experiments and characterization techniques	25-35
Chapter 3. Synthesis, characterization, and magnetic properties of mesoporous iron oxides with amorphous walls	36-45
Chapter 4. Synthesis, characterization, and magnetic properties of mesoporous transition metal oxides prepared by the hard template method	46-77
Chapter 5. Electrochemical properties of nanowire and mesoporous transition metal oxides with crystalline walls	78-94
Chapter 6. Characterization of mesoporous materials synthesized by post-templating method	95-121
Chapter 7. Ordered three-dimensional arrays of monodispersed Mn_3O_4 nanoparticles with a core-shell structure	122-132
Chapter 8. Conclusions	133-134
Publication list	I
List of Abbreviations and Acronyms	II

Abstract

The results presented in this thesis demonstrate the first synthesis of several nanostructured transition metal oxides and lithium containing transition metal oxides. Their uses in lithium-ion batteries and/or as magnetic materials have been investigated.

The first example of two and three dimensional mesoporous Fe_2O_3 has been prepared by using the soft templating (surfactant) method. The materials have amorphous walls and exhibit superparamagnetic behaviour.

By using a hard template route, a mesoporous $\alpha\text{-Fe}_2\text{O}_3$ with highly crystalline walls has been synthesized. Its unique magnetic behaviour, distinct from bulk $\alpha\text{-Fe}_2\text{O}_3$, nanoparticulate $\alpha\text{-Fe}_2\text{O}_3$, and mesoporous Fe_2O_3 with disordered walls, has been demonstrated.

The hard template method was also used to prepare nanowire and mesoporous Co_3O_4 , $\beta\text{-MnO}_2$ and Mn_2O_3 with crystalline walls. Their electrochemical properties as electrodes in Li-ion batteries have been investigated. Mesoporous $\beta\text{-MnO}_2$ can accommodate 0.9 Li/Mn in stark contrast to bulk $\beta\text{-MnO}_2$ which cannot accommodate Li.

To prepare mesoporous materials which cannot be obtained directly by the hard template method, a post-templating route has been developed. Mesoporous Fe_3O_4 , $\gamma\text{-Fe}_2\text{O}_3$, and Mn_3O_4 with ordered mesostructures and highly crystalline walls have been obtained by post-synthesis reduction/oxidation treatments. All the materials show unique magnetic properties compared with nanoparticulate and bulk materials.

Also, the first example of lithium containing mesoporous material, LT-LiCoO₂, was synthesized by first preparing mesoporous Co_3O_4 , then reacting this with LiOH to form LT-LiCoO₂, with retention of the ordered nanostructure. The nanostructured LT-LiCoO₂ compounds demonstrate superior performance compared with normal or nanoparticulate LT-LiCoO₂, when used as intercalation electrodes in lithium batteries.

Finally, monodispersed Mn_3O_4 nanoparticles (diameter ~ 8 nm) with a core-shell structure (a highly crystalline Mn_3O_4 core encased in a thin MnO_2 shell) have been prepared for the first time. Ordered three-dimensional arrays form by spontaneous self-assembly. Magnetic measurements demonstrated that the self-assembled three-dimensional arrays exhibit spin-glass behaviour, rather than the anticipated

superparamagnetic behaviour for isolated nanoparticles. Such behaviour is interpreted as arising from strong interactions between the core (crystallized Mn_3O_4) and shell (MnO_2).

Chapter 1. Introduction

1-1 Mesoporous solids

1-1-1 General introduction into mesoporous solids

Mesoporous materials belong to the wider class of nanostructured materials. They are composed of nano-sized pores (pore size from 2 to 50 nm) between which are thin walls (typical thickness below 10 nm).¹ The first ordered mesoporous silica material MCM-41 was reported by the Mobil Company in 1992, which has two-dimensional hexagonal packed pores without any connection between them (Figure 1).^{2,3} It has a typical pore size (pore diameter determined by N₂ sorption analysis) of ~ 2.5 nm and a wall thickness ~ 1.8 nm. The BET specific surface area and pore volume determined by sorption measurements are ~ 1000 m²/g and ~ 0.9 cm³/g, which are significantly larger than bulk materials. Because of the large internal surface area and pore volume, MCM-41 is important in many fields, such as catalysis, gas storage, and molecular filters.⁴⁻⁶ However, the ultra thin wall thickness (below 2 nm) results in an unstable pore structure for practice proposes, especially in catalytic reactions. A thick wall (high stability) is important in overcoming this deficiency.

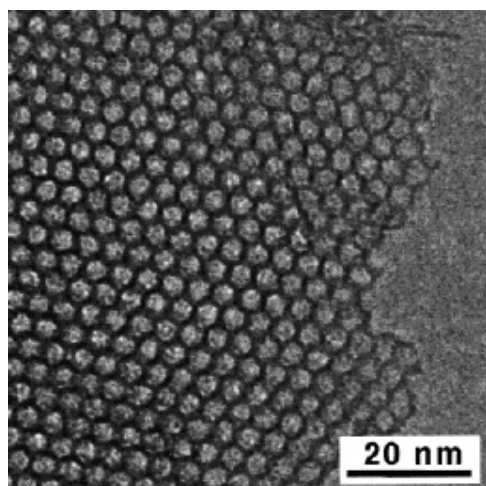


Figure 1. A typical TEM image of MCM-41.

In 1998, GD Stucky's group prepared a new mesoporous silica SBA-15, which not only has better thermal stability, due to thicker walls (~ 3.5 nm) but also larger pores, with a typical size 8 nm.⁷ This material has a hexagonal packed one-dimensional mesoporous structure (Figure 2), similar to the pore structure of MCM-41, as well as some disordered small pores (micropores) between the main

pores, resulting in a 3D pore network. This is because part of polymer template (P123 which was used in SBA-15 preparation) became embedded into the silica walls during the self-assembly process. On its removal by calcination at high temperature, micropores were created. Such microporosity had influences on the structure of replica mesopores cast from SBA-15. This will be discussed in the hard template method section.

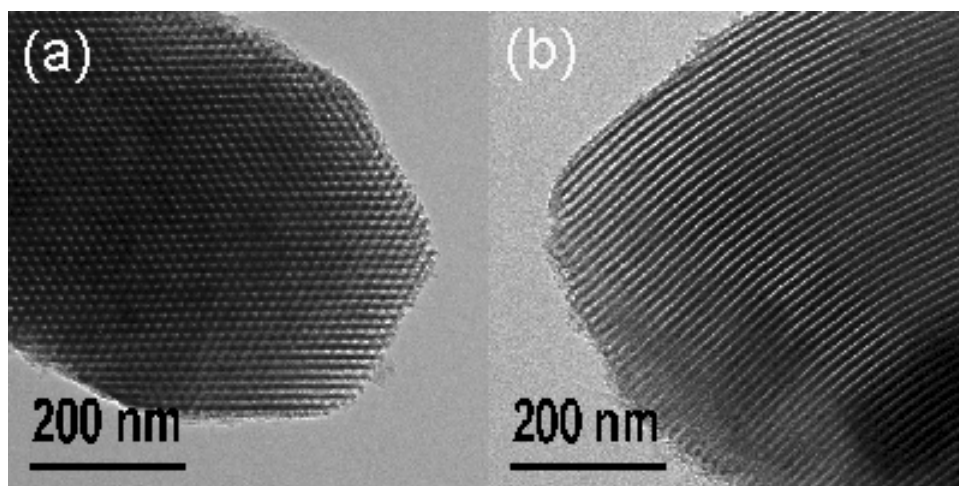


Figure 2. TEM images of SBA-15 recorded along (a) [001] and (b) [110] directions.

In addition to the stability of mesostructure, the accessibility of the internal surface area is also important. One way to achieve this is to create three-dimensional rather than one-dimensional (e.g. MCM-41 and SBA-15) mesopores so that even if some pores are blocked, others are available. Recently, a group in Korea has successfully synthesized three-dimensional mesoporous silica (KIT-6) in a butanol-water-polymer system.⁸ A typical TEM image and pore structure model for KIT-6 are shown in Figure 3.^{9, 10} This material has thick walls (~ 4 nm), a large surface area (~ 800 m²/g), large pore size (~ 7 nm) and a 3D bi-continuous pore network. Due to these superior properties, mesoporous KIT-6, which exhibits good stability, may be a good candidate for many applications, such as high temperature catalysis, large molecule separation, and as a hard template, with which to synthesize other mesopores.^{9, 10}

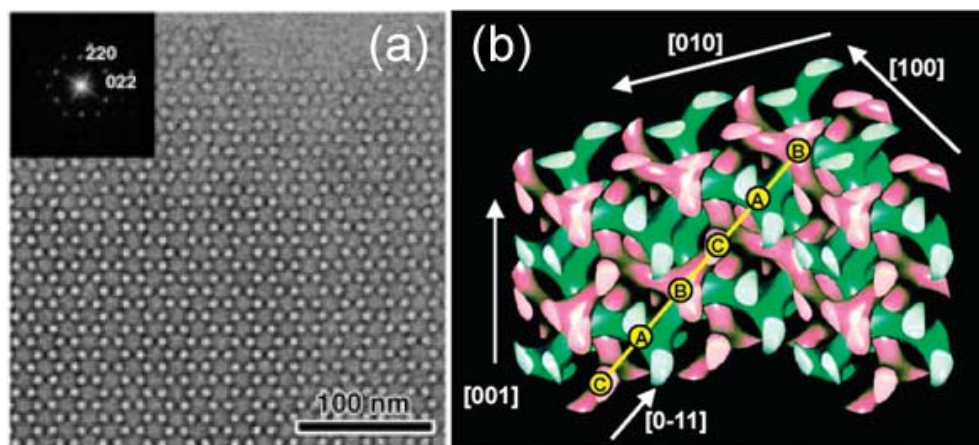


Figure 3. (a) a typical TEM image for KIT-6 recorded along [111] direction; (b) a schematic diagram for KIT-6 pore structure. A, B, and C in (b) indicate the channels.¹⁰

Although many approaches have been developed to synthesize mesoporous silica materials, it is still difficult to apply these methods to the preparation of non-silica mesoporous materials, such as mesoporous carbon and mesoporous transition metal oxides. Among these mesoporous non-silica materials, mesoporous transition metal oxides are important targets, because such solids can combine open d-shells, high surface area, limited wall thickness and open pore networks, with the result that they may exhibit many interesting properties in catalysis, electron transfer, energy conversion and storage, and magnetic devices.¹¹⁻¹⁷ The first synthesis of a mesoporous transition metal oxide TiO_2 was reported by Jackie Y. Ying and her co-workers in 1995, using long chain alkyl amines as templates.¹⁸ This ‘ligand-assisted’ method was also used to prepare mesoporous Nb_2O_5 .¹⁶ Following their work, many groups began to explore the synthesis, properties, and possible applications of mesoporous transition metal oxides. Several mesoporous transition metal oxides have been successfully prepared, such as TiO_2 , ZrO_2 , Nb_2O_5 , SnO_2 , Ta_2O_5 , WO_3 , and MnO_x .^{17, 19,}
²⁰ Some typical TEM images of the pore structures of mesoporous transition metal oxides are shown in Figure 4. These materials have been widely studied as catalysts, electrodes, and optical materials.^{5, 12} Synthesis methods for mesoporous transition metal oxides may be divided into two groups based on soft or hard templates.

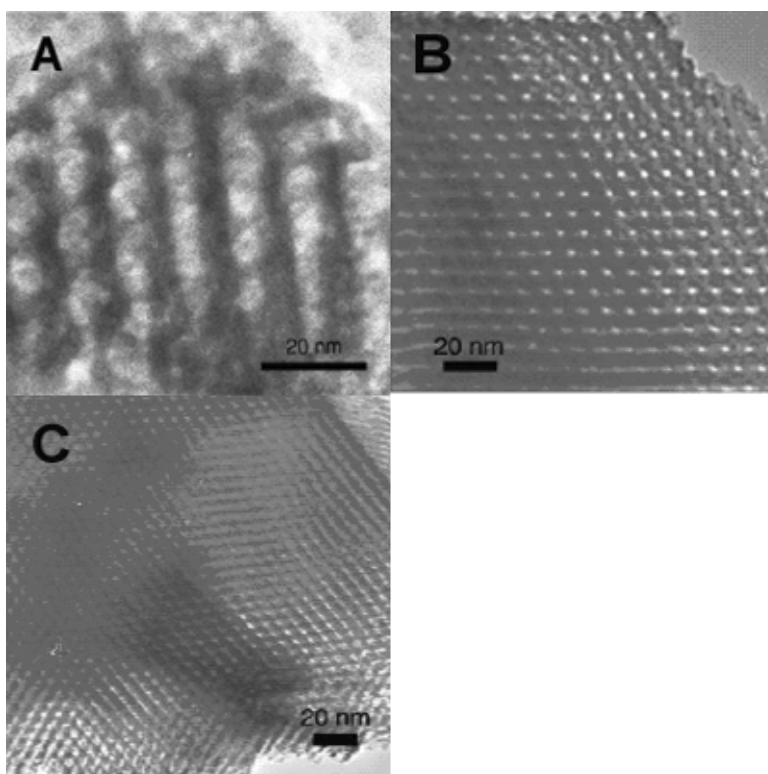


Figure 4. Typical TEM images of mesoporous transition metal oxides: (A) TiO₂, (B) ZrO₂, and (C) Nb₂O₅.¹⁹

1-1-2 Soft template method

The soft template method may be further divided into two categories: (a) using poly(alkylene oxide) block copolymers as structure-directing agent (neutral templating method); (b) using amine surfactants as template (ligand-assisted templating method). By using these soft template methods, the final materials usually have a large surface area ($> 200 \text{ m}^2/\text{g}$). For example, mesoporous TiO₂ with a specific surface area as large as $500 \text{ m}^2/\text{g}$ has been prepared by using copolymer P123 as soft template.²¹

Nevertheless, the materials prepared by soft templating have their limitations. The resulting product, just like the silica materials prepared by similar approaches, usually has poorly crystalline or amorphous walls and poor thermal stability.²² Also, despite much effort, the range of mesoporous transition metal oxides which can be prepared by this soft template method is limited because of the complicated synthesis conditions, such as pH, aging temperature, solvent, and inorganic precursors.

To synthesize mesoporous transition metal oxides by soft templating, because of their potentially unique properties, required a novel approach, which should ideally be a simple procedure to obtain materials with controllable pore sizes and pore structures.

1-1-3 Hard template method

The hard template method was first introduced by Ryoo and Terasaki.²³ They reported the synthesis of three-dimensional mesoporous Pt by using MCM-48 as hard template. The schematic diagram representing the process is shown in Figure 5. The empty ordered mesopores of MCM-48 are first filled with inorganic precursors; the precursor is then converted to the dense material by for example, reduction or decomposition, to form the desired material inside the pores. Then, the mesoporous silica template is removed using a hot 2M NaOH or a 10% HF solution and after washing with water a material replicating the mesostructure of the hard template is obtained. This method has been developed to prepare mesoporous carbons, such as CMK-1, CMK-3, and CMK-6.²⁴⁻²⁶

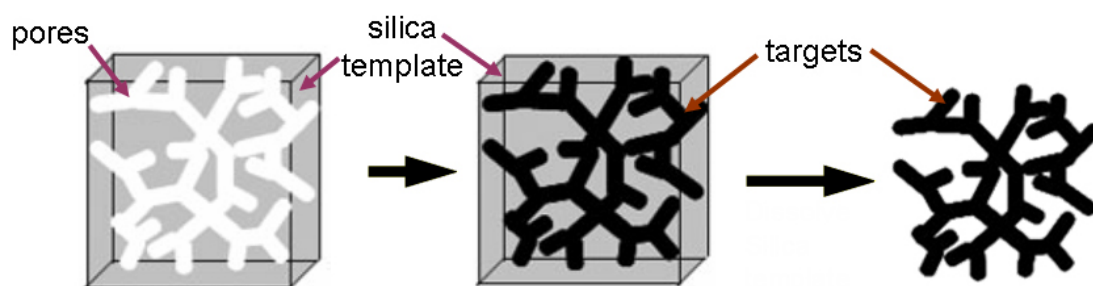


Figure 5. Schematic diagram of hard template synthesis.

The first preparation of three-dimensional highly crystalline porous transition metal oxides by the hard template route was reported by Zhu and co-workers.²⁷ Using amine group grafted SBA-15, they obtained porous Cr_2O_3 with highly ordered pores and highly crystalline (single-crystal like) walls. The mesostructure consisted of nanowires connected by short bridges (Figure 6), which replicate the pore structure of SBA-15. Via a similar approach, porous Fe_2O_3 with a similar nanowire-bundle structure was reported and this material exhibits interesting catalytic activity for

phenol hydroxylation.²⁸ Almost simultaneously, Zhao's group reported a series of porous transition metal oxides, such as Co_3O_4 , NiO , Mn_xO_y , and Fe_2O_3 , prepared using microwave/ HNO_3 treated SBA-15 as hard template.²⁹

The hard template procedure offers a number of advantages. The mesostructure of the target material may be controlled by selecting different templates, because many mesoporous silicas with different porous structures are already known.

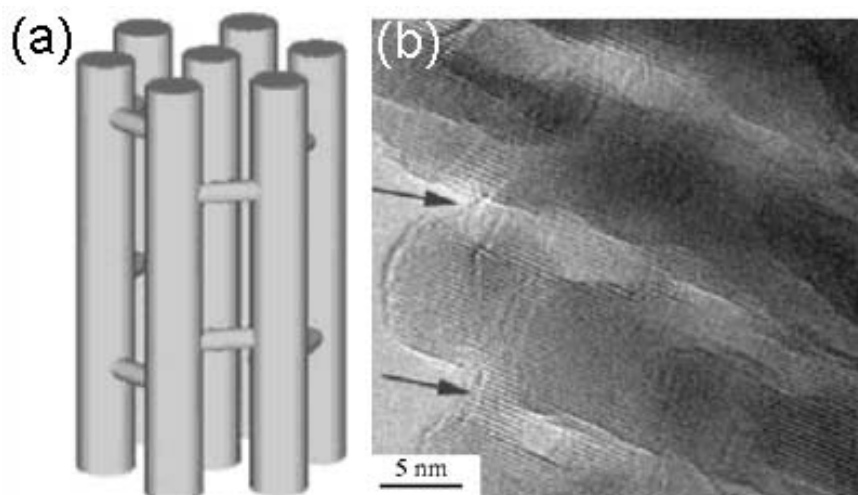


Figure 6. (a) Mesostructure model and (b) HRTEM image for mesoporous Cr_2O_3 . The arrows indicate the small ‘bridges’ between the wires.²⁷

Also the hard template method permits the synthesis of mesoporous materials with highly crystalline walls, which is a breakthrough in mesoporous material research. Before the introduce of the hard template method, all previously reported mesoporous materials including silicas, aluminosilicates and transition metal oxides had amorphous or poorly/semi- crystalline walls, which usually exhibit poor thermal stability.^{4, 13, 15, 19} It is known that well crystallized zeolites are much more stable than the amorphous/poorly crystalline mesoporous silicas in catalytic reactions. Furthermore, many important properties, such as magnetic and electrochemical properties, may be influenced by the crystallinity of the walls. For example, the magnetic behaviour of amorphous and highly crystalline mesoporous Fe_2O_3 proved to be completely different.²² Electrode materials with a highly crystalline structure perform better as intercalation hosts than the amorphous materials.

Although successful, the hard template method for synthesizing mesoporous

transition metal oxides still has its limitations. The target material must be stable in NaOH or HF solution, used to remove the silica template. For example, the synthesis of mesoporous vanadium oxide hasn't been successful using mesoporous silica as the hard template, because vanadium oxide dissolves in NaOH and will react with HF. A solution step is still required as the means of introducing the transition metal precursor and this limits the range of materials to those stable in solution. Also, materials for which the precursors react with the mesoporous silica cannot be obtained (e.g. lithium). Mesopores will also collapse if the desired phase requires heating above 900 °C.

1-2 General introduction into nanoparticles of transition metal oxides

Nanoparticulate transition metal oxides can exhibit enhanced optical magnetic and electrical properties compared with their bulk counterparts, rendering such nanoparticles of interest for a variety of applications, e.g. as electrodes in energy storage devices, as catalysts and as magnetic storage devices.³⁰⁻³⁴ Generally, nanoparticles exhibit a distribution in their size; however, synthesis routes leading to the formation of monodispersed particle sizes are becoming more available (Figure 7).^{30, 32} Such monodispersity is particularly important in the case of nanoparticles, because of the influence of size on their properties. For example, bulk magnetite Fe_3O_4 is ferromagnetic; however nano-sized Fe_3O_4 exhibits superparamagnetic behaviour.³⁰ And the blocking temperature can be justified by changing the particle size. In another case, Tarascon and co-workers reported the effect of particle size on the reactivity of $\alpha\text{-Fe}_2\text{O}_3$ powders when reacted with metallic lithium.³⁵ Large particles in the micrometric range ($\sim 0.5 \mu\text{m}$, $2 \text{ m}^2/\text{g}$) undergo an irreversible transformation of the close-packed anionic array hexagonal ($\alpha\text{-Fe}_2\text{O}_3$) to a disordered cubic stacking ($\text{Li}_2\text{Fe}_2\text{O}_3$) as soon as a small amount of lithium ($x_c = 0.03 \text{ Li}/\text{Fe}_2\text{O}_3$) is inserted in the corundum structure. However, when the particle size is reduced to about 20 nm ($60 \text{ m}^2/\text{g}$), Fe_2O_3 nanoparticles can reversibly and topotactically react with up to 1 Li per formula unit without phase transformation.³⁵

Recent advances in the colloidal synthesis of transition metal oxides reveal that

thermal decomposition of metal acetylacetonates, metal alkoxides and metal carbonyls in complex organic solvent systems can lead to metal oxide nanoparticles with uniform sizes.^{30, 32, 36} The thermal decomposition usually was undertaken under nitrogen or argon protection. The oxidation state of the metal in final products is sometimes different from that of metal in precursors, which may be due to self-oxidation/reduction during decomposition. Several transition metal oxide nanoparticles with a uniform particle size, such as γ -Fe₂O₃, NiO, MnO, and Fe₃O₄, have been prepared.^{30, 32, 36} This makes their uses in many applications possible.

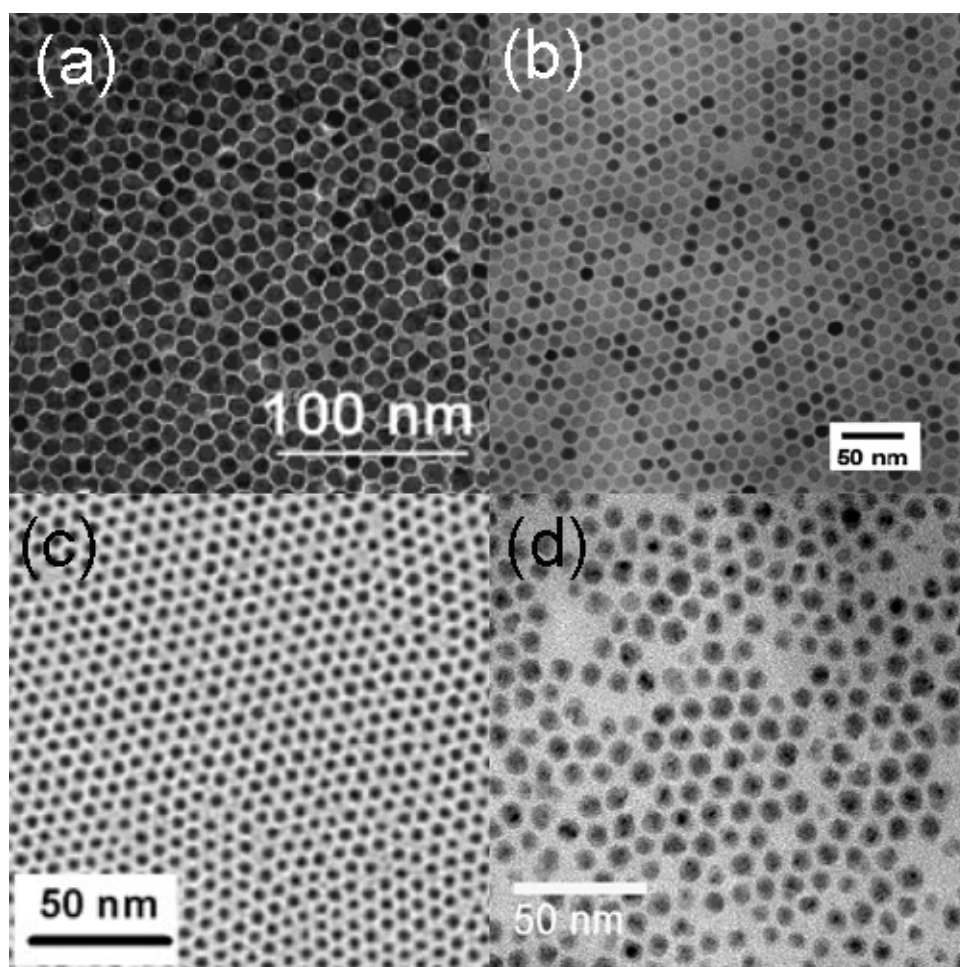


Figure 7. TEM images for (a) MnO, (b) Fe₃O₄, (c) NiO, and (d) CuO nanoparticles.^{30, 32, 36, 37}

It has been found that monodispersed nanoparticles can self-assemble into 2D or 3D ordered arrays, with which materials may exhibit unique electronic, optical and magnetic behaviour by interactions between neighbouring particles. Self-assembly processes have attracted much attention and a few ordered three dimensional

transition metal oxide nanoparticulate arrays, such as Fe_3O_4 , MnO , Fe_2O_3 , and Cu_2O , were reported.³⁸⁻⁴⁰ For example, highly ordered 3D array of MnO nanoparticles has been obtained by controlling the solvent evaporation process (Figure 8).³⁷ This technique was also used in preparation of other transition metal arrays. Very recently, Co_3O_4 nanoparticulate array was reported by a surface modification technique. Monodispersed Co_3O_4 nanoparticles were treated by reducing agents and a thin layer of cobalt metal formed on the particle surface. The authors claimed that the introduction of a thin cobalt layer which is superparamagnetic enables the self-assembly into ordered arrays. This result indicates that the core-shell structure may influence the magnetic behaviour of nanoparticles and the self-assembly process.

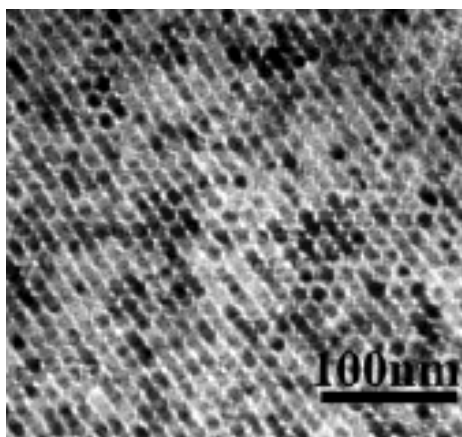


Figure 8. TEM image of 3D arrays of MnO nanoparticles.³⁷

1-3 Rechargeable lithium-ion batteries

1-3-1 General introduction into rechargeable lithium-ion batteries

Batteries store electrical energy in a chemical form, and rechargeable batteries do so reversibly. The lithium-ion battery is one of the most important innovation in rechargeable (secondary) batteries in 100 years.⁴¹⁻⁴³ The lithium-ion battery has many advantages over other rechargeable batteries, such as storing up to three times more energy, working at higher voltage (~ 3.5 V) rather than ~ 1.5 V for traditional batteries, and providing green batteries which do not produce any carbon dioxide or toxic products during cycling.

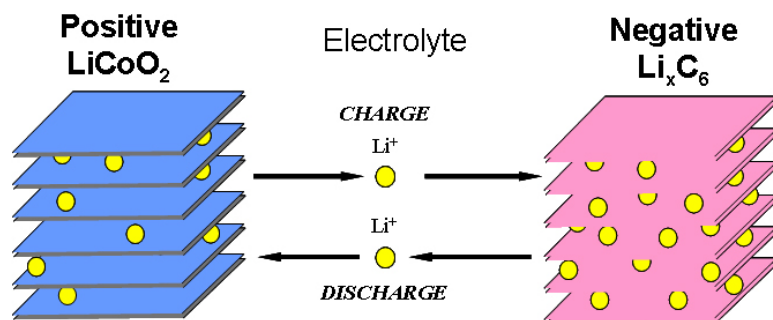


Figure 9. Schematic diagram of lithium-ion battery.

A lithium-ion battery containing Li consists of a positive electrode, which is usually an intercalation solid (normally LiCoO₂), a negative electrode which is usually another intercalation compound (normally graphite), and an electrolyte (composed of a Li salt, LiPF₆, dissolved in a non-aqueous solvent, mixture of ethylene and dimethyl carbonate), Figure 9. When it is charged, the lithium ions are removed from the positive electrode, pass through the electrolyte and are inserted into the negative electrode; while when it is discharged, the lithium ions are removed from negative electrode, pass through the electrolyte and reinserted into the positive electrode. This type of battery is safer than batteries containing lithium metal instead of graphite because lithium metal may cause serious safety problems especially due to dendrite formation on charging. After the first commercialized lithium-ion battery (LiCoO₂/C) was produced by the Sony Company in 1991, billions of lithium-ion batteries have been produced every year and widely used in many applications, such as laptops, mobile phones, digital cameras and recently power tools.⁴⁴

The lithium-ion battery market is growing very rapidly, but it demands scientific research and development to deliver improvements. Many new markets require more powerful lithium-ion batteries, i.e. a battery that can be discharged and charged much more quickly than the present devices. The electrodes used today support only slow charge/discharge rates, because of their low surface area and long diffusion path for ions and electrons within the particles due to large (μm) particle sizes. Materials with high surface area and short lithium diffusion path are required for future applications, such as power tools and hybrid electric vehicles. Such markets also require cheaper and safer positive electrode materials to replace toxic and expensive LiCoO₂. For

other materials, higher capacity materials, such as Li-metal alloys, Si or Sn based anodes and new transition metal oxides, have been investigated as negative electrodes.

All the above points indicate that novel electrode materials hold the key to future cheaper, safer, and more powerful lithium-ion batteries. In the following paragraphs, historic and current developments in positive and negative electrode materials will be discussed in greater detail.

1-3-2 Positive electrode material

In the 1980s, Goodenough proposed a series of layered LiMO_2 ($M = \text{Ni}$ or Co) electrode materials. LiCoO_2 is still the most widely used positive electrode material in commercial cells.⁴⁵ LiCoO_2 crystallizes in the space group R-3m with lattice parameters $a = 2.814 \text{ \AA}$ and $c = 14.048 \text{ \AA}$ (Figure 10). The crystal structure consists of a lithium layer between two transition metal oxide layers, from which lithium can be removed and reinserted without destroying the structure. Although the theoretical discharge capacity is $\sim 274 \text{ mAh/g}$ (based on Co^{3+} - Co^{4+} , corresponding to the reaction $\text{Li}^+ + \text{CoO}_2 \leftrightarrow \text{LiCoO}_2 - e^-$), only half of the lithium can be removed and reinserted reversibly from this layered structure and thus only $\sim 130 \text{ mAh/g}$ capacity is achieved in a real cell. LiCoO_2 discharges at $\sim 4 \text{ V}$ with good capacity retention (capacity fade at $\sim 0.1\%$ per cycle). However, because cobalt is toxic and expensive, many other layered compounds with non-toxic and cheap elements have been explored.

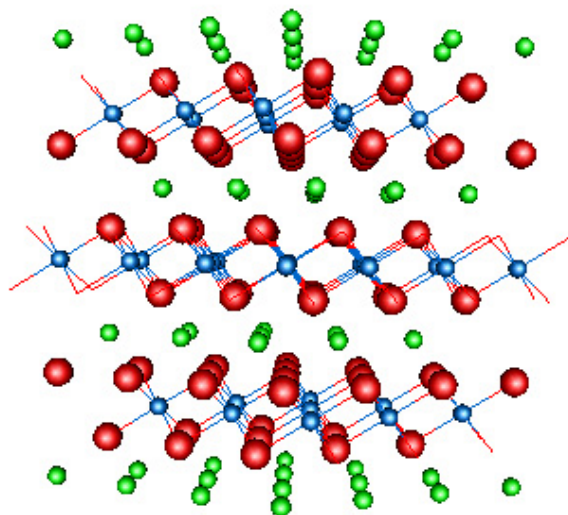


Figure 10. Crystal structure of layered LiCoO₂. Green, blue, and red balls represent lithium, cobalt, and oxygen atoms, respectively.

LiMnO₂ with a similar layered structure was proposed to be a good electrode material due to the low price, low toxicity and high safety. However, direct synthesis of LiMnO₂ with a layered structure was not successful. In 1996, Bruce's group reported the first example of layered LiMnO₂, essentially isostructural with LiCoO₂, through a Li⁺ ion-exchange process with NaMnO₂.⁴⁶ This layered LiMnO₂ compound with space group of C2/m (Figure 11) delivers a much higher first charge capacity (~ 270 mAh/g) than that of LiCoO₂ (~ 130 mAh/g). However, it suffered a continuous structure change during cycling and it converted to spinel. Recent studies indicate that conversion forms nanodomains of spinel that in fact exhibit good capacity retention in both 3V and 4V ranges. Although layered LiMnO₂ suffered a safety problem (O loss from layered material on heating), layered materials based on LiMnO₂, specially Li(Ni_{0.5}Mn_{0.5})O₂ and Li(Ni_{1/3}Co_{1/3}Mn_{1/3})O₂ are receiving a great amount of attention.^{47, 48} Recent reports confirmed the oxidation states of Ni and Mn in these materials are 2+ and 4+, respectively. Mn⁴⁺ does not migrate to the Li layer or form spinel, while the Ni²⁺ switches between Ni²⁺ and Ni⁴⁺ on cycling. Li(Ni_{0.5}Mn_{0.5})O₂ has a high theoretical capacity (~ 280 mAh/g) and delivers ~ 180 mAh/g on the first cycle. Its rate capacity is poor, because of ~ 10 % Ni existing in the Li layers. It has been shown that material synthesized by exchanging from Na(Ni_{0.5}Mn_{0.5})O₂ has less

than 5% and rate capacity is better than that of material prepared by conventional solid state reaction. The $\text{Li}(\text{Ni}_{1/3}\text{Co}_{1/3}\text{Mn}_{1/3})\text{O}_2$ phase contains cobalt which reduces the Ni/Li exchange and increases electronic conductivity. Recent results by Bruce's group showed that such a material may be synthesized which delivers above 200 mAh/g at 1C and 175 mAh/g at 10C (discharge in 6 mins).

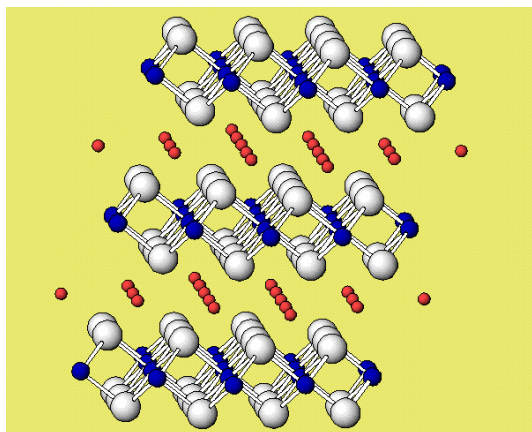


Figure 11. The crystal structure of layered LiMnO_2 . White, blue, and red balls represent oxygen, manganese, and lithium atoms, respectively.

In addition to the well-known layered structures, materials with the spinel structure have also been considered, such as low temperature LiCoO_2 , LiMn_2O_4 , and LiFe_5O_8 .⁴⁹⁻⁵¹ Among these spinel compounds, LiMn_2O_4 is the most important one because manganese is cheap and of low toxicity. The LiMn_2O_4 spinel structure is shown in Figure 12 (cubic $\text{Fd-}3\text{m}$ space group). The structure consists of a cubic close packed oxygen subarray with Mn ions in the 16d sites and Li ions in the 8a sites. The material may be charged to remove one lithium from the structure to form $\lambda\text{-MnO}_2$. In the following discharging, ~ 1 Li can be reinserted into $\lambda\text{-MnO}_2$ with two plateaus, one at 4.1V and the other at 3.9V, which correspond to lithium insertion into tetragonal sites in $\text{Li}_x\text{Mn}_2\text{O}_4$ ($0 < x < 1$). Beyond $\text{Li}_1\text{Mn}_2\text{O}_4$, Li may also be inserted and removed over the range $1 < x < 2$ in $\text{Li}_x\text{Mn}_2\text{O}_4$; this occurs at ~ 3 V. Electrode dissolution is not too serious and this can be improved further; less than 6% capacity fading after 50 cycles in 4V range has been achieved by doping $\sim 7\%$ Li in this compound (Figure 13). However, 7% Li doping reduces the amount of Mn^{3+} in the compound so that the discharge capacity in the 4V range is decreased to ~ 117 mAh/g (Figure 13).

Further discharging to 3V range will reduce the average oxidation state of Mn below +3.5 and introduces the Jahn-Teller distortion (a two phase reaction between cubic LiMn_2O_4 and tetragonal $\text{Li}_2\text{Mn}_2\text{O}_4$). Therefore, the 3V process is less reversible than the 4V range.^{50, 51} Breaking up the big crystals into nanodomains via ball milling showed significant improvement in the cycling performance in this range, which indicates that nanostructuring may be helpful in achieving superior performance of the material.⁵²

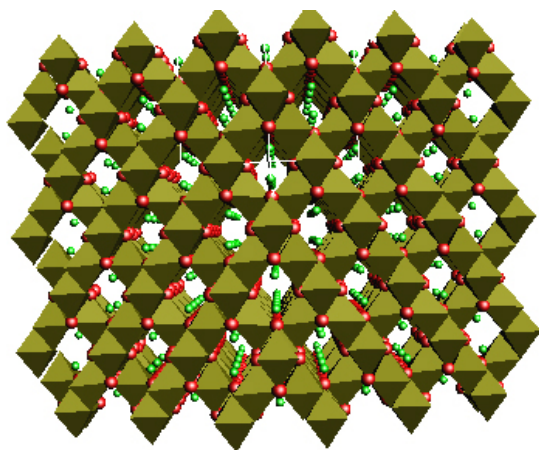


Figure 12. Crystal structure of LiMn_2O_4 spinel. Green and red balls represent lithium and oxygen atoms, respectively.

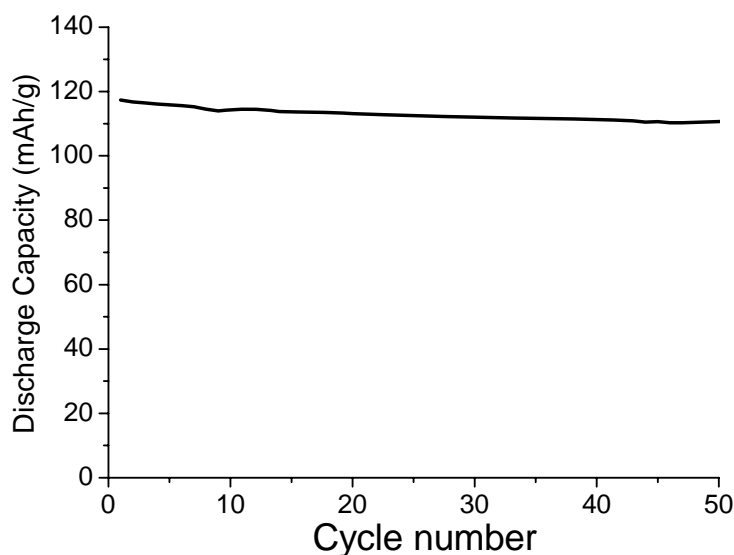


Figure 13. Cycling data for $\text{Li}_{1.07}\text{Mn}_{1.93}\text{O}_4$. Voltage range: 3.2 – 4.5V; current density: 30 mA/g.

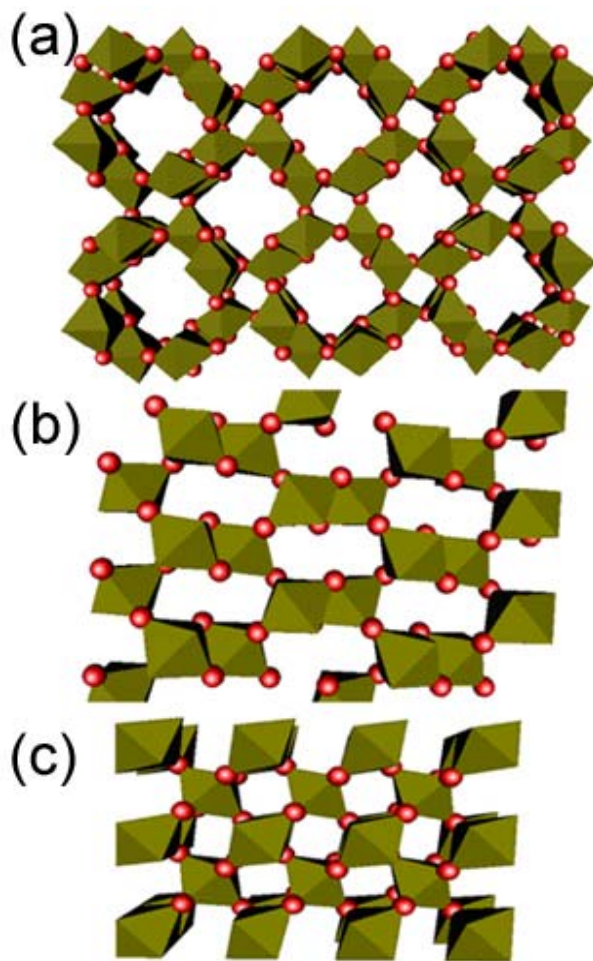


Figure 14. Crystal structures for (a) α -MnO₂, (b) γ -MnO₂, and (c) β -MnO₂. Red balls represent oxygen atoms.

Although most of well-known positive electrode materials contain lithium, some transition metal oxides, such as V₂O₅ and MnO₂, have been considered as potential positive electrodes.⁵³ Recent advances in the research of lithium metal as an anode, although not achieving commercial performances, do represent successful progress. Also the possibility of chemical methods for pre-lithiating the negative electrode, including *in situ*, makes it possible to use a variety of materials, e.g. graphite, Si, Sn, with positive electrodes that are devoid of lithium. Manganese dioxide as well as cation stabilized manganese dioxide has been widely studied for more than 20 years. There are three main phases: α -MnO₂ (2*2 structure), γ -MnO₂ (2*1 structure), and β -MnO₂ (1*1 structure), where the numbers refer to the number of MnO₆ octahedra forming the tunnels, Figure 14. Among them, amorphous or poorly crystalline MnO₂, α -MnO₂ and γ -MnO₂ have shown good performance as positive electrodes in both

primary and secondary batteries. Although the discharge voltage (M vs. Li) is low (~ 3 V), the discharging capacity (more than 150 mAh/g) is comparable to other positive electrode materials.⁵³ The β - MnO_2 with 1*1 tunnels (Figure 14c) was considered as an electrochemical inactive material in previous studies because of the difficulty of insertion of lithium into its small channels.

1-3-3 Negative electrode materials

Although lithium metal has a high gravimetric energy density (3600 mAh/g), dendrite forms on charging that limits its cycleability and safety. As a result alternative negative electrodes were sought in order to develop a battery that would be commercially successful. In the 1980s, Armand, Murphy, and Scrosati first introduced and successfully developed the concept of using an intercalation material as the negative electrode to replace Li and hence introduced the concept of the rocking-chair lithium-ion battery.

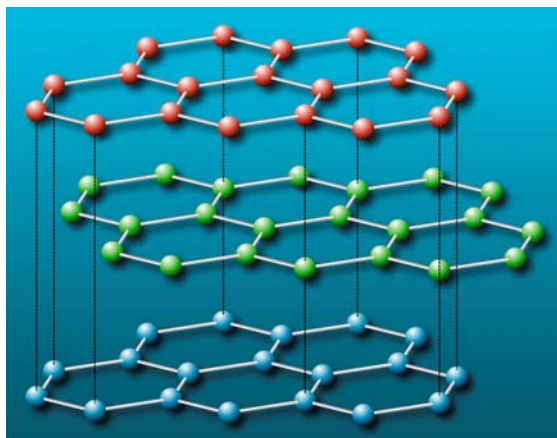


Figure 15. Schematic diagram of graphite structure.

As negative electrode, graphite has a lot of advantages, such as extremely low cost, non-toxicity, good conductivity and a sufficiently low electrochemical potential to obtain a good cell potential ($> 3\text{V}$), therefore it is still the most widely used in commercial lithium-ion batteries. Graphite has a well-known layered structure with hexagonal carbon sheets parallel each other in an ABAB... stacking along c-axis (Figure 15), which exhibits a reversible discharge capacity of ~ 300 mAh/g and a discharge plateau below 0.25 V.⁵⁴ However, due to the limitation of low gravimetric

capacity as low as 372 mAh/g (based on LiC_6) and low volumetric capacity (1000 mAh/cc) of carbon, other candidates (i.e. metal alloys) were investigated.

Metals, such as Al, Sn, and Sb, react with lithium and form alloys at low potentials vs. Li. Much of early work focused on Li/Sn alloys because their high theoretical capacity (~ 1000 mAh/g, based on lithiated phase $\text{Li}_{17}\text{Sn}_4$) and large theoretical volumetric capacity (~ 7000 mAh/cc).^{55, 56} However, this material suffered a safety problem due to the large volume change ($\sim 250\%$) on cycling. Intermetallic composites were considered as alternative solutions to solve this problem. By introducing an electrochemically inactive metal, Sn shows a better performance in metal matrix hosts, such as Fe, Ni, Mn, and Co.⁵⁷ However, this reduces both theoretical gravimetric and volumetric capacities.

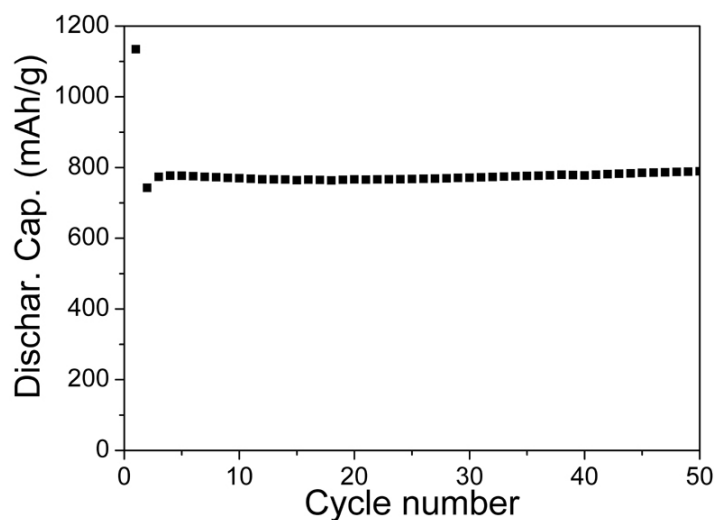


Figure 16. Cycling data for bulk Co_3O_4 between 0.005 V and 3 V with a current density of 100 mA/g.

Recently, Tarascon and co-workers developed a series of transition metal oxides as negative electrode materials, which showed much higher discharge capacity (~ 900 mAh/g) than that of graphite (less than 360 mAh/g).⁵⁸ Many transition metal oxides, such as Co_3O_4 , CoO , FeO , NiO , and Cu_2O , have been investigated. Among them, Co_3O_4 showed the highest discharge capacity (~ 800 mAh/g) and an excellent capacity retention (nearly no fading after 50 cycles), Figure 16.⁵⁸ The reaction mechanism has been described as conversion reaction (Figure 17). When it is discharged, a small amount of lithium (up to $\sim 1\text{Li}$) is first inserted into Co_3O_4 and

forms $\text{Li}_x\text{Co}_3\text{O}_4$, following by the decomposition of $\text{Li}_x\text{Co}_3\text{O}_4$ into nano-sized Co metal particles which are embedded into lithium oxide matrix. A polymer surface layer is formed on the particle surface simultaneously. This conversion reaction delivers a very high capacity with a discharge plateau at ~ 1.1 V (see Figure 18). When it is charged, Co metal and lithium oxide nanoparticles can reform cobalt oxide (CoO). Such a conversion reaction can be cycled reversibly many times without capacity fading (Figure 16). Because of the cost and toxicity of cobalt, many other transition metal oxides, such as Cu_2O , FeO, and NiO, are considered.⁵⁸ Cu_2O with large particle size showed very good capacity retention but had a relative low capacity (~ 600 mAh/g).⁵⁹ FeO and NiO gave high first discharge capacities (~ 1000 mAh/g), but they have poor capacity retention.⁵⁸

Following the discovery of conversion reaction in oxides, other materials, such as transition metal sulfides, nitrides and phosphides were also investigated as negative electrodes in lithium-ion batteries.⁶⁰⁻⁶² These materials deliver a high capacity (>600 mAh/g); however, their synthesis is usually difficult and most of them are air-sensitive, which limits their uses as negative electrodes in commercial cells.

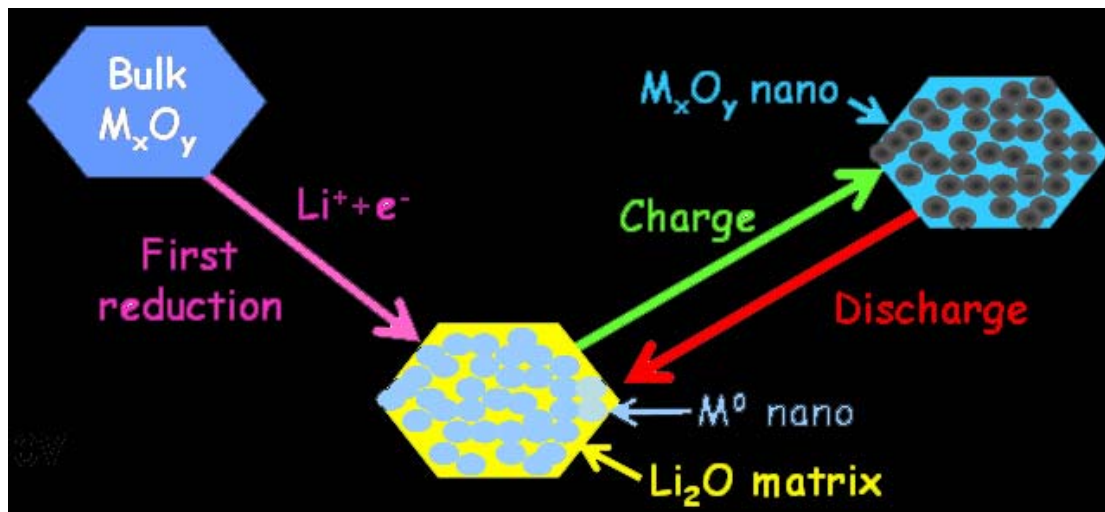


Figure 17. Schematic diagram of conversion reaction.

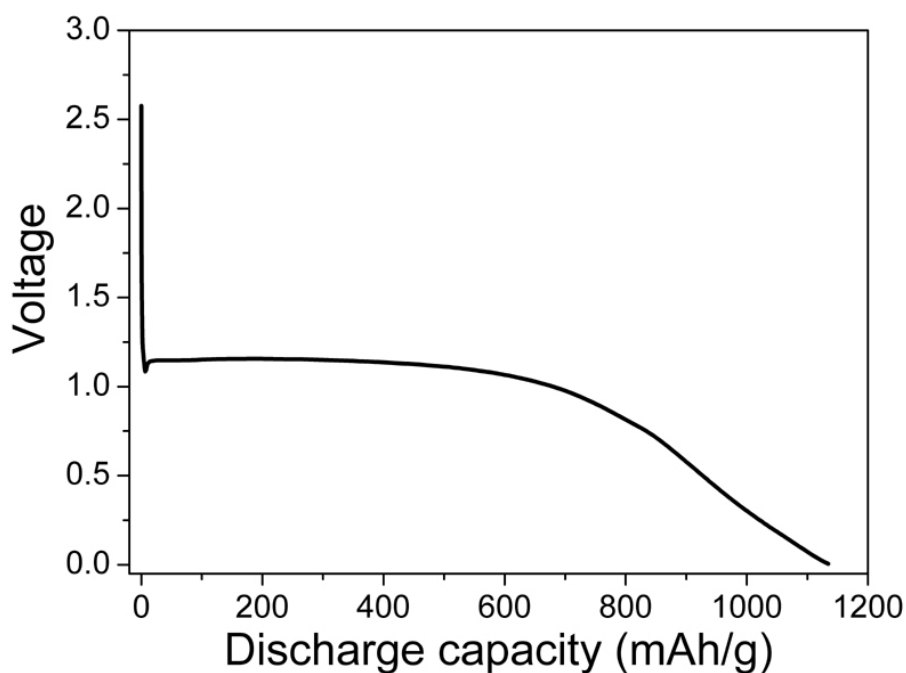


Figure 18. First discharge plot for bulk Co_3O_4 .

1-3 Aim of this research

Recognizing the limitation that the present templating method placed on the range of mesoporous transition metal oxides that can be synthesized, new ways in which new mesoporous materials can be prepared that were not previously possible are required. This includes transition metal oxide mesopores in previously inaccessible oxidation states and the first examples of lithium containing mesopores.

As described above, new electrode materials hold the key to future safer, cheaper, and environmental friendly lithium-ion batteries. Furthermore, new markets for lithium-ion batteries require more powerful batteries for many future applications. To meet the requirement of powerful batteries, fast intercalation/deintercalation of lithium from both electrodes is required to deliver the high current. Nano-sized electrode materials with short lithium and electron diffusion paths and a large surface area in contact with the electrolyte would be ideal for high rate applications. However, previous work showed that nanoparticles became disconnected from each other due to their expansion and shrinkage during cycling, resulting in capacity fading.

Mesoporous electrode materials offer a potentially excellent solution. Their

micron size particles ensure better interparticle contact than for nanoparticles, while the electrolyte can flood the pores providing a high contact area. The thin walls ensure rapid lithium intercalation/deintercalation.

In addition to their electrochemical properties, nanomaterials (e.g. nanoparticulate and mesoporous transition metal oxides) have potentially unique magnetic properties. Previous reports showed that nanostructured materials, such as nanoparticles with a core-shell structure and mesoporous materials, exhibited unusual magnetic behaviours. However, due to the limitation of their synthesis methods, the range of materials can be synthesized are limited. With the aid of new simple and straight-forward synthesis methods, novel nanomaterials may be prepared and the investigation of their properties will be possible.

1-4 References

- ¹ K. S. W. Sing, D. H. Everett, R. A. W. Haul, L. Moscou, R. A. Pierotti, J. Rouquerol, and T. Siemieniowska, *Pure and Applied Chemistry*, 1985, **57**, 603.
- ² M. Kruk, M. Jaroniec, Y. Sakamoto, O. Terasaki, R. Ryoo, and C. H. Ko, *Journal of Physical Chemistry B*, 2000, **104**, 292.
- ³ J. S. Beck, J. C. Vartuli, W. J. Roth, M. E. Leonowicz, C. T. Kresge, K. D. Schmitt, C. T. W. Chu, D. H. Olson, E. W. Sheppard, S. B. McCullen, J. B. Higgins, and J. L. Schlenker, *Journal of the American Chemical Society*, 1992, **114**, 10834.
- ⁴ M. Antonietti and G. A. Ozin, *Chemistry-a European Journal*, 2004, **10**, 29.
- ⁵ J. Y. Ying, C. P. Mehnert, and M. S. Wong, *Angewandte Chemie-International Edition*, 1999, **38**, 56.
- ⁶ A. Corma, *Chemical Reviews*, 1997, **97**, 2373.
- ⁷ D. Y. Zhao, J. L. Feng, Q. S. Huo, N. Melosh, G. H. Fredrickson, B. F. Chmelka, and G. D. Stucky, *Science*, 1998, **279**, 548.
- ⁸ F. Kleitz, S. H. Choi, and R. Ryoo, *Chemical Communications*, 2003, 2136.
- ⁹ Y. Sakamoto, T. W. Kim, R. Ryoo, and O. Terasaki, *Angewandte Chemie-International Edition*, 2004, **43**, 5231.

- 10 B. Z. Tian, X. Y. Liu, L. A. Solovyov, Z. Liu, H. F. Yang, Z. D. Zhang, S. H. Xie, F. Q. Zhang, B. Tu, C. Z. Yu, O. Terasaki, and D. Y. Zhao, *Journal of the American Chemical Society*, 2004, **126**, 865.
- 11 G. J. D. Soler-illia, C. Sanchez, B. Lebeau, and J. Patarin, *Chemical Reviews*, 2002, **102**, 4093.
- 12 D. E. De Vos, M. Dams, B. F. Sels, and P. A. Jacobs, *Chemical Reviews*, 2002, **102**, 3615.
- 13 U. Ciesla and F. Schuth, *Microporous and Mesoporous Materials*, 1999, **27**, 131.
- 14 A. Sayari and P. Liu, *Microporous Materials*, 1997, **12**, 149.
- 15 D. M. Antonelli and J. Y. Ying, *Current Opinion in Colloid & Interface Science*, 1996, **1**, 523.
- 16 D. M. Antonelli, A. Nakahira, and J. Y. Ying, *Inorganic Chemistry*, 1996, **35**, 3126.
- 17 Q. S. Huo, D. I. Margolese, U. Ciesla, P. Y. Feng, T. E. Gier, P. Sieger, R. Leon, P. M. Petroff, F. Schuth, and G. D. Stucky, *Nature*, 1994, **368**, 317.
- 18 D. M. Antonelli and J. Y. Ying, *Angewandte Chemie-International Edition in English*, 1995, **34**, 2014.
- 19 P. D. Yang, D. Y. Zhao, D. I. Margolese, B. F. Chmelka, and G. D. Stucky, *Nature*, 1998, **396**, 152.
- 20 Z. R. Tian, W. Tong, J. Y. Wang, N. G. Duan, V. V. Krishnan, and S. L. Suib, *Science*, 1997, **276**, 926.
- 21 P. C. A. Alberius, K. L. Frindell, R. C. Hayward, E. J. Kramer, G. D. Stucky, and B. F. Chmelka, *Chemistry of Materials*, 2002, **14**, 3284.
- 22 F. Jiao, A. Harrison, J. C. Jumas, A. V. Chadwick, W. Kockelmann, and P. G. Bruce, *Journal of the American Chemical Society*, 2006, **128**, 5468.
- 23 H. J. Shin, R. Ryoo, Z. Liu, and O. Terasaki, *Journal of the American Chemical Society*, 2001, **123**, 1246.
- 24 S. N. Che, K. Lund, T. Tatsumi, S. Iijima, S. H. Joo, R. Ryoo, and O. Terasaki, *Angewandte Chemie-International Edition*, 2003, **42**, 2182.

- 25 H. J. Shin, R. Ryoo, M. Kruk, and M. Jaroniec, *Chemical Communications*,
2001, 349.
- 26 M. Kruk, M. Jaroniec, R. Ryoo, and S. H. Joo, *Journal of Physical Chemistry*
B, 2000, **104**, 7960.
- 27 K. K. Zhu, B. Yue, W. Z. Zhou, and H. Y. He, *Chemical Communications*,
2003, 98.
- 28 F. Jiao, B. Yue, K. K. Zhu, D. Y. Zhao, and H. Y. He, *Chemistry Letters*, 2003,
32, 770.
- 29 B. Z. Tian, X. Y. Liu, H. F. Yang, S. H. Xie, C. Z. Yu, B. Tu, and D. Y. Zhao,
Advanced Materials, 2003, **15**, 1370.
- 30 T. Hyeon, S. S. Lee, J. Park, Y. Chung, and H. Bin Na, *Journal of the*
American Chemical Society, 2001, **123**, 12798.
- 31 A. N. Shipway, E. Katz, and I. Willner, *Chemphyschem*, 2000, **1**, 18.
- 32 C. B. Murray, C. R. Kagan, and M. G. Bawendi, *Annual Review of Materials*
Science, 2000, **30**, 545.
- 33 M. Lewin, N. Carlesso, C. H. Tung, X. W. Tang, D. Cory, D. T. Scadden, and
R. Weissleder, *Nature Biotechnology*, 2000, **18**, 410.
- 34 R. H. Kodama, *Journal of Magnetism and Magnetic Materials*, 1999, **200**,
359.
- 35 D. Larcher, C. Masquelier, D. Bonnin, Y. Chabre, V. Masson, J. B. Leriche,
and J. M. Tarascon, *Journal of the Electrochemical Society*, 2003, **150**, A133.
- 36 W. S. Seo, H. H. Jo, K. Lee, B. Kim, S. J. Oh, and J. T. Park, *Angewandte*
Chemie-International Edition, 2004, **43**, 1115.
- 37 Y. N. Xia, P. D. Yang, Y. G. Sun, Y. Y. Wu, B. Mayers, B. Gates, Y. D. Yin, F.
Kim, and Y. Q. Yan, *Advanced Materials*, 2003, **15**, 353.
- 38 X. W. Teng and H. Yang, *Journal of Materials Chemistry*, 2004, **14**, 774.
- 39 H. Zeng, J. Li, J. P. Liu, Z. L. Wang, and S. H. Sun, *Nature*, 2002, **420**, 395.
- 40 M. Yin, C. K. Wu, Y. B. Lou, C. Burda, J. T. Koberstein, Y. M. Zhu, and S.
O'Brien, *Journal of the American Chemical Society*, 2005, **127**, 9506.
- 41 B. Scrosati, *Nature*, 1995, **373**, 557.

- 42 P. G. Bruce, *Chemical Communications*, 1997, 1817.
- 43 J. M. Tarascon and M. Armand, *Nature*, 2001, **414**, 359.
- 44 T. Nagaura and K. Tozawa, *Prof. Batteries Solar Cells*, 1990, **9**, 209.
- 45 K. Mizushima, P. C. Jones, P. J. Wiseman, and J. B. Goodenough, *Materials Research Bulletin*, 1980, **15**, 783.
- 46 A. R. Armstrong and P. G. Bruce, *Nature*, 1996, **381**, 499.
- 47 T. Ohzuku and Y. Makimura, *Chemistry Letters*, 2001, 744.
- 48 T. Ohzuku and Y. Makimura, *Chemistry Letters*, 2001, 642.
- 49 M. M. Thackeray, W. I. F. David, and J. B. Goodenough, *Materials Research Bulletin*, 1982, **17**, 785.
- 50 M. M. Thackeray, W. I. F. David, P. G. Bruce, and J. B. Goodenough, *Materials Research Bulletin*, 1983, **18**, 461.
- 51 M. M. Thackeray, P. J. Johnson, L. A. Depicciotto, P. G. Bruce, and J. B. Goodenough, *Materials Research Bulletin*, 1984, **19**, 179.
- 52 A. J. Paterson, A. R. Armstrong, and P. G. Bruce, *Journal of the Electrochemical Society*, 2004, **151**, A1552.
- 53 M. M. Thackeray, *Progress in Solid State Chemistry*, 1997, **25**, 1.
- 54 D. Guerard and A. Herold, *Carbon*, 1975, **13**, 337.
- 55 W. Weppner and R. A. Huggins, *Journal of the Electrochemical Society*, 1978, **125**, 7.
- 56 C. J. Wen and R. A. Huggins, *Journal of the Electrochemical Society*, 1981, **128**, 1181.
- 57 D. Larcher, L. Y. Beaulieu, O. Mao, A. E. George, and J. R. Dahn, *Journal of the Electrochemical Society*, 2000, **147**, 1703.
- 58 P. Poizot, S. Laruelle, S. Grugeon, L. Dupont, and J. M. Tarascon, *Nature*, 2000, **407**, 496.
- 59 S. Grugeon, S. Laruelle, R. Herrera-Urbina, L. Dupont, P. Poizot, and J. M. Tarascon, *Journal of the Electrochemical Society*, 2001, **148**, A285.
- 60 D. C. S. Souza, V. Pralong, A. J. Jacobson, and L. F. Nazar, *Science*, 2002, **296**, 2012.

- ⁶¹ A. Debart, L. Dupont, R. Patrice, and J. M. Tarascon, *Solid State Sciences*, 2006, **8**, 640.
- ⁶² Z. W. Fu, Y. Wang, X. L. Yue, S. L. Zhao, and Q. Z. Qin, *Journal of Physical Chemistry B*, 2004, **108**, 2236.

Chapter 2. Routine experiments and characterization techniques

2-1 Routine experimental details

2-1-1 synthesis of mesoporous silica SBA-15

The synthesis of mesoporous silica SBA-15 has been reported previously by Stucky and co-workers.¹ A detailed synthesis procedure is described as following: 2 g of Poly(ethylene glycol)-block-poly(propylene glycol)-block-poly(ethylene glycol) P123 (average M_n ~5800, Aldrich) was mixed with 75 mL of water and 4 mL of concentrated HCl (37 wt %, Fisher) in a beaker, followed by stirring at 40 °C until all polymer was dissolved. 4.4 g of tetraethyl orthosilicate (TEOS, 98%, Aldrich) was added into this solution and stirred at 40 °C for 24 h. Then, the mixture was sealed in autoclaves and heated at 100 °C for another 24 h. After the hydrothermal treatment, the resulting sample was filtered, washed with water for several times, dried at 60 °C. The polymer template was removed by calcining at 500 °C for 3 h under air.

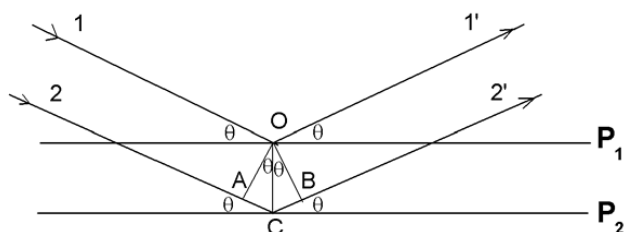
2-1-2 Synthesis of mesoporous silica KIT-6

The preparation of mesoporous silica KIT-6 was reported by Ryoo and co-workers.² A typical synthesis procedure is as following: 2 g of Poly(ethylene glycol)-block-poly(propylene glycol)-block-poly(ethylene glycol) P123 (average M_n ~5800, Aldrich) was mixed with 72.5 mL of water and 3.35 mL of concentrated HCl (37 wt %, Fisher) in a beaker. The mixture was stirred at 35 °C until a homogeneous solution was obtained. Then, 2 g of n-butanol (99.4+%, Aldrich) was added and this mixture was stirred for 1 h before 4.3 g of tetraethyl orthosilicate (TEOS, 98%, Aldrich) was added. After stirring at 35 °C for 24 h, the mixture was transferred into autoclaves which were sealed and maintained at 100 °C for another 24 h. The resulting mixture was filtered and dried at 60 °C, followed by mixing with 200-300 mL of ethanol and 10-20 mL of concentrated HCl (37 wt %, Fisher) in an 800 mL beaker. After stirring at room temperature for 1-2 h, it was filtered and washed with water and ethanol for several times. The final sample was dried at 60 °C and calcined at 500 °C for 3 h under air to remove the polymer template.

2-2 Characterization techniques

2-2-1 Powder X-ray diffraction technique

Since the experimental observation of X-ray diffraction in 1912, W. L. Bragg noticed the similarity of diffraction to ordinary reflection and deduced an uncomplicated equation treating diffraction as “reflection” from planes in the crystal lattice (see Scheme 1). A simple function, $2d\sin\theta=n\lambda$ (where d is the distance between adjacent planes of atoms, θ is the angle of incident X-ray beam, n is the order of the diffracted beam, λ is the wavelength of the X-ray beam), was established, which is called *Bragg's law*. Following this law, if the wavelength of the incident X-ray beam is known, a set of distances between the planes of atoms can be obtained by measuring reflection intensities at different angles. Because the X-ray diffraction pattern is normally unique, the identification of the target material can be achieved.



Scheme 1. X-ray diffraction. P_1 and P_2 indicate lattice plane 1 and plane 2. O and C are the contact points for injection lights and lattice planes.

Powder X-ray diffraction (PXRD) is widely used in many fields, such as material science, geology, chemistry, physics and environmental science. The sample studied in PXRD is usually in a powder form, consisting of many crystal domains with different orientations, which is different from single crystal diffraction. After a PXRD pattern is obtained, the phase is normally identified by searching the crystallography database and comparing the diffraction peaks (both the d spacings and intensities).

In the studies presented in this thesis, wide-angle PXRD data were collected in a Stoe STADI/P powder diffractometer operating in transmission mode and with a low angle position sensitive detector. Incident radiation was generated using a $\text{FeK}_{\alpha 1}$ source ($\lambda = 1.936 \text{ \AA}$). While low-angle PXRD measurements were carried out using a Rigaku/MSD, D/max-rB with $\text{Cu K}_{\alpha 1}$ radiation ($\lambda = 1.541 \text{ \AA}$) operating in reflection

mode and a scintillation detector. For the samples which are not air-sensitive, the PXRD measurements are carried out at room temperature under air; while for those air-sensitive samples, the samples were sealed in two polymer films by using vacuum grease and all assembling work was carried out under argon in an Ar filled glove box.

2-2-2 Transmission electron microscopy technique

The Transmission Electron Microscopy (TEM) is an electron-optical microscope that uses electromagnetic lenses to focus and direct an electron beam. Data are collected from the beam after it passes through the sample. The reason for using an electron beam instead of a light beam is that electrons have a much shorter wavelength than photons. Resolution and magnification of a microscope are related to the wavelength and the energy of the radiation. The shorter the wavelength, the better the resolution.

TEM is widely used to characterize a lot of materials not only from the morphological and crystallographic points of view but also for the elemental composition. Using TEM a large variety of materials as ceramics, metals, alloys, semiconductors, glasses and polymers can be observed. The main requirements for the samples are: due to the high vacuum ambient of work they must not outgas and they have to be appropriately thinned to be observed.

An electron diffraction unit is usually attached to TEM. When the electron beam is focused onto a small part of the sample (normal several to hundreds of nanometers by adjusting the spot size), an electron diffraction pattern can be obtained which is normally called selected-area electron diffraction (SAED). Based on SAED measurements, it is possible to carry out electron crystallography studies, which means solving the crystal structure of a very small single crystal using the diffracted electron beams in an electron microscope. First a series of SAED patterns from different orientations are taken on a selected particle in TEM. By combining all reflections, an electron density map may be obtained and a three-dimensional model can be set up. Further refinement is required to determine the final structure of the sample. This technique is very useful if crystalline domain size is on a nano-scale

which is too small for normal PXRD studies. This includes crystals which have a particularly short crystal dimension, such as nanocrystals, nanowire crystals, and porous materials with nanoscale crystalline walls. Further, as the crystallography is carried out in TEM, in principle, crystallography may be performed on different parts of a sample which have different composition on a sub-micron scale.

TEM studies discussed in the following chapters were carried out by using a JEOL JEM-2011 (Figure 1). This TEM uses a LaB₆ filament as the electron source and the accelerating voltage is 200 keV. TEM and HRTEM images were both recorded by a Gatan CCD camera in a digital format. The SAED patterns were recorded on traditional films followed by developing in a dark room and transforming into a digital form by scanning. The camera length for recording SAED patterns was set to 80 cm and the exposing time was varied depending on the brightness of the diffraction spots. An energy dispersive X-ray analysis (EDXA) system was attached to this TEM, which was used to identifying the elemental composition of the sample.



Figure 1. JEOL JEM 2011.

2-2-3 N₂ adsorption-desorption technique

When nitrogen is brought into contact with a solid, part of it is taken up by the solid, which is called nitrogen adsorption. This phenomenon has been studied theoretically for most of last century and the simplest of the resulting theories provide

the insight needed for most applications. Two methods were widely used to calculate the experimental data and estimate the surface area: one is Langmuir and the other is Brunauer, Emmett and Teller (BET), which is used to calculate all the specific surface area in all nitrogen adsorption measurements. BET method was first introduced in 1938 and is widely used to calculate the surface area of solids by physical gas adsorption. This method extended the Langmuir theory from monolayer molecular adsorption to multilayer adsorption. The BET equation can be expressed by the following function:

$$\frac{1}{v \left[\left(\frac{P_0}{P} \right) - 1 \right]} = \frac{1}{v_m c} \left(\frac{P}{P_0} \right) + \frac{1}{v_m}$$

In this function, P is the equilibrium pressure of nitrogen, P_0 is the saturation pressure of nitrogen at the adsorption temperature, v is the quantity of adsorbed nitrogen in the solid, c is the BET constant and v_m is the quantity of adsorbed nitrogen via monolayer mechanism. Because the linear relationship in this function only exists in the relative pressure (P/P_0) range from 0.05 to 0.35, the data for calculation of the surface area by BET method were chosen in this pressure range.

Experimental N_2 adsorption isotherms usually fall into six typical categories, which are shown in Figure 2.³

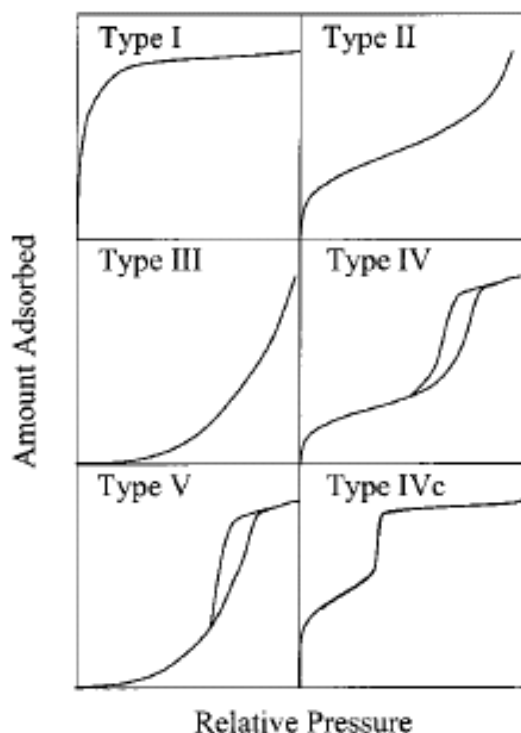


Figure 2. Classification of gas adsorption isotherms.

Type I isotherms are usually considered to be indicative of adsorption in micropores or monolayer adsorption due to strong adsorbent-adsorbate interactions. Adsorption on many macroporous solids proceeds via multilayer formation in such a manner that the amount adsorbed increases gradually as the relative pressure increases, although the multilayer buildup close to the saturation vapour pressure may be quite rapid. This unrestricted multilayer formation process gives rise to type II and III isotherms. Adsorption on mesoporous solids proceeding via multilayer adsorption followed by capillary condensation gives type IV or V isotherms.

Nitrogen adsorption-desorption measurements were carried out by using a Hiden IGA porosimeter in the current studies. The typical sample weight used in the measurement was 10-20 mg. The outgas conditions were normally set to 120 minutes at 120 °C under vacuum and all adsorption-desorption measurements were carried out under liquid nitrogen temperature.

2-2-4 Superconducting quantum interference device (SQUID) technique

Superconducting quantum interference devices (SQUID) are usually the devices,

e.g. magnetometers, which are used to measure very small magnetic fields with extremely high sensitivity. Based on the discovery of the Josephson Effect in 1962, the first dc SQUID was introduced in 1964 by people from Ford Research Labs. Because of the extremely high sensitivity to the weak magnetic field, SQUID have been used to study many topics, such as magnetic properties of materials, biological phenomena and in the geographical field.

The device used to measure the magnetic properties in the following studies is a Quantum Design SQUID magnetometer, which is located in University of Edinburgh. The sample was first weighed by using a balance and filled in a polymer container. Then, it was placed on a sample holder, which was connected to the SQUID system. Data were usually collected from 1.8 K to 300 K, in fields of 0.01 T after cooling first in zero field, and then in 0.01 T field.

2-2-5 X-ray absorption spectroscopy (XAS) techniques

In the interaction of X-rays with matter, there are three main processes: elastic scattering, inelastic scattering, and absorption due to ionisation. The absorption can be characterised by the following equation: $I_1 = I_0 \exp(-\mu x)$ where I_1 is the exiting intensity, I_0 is incident intensity, x is the distance travelled through the material and μ is the x-ray absorption coefficient of the material. The coefficient μ is energy dependent which decreases smoothly in general, but it has certain discontinuities in its values. These values are known as absorption edges. However, in condensed material when the incident X-ray is energetic enough to eject one of the core electrons, the ejected photo-electron (wave) will be scattered by neighbouring atoms. It is the interference between the outgoing electron and the back-scattered ones which leads to oscillations visible in the absorption spectrum above the edge, which can extend to up to 1000 eV past the edge. These oscillations are called the Extended X-ray absorption fine structure (EXAFS).

Based on these phenomena, X-ray absorption spectroscopy is developed to detect the formal oxidation state, coordination chemistry, and the distances, coordination

number and species of the atoms immediately surrounding the selected element. These techniques provide a practical, and relatively simple, way to determine the chemical state and local atomic structure for a selected atomic species. XAS techniques have been widely used in many fields, including biology, environmental science, catalysts research, and material science. Because this technique is an atomic probe, nearly all the elements can be measured. Moreover, XAS technique can also be used in analyzing amorphous, poorly crystalline, and highly disordered materials, which are difficult to be measured by traditional X-ray diffraction technique.

XAS is typically divided into X-ray absorption near-edge spectroscopy (XANES) and extended X-ray absorption fine-structure spectroscopy (EXAFS). A typical XAS pattern is shown in Figure 3. Though these two regions of the spectra have the same physical origin, this distinction is convenient for the interpretation. XANES is strongly sensitive to formal oxidation state and coordination chemistry (e.g., octahedral, tetrahedral coordination) of the absorbing atom, while the EXAFS is used to determine the distances, coordination number, and species of the neighbours of the absorbing atom.

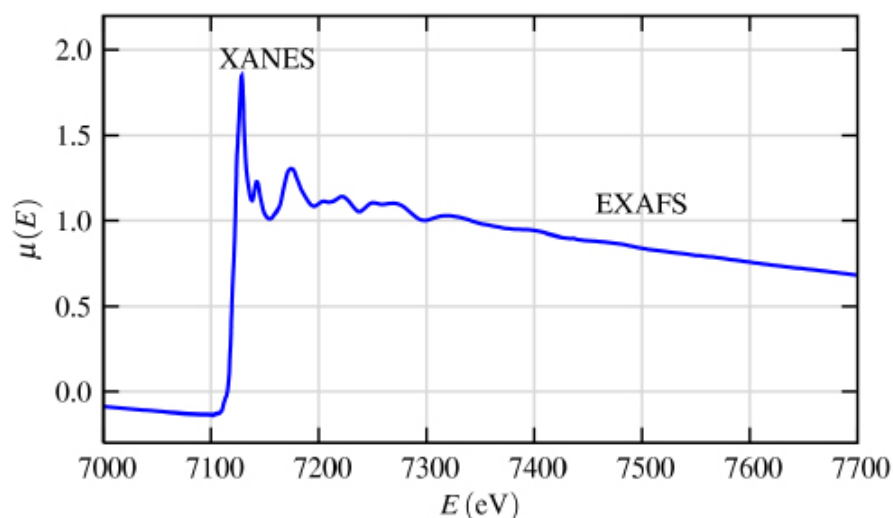


Figure 3. A typical XAS pattern.

Many experimental techniques and sample conditions are available for XAS measurements. For example, it is possible to carry out fast in situ XANES and EXAFS measurements during lithium intercalation/deintercalation processes in a lithium-ion cell. This offers a good chance to observe the oxidation state and structure

changing accompanying with the lithium intercalation. XAS experiment usually requires only a small amount of sample (~ 10 mg) which is pressed into a pellet and put on a sample holder for the measurements. For air-sensitive samples, an aluminium foil bag can be used to seal the material in an Ar filled glove box.

The XANES and EXAFS data were collected at the stations 7.1 and 9.3 in CLRC Daresbury Synchrotron Radiation Source. This source has electron energy of 2 GeV and the average current for these measurements was ~150 mA. The data were collected in transmission mode and the beam current was measured using gas filled ion chamber detectors. The scan range was from ~100 eV below the absorption edge to several hundred eV beyond the edge. The raw data were treated in a conventional manner, using the *excalib*, *exback* and *dl_excurv* programs provided by Daresbury Laboratory. Phase shifts were derived from ab initio calculations within *dl_excurv* program. The fitting of EXAFS spectrum with a known structural model from the standard database was also carried out by using this program.

2-2-6 Mössbauer spectroscopy

Mössbauer spectroscopy is developed after the discovery of the Mössbauer effect, a γ -ray resonance phenomenon in solids, by Rudolf Mössbauer in 1957. γ -ray, normally produced by nuclear transition from a high energy state to a low energy state, has an energy equal to the energy of this nuclear transition if the energy loss due to recoil to the emitting atom is relatively small. This γ -ray can be absorbed by neighbouring same type atoms. Because the recoil energy is normally negligible in solids, this emission and absorption (resonance) can occur in the whole solid rather than in a single atom. Also because γ -ray has a very short linewidth, it is sensitive to small changes in the energies of nuclear transitions. This is the basis for Mössbauer spectroscopy to monitor these interactions.

Mössbauer spectroscopy is widely used to study the structure and properties of materials in many fields, such as nanomaterials, electrochemical reactions in lithium-ion batteries, and magnetic devices. The Mössbauer spectrometer used in present studies is a standard EG&G spectrometer in the constant acceleration mode,

using a $^{57}\text{Co}(\text{Rh})$ source in University of Montpellier II, France. Experimental data were collected in a temperature range from 4 K to 300 K. The hyperfine parameters δ (isomer shift) and Δ (quadrupole splitting) were determined by fitting Lorentzian lines to the experimental data by the ISO software.

2-2-7 Batteries test

Coin type and Swagelok type cells were used in the electrochemical tests carried out in this thesis. All cell parts are dried before using. A typical assembling of a coin type cell is described as following: first dried sample is mixed with Kynar 2801 (a co-polymer based on polyvinylidene fluoride), and Super S/Super P carbon in a selected weight ratio, e.g. 85:5:10. THF is usually used to disperse this mixture. It is then cast onto an Al or Cu foil from THF using a Doctor-Blade technique. After solvent evaporation at 45 °C, the foil is cut into small discs and dried in a vacuum oven at 80 °C for 8-12 h. After drying under vacuum, the sample discs are transported into an Ar filled MBraun glovebox for the assembling. An active material coated disc is first placed on a coin cell bottom part with coated side facing upward, and then two pieces of separator are placed on the sample disc followed by adding 8-10 droplets of electrolyte LP30 (Merck; 1M LiPF_6 in 1:1 v/v ethylene carbonate:dimethyl carbonate). A small piece of lithium metal, a steel disc, a spring and a coin cell top part with a plastic sealing ring are placed on the top following this order. Finally the cell is sealed by using a coin cell pressure system.

For the assembling of Swagelok type cell, the active material is mixed with Super S carbon with a selected weight ratio, e.g. 80:20. Followed by grinding gently, the mixture is kept in a vacuum oven at 80 °C for drying overnight. After that, it is put into an Ar filled glovebox for assembling. A plastic film is placed inside the cell body first and one steel pillar with PTFE liner is sealed one end of the cell body. The active material powder is added into the body carefully and two separators are used followed by adding 8-10 droplets of liquid electrolyte LP30 (Merck). A small piece of lithium metal, a steel disc, and a spring are placed on the top, and this end of cell is sealed by another pillar with a PTFE liner.

MACCOR and Biologic MacPile II system are used in collecting the electrochemistry data. All tests were carried out at 30 °C in an oven. For the characterization of electrode materials after cycling by other techniques, such as PXRD and TEM analysis, the powder of active material was recovered from the cell followed by washing with dimethyl carbonate (DMC) several times and drying under vacuum without exposure to air.

2-3 references

- ¹ D. Y. Zhao, J. L. Feng, Q. S. Huo, N. Melosh, G. H. Fredrickson, B. F. Chmelka, and G. D. Stucky, *Science*, 1998, **279**, 548.
- ² F. Kleitz, S. H. Choi, and R. Ryoo, *Chemical Communications*, 2003, 2136.
- ³ C. G. V. Burgess, D. H. Everett, and S. Nuttall, *Pure and Applied Chemistry*, 1989, **61**, 1845.

Chapter 3. Synthesis, characterization, and magnetic properties of mesoporous iron oxides with amorphous walls

As discussed in the introduction Chapter 1, the synthesis of mesoporous transition metal oxides by soft templating has attracted much less attention than main group oxides, such as SiO_2 .¹⁻³ Very few examples of soft templated mesoporous transition metal oxides are prepared, such as TiO_2 and Nb_2O_5 .^{2,3} Mesoporous iron oxides are of particular interest. Reversible Li intercalation can occur for nanoparticulate Fe_2O_3 , while it is much more difficult to carry out such intercalation with Fe_2O_3 of normal particle size.⁴ Since the walls of a mesoporous iron oxide are of nano-dimensions, similar behaviour may be possible. The limited dimensions of the walls will also alter the magnetic behaviour from that of bulk Fe_2O_3 . Here, the first synthesis of ordered mesoporous Fe_2O_3 with controllable pore structures was demonstrated. Ordered two-dimensional (2D) hexagonal mesoporous iron oxide (2DMIO) with P6mm symmetry and three-dimensional (3D) cubic mesoporous iron oxide (3DMIO) with Fm3m symmetry have been prepared by using decylamine as the template and Fe^{III} ethoxide as the precursor. Different aging conditions were used for 2DMIO and 3DMIO. In both cases, the walls exhibit a microporous structure.⁵

3-1 Synthesis

By modifying the previous ligand-assisted method,² the synthesis procedure of 2D mesoporous iron oxide (2DMIO) was as following: 0.573 g (3 mmol) of $\text{Fe}(\text{III})$ ethoxide [$\text{Fe}(\text{CH}_3\text{CH}_2\text{O})_3$, 99%, ABCR] was dispersed in 35 mL of ethanol, and stirred for 5 minutes, followed by addition of 0.472 g (3 mmol) of decylamine (a surfactant ligand, 95%, Aldrich). After stirring at 40 °C for 2 h, the resulting solution was maintained at 40 °C for 24 h, and further aged at 80 °C for 6 h. In the case of 3DMIO, additional aging at 150 °C was carried out. Subsequently, the products were filtered (liquid removed), washed with ethanol and dried at 50 °C. The template may be removed by extraction with excess ethanol: 0.1 g of as-prepared material was added to 100 mL of ethanol with stirring at RT for 30 min, followed by filtration and drying at 70 °C under vacuum for 1 h.

3-2 Results and discussion

3-2-1 2D mesoporous Fe₂O₃

The successful template removal from 2D mesoporous iron oxide (2DMIO) was confirmed by CHN analysis. As-prepared 2DMIO contained 44.0% C, 9.69% H, and 4.82% N by weight, while the 2DMIO after ethanol extraction contained 6.48% C, 2.17% H, and 0.28% N. Based on the N analysis, about 94% of the template had been removed. Slightly high C and H contents were observed after template removal and this may correspond to a small amount of ethanol remaining in the pores.

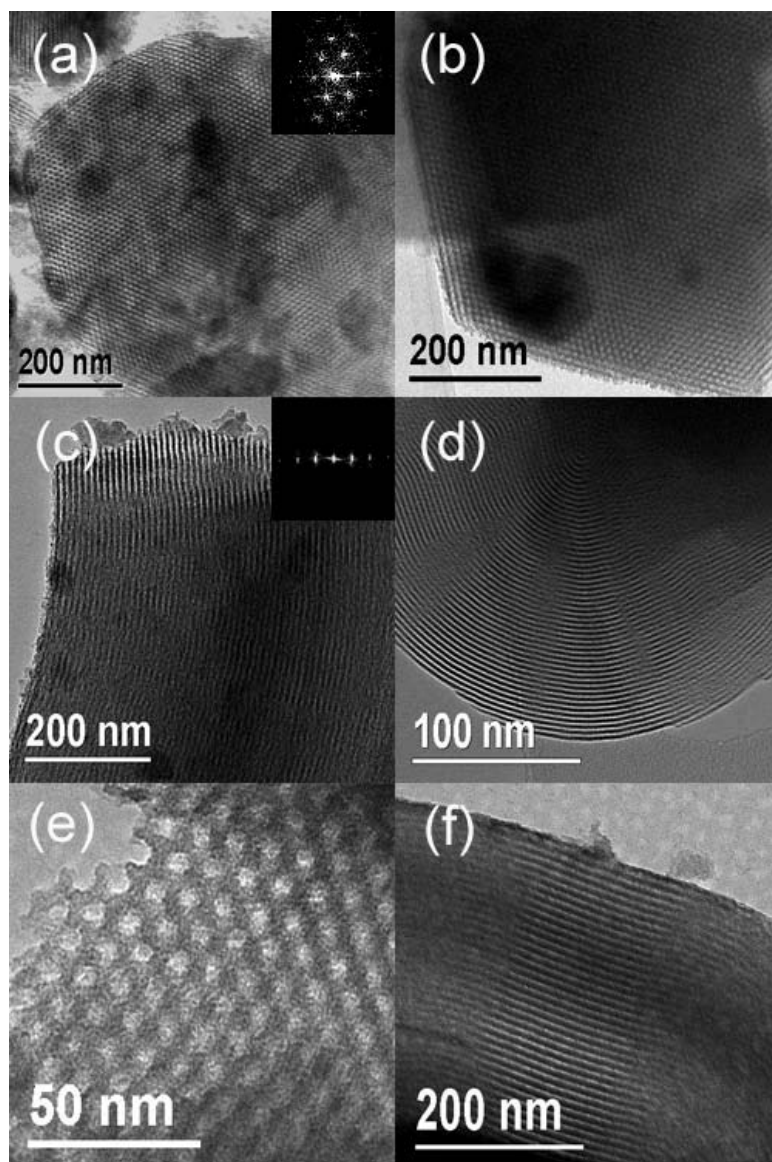


Figure 1. TEM images for 2DMIO: (a, b) recorded along [001] direction and (c, d) recorded along [110] direction. TEM images for 2DMIO after template removal recorded along (e) [001] and (f) [110] directions. The Fourier transforms (FFT)

of (a) and (c) are shown in (a, inset) and (c, inset), respectively.

A transmission electron microscope (TEM) image of ordered 2DMIO was recorded along the [001] direction (Figure 1a and b) and the corresponding FFT pattern (Figure 1a, inset) confirmed a hexagonal structure over a large area. Examination of a wide range of particles demonstrated that they all had similar structures. Combining these results with the TEM result recorded along the [110] direction (Figure 1c and d) and their FFT pattern (Figure 1c, inset), it is clear that our 2DMIO has a large scale well-ordered 2D hexagonal array of mesopores, similar to those typically observed in 2D hexagonal mesoporous silica materials, such as MCM-41 and SBA-15.^{6, 7} After template removal, the highly ordered hexagonal mesoporous structure is maintained, based on TEM results (Figure 1e and f).

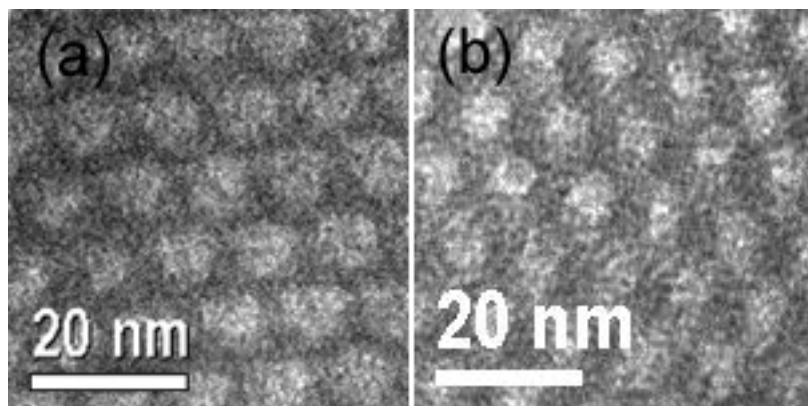


Figure 2. HRTEM images for (a) as-prepared and (b) after template removal 2DMIO.

From the high-resolution transmission electron microscopy (HRTEM) image of as-prepared 2DMIO recorded along the [001] direction (Figure 2a), an average pore size of 70 Å and wall thickness of 40 Å, with a cell parameter for the mesostructure a_0 of 110 Å were estimated. The low-angle powder X-ray diffraction (PXRD) pattern (Figure 3) of as-prepared 2DMIO exhibits a diffraction peak at $2\theta = 1.14^\circ$, which translates to a d -spacing of 97.6 Å ($FeK_{\alpha_1}, \lambda = 1.936 \text{ \AA}$). The peak may be indexed as the [100] reflection, based on the hexagonal space group P6mm, identified by TEM analysis. It corresponds to an a_0 unit cell parameter of 113 Å, in good agreement with the TEM data. From the well ordered hexagonal arrangement of mesopores revealed in Figures 1a and b, peaks might also be expected in the PXRD pattern at $2\theta = 1.97^\circ$

and 2.29° , corresponding to d -spacings of 56.4 \AA and 48.4 \AA , for the [110] and [200] reflections, respectively. These peaks are not evident. This appears to be due, at least in part, to the existence of a broad peak in the range of 2θ from 2.2° to 4° , corresponding to d -spacings between 25 and 45 \AA . Such a broad peak is consistent with disordered microporous regions within the walls as observed by HRTEM (Figure 2) and discussed later.

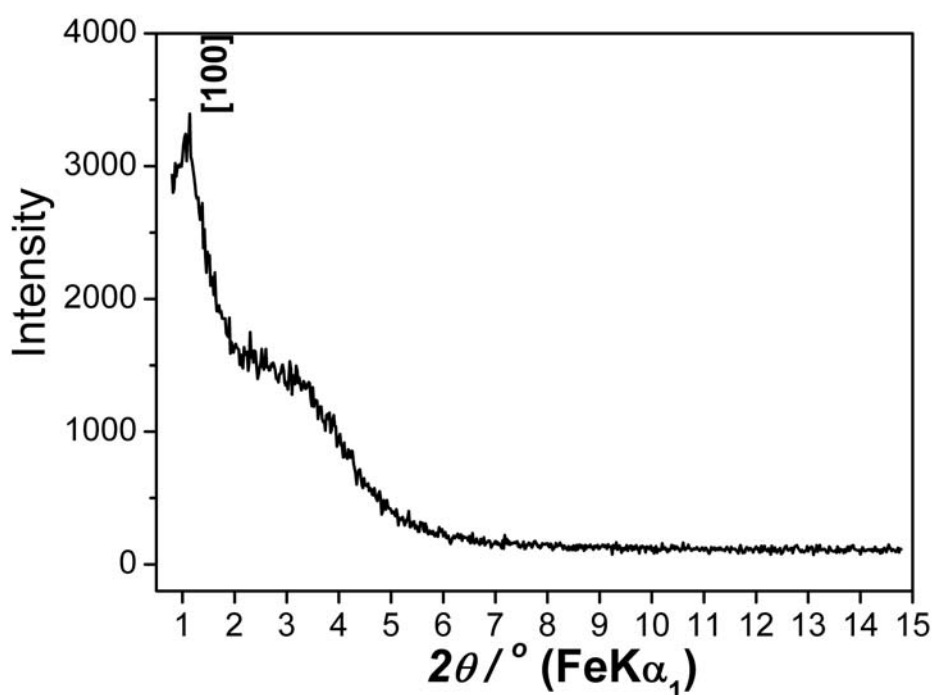


Figure 3. Low-angle PXRD pattern for as-prepared 2DMIO.

After removing the template by ethanol extraction, a smaller average pore size of 54 \AA and a wall thickness of 51 \AA may be estimated by the HRTEM image of 2DMIO (Figure 2b); the reduced pore diameter is due to shrinkage accompanying removal of the decylamine. Such a pore size is larger than those previously reported for mesoporous transition metal oxides templated by alkyl amines of comparable size, such as TiO_2 and Nb_2O_5 , indicating the formation mechanism may be different in the present case.^{2, 3} Mössbauer measurements (Figure 4) indicate that the Fe oxidation state is +3 and that the iron is in an octahedral oxygen environment. Mössbauer data for 2DMIO show a doublet indicating no magnetic order and from the separation of the two peaks it is clear that the material exhibits superparamagnetic behaviour. More

details concerning the Mössbauer studies will be discussed along with magnetic measurements on mesoporous iron oxides with amorphous/nanocrystalline/highly crystalline walls in Chapter 4-1.

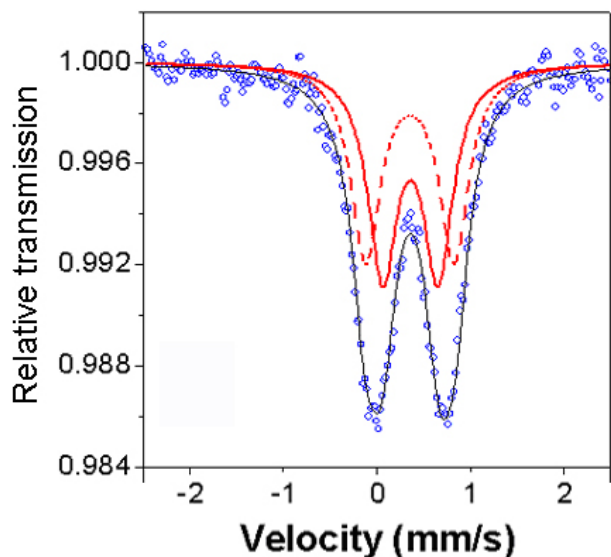


Figure 4. Mössbauer data for 2DMIO.

A detailed examination of the HRTEM image (Figure 2) for as-prepared 2DMIO shows a large quantity of disordered micropores within the walls and with pore sizes of around 10 Å. This suggests that the formation mechanism of 2DMIO mesopores may involve self-assembly of microporous structures. Further extensive studies would be required to understand the exact nature of the formation mechanism for this micro/mesoporous solid, including the role of the template and self-assembly of microporous structures into the micro/mesoporous solid. The microporosity of 2DMIO is further confirmed by nitrogen adsorption-desorption analysis. The N₂ adsorption-desorption isotherms (Figure 5a) for 2DMIO after template removal show predominantly a type I curve, indicating that the dominant surface area is in fact the micropores. There is a small step at the relative pressure of 0.7-0.8, which corresponds to mesoporous adsorption in 2DMIO. The identification of microporosity in the walls of mesoporous materials has been observed before, especially in SBA-15, MAS-7, and MTS-9.^{8,9} However, the ratio of micropores to mesopores is much higher in the transition metal oxides, as is evident from the small mesopore adsorption at relative pressure 0.7 and 0.8. Since the TEM clearly indicates significant

mesoporosity, we propose that the surfaces of the mesoporous walls may themselves be highly microporous resulting in even greater domination of the sorption isotherms by microporous behaviour (type I), Figure 5a. The Brunauer-Emmett-Teller (BET) surface area of 2DMIO is $340 \text{ m}^2\text{g}^{-1}$.

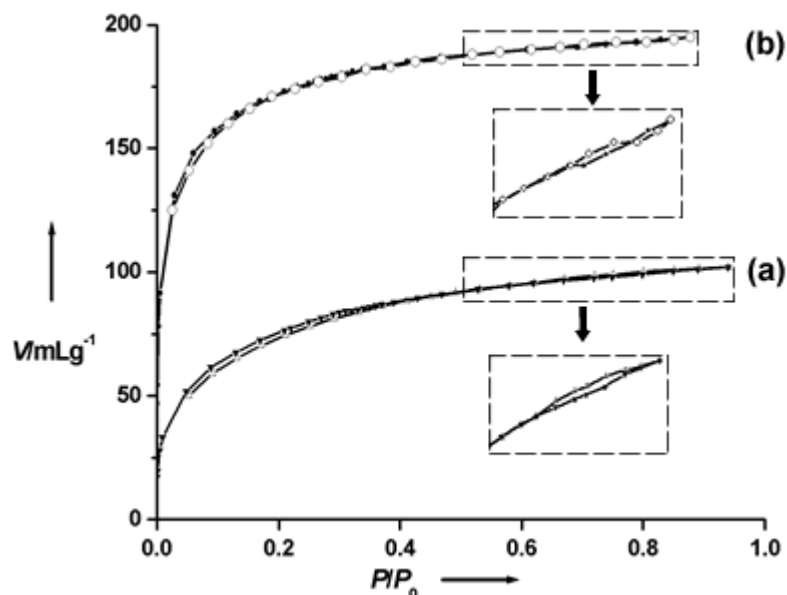


Figure 5. Nitrogen adsorption-desorption isotherms: (a) 2DMIO and (b) 3DMIO after ethanol extraction. The inset shows an enlarge region of the curves between relative pressures of 0.6 and 0.8.

3-2-2 3D mesoporous Fe_2O_3

This approach can also be used to prepare three-dimensional mesoporous iron oxide by adjusting the aging temperature. When the Fe^{III} ethoxide-decylamine mixture is further aged at $150 \text{ }^\circ\text{C}$, ordered three-dimensional (3D) cubic mesoporous iron oxide (3DMIO) with $\text{Fm}3\text{m}$ symmetry is obtained.

CHN analysis confirms the successful template removal from 3DMIO. As-prepared 3DMIO contained 37.9% C, 8.80% H, and 4.14% N, while for 3DMIO after ethanol extraction the values were 7.08% C, 1.71% H, and 0.35% N. Based on the N analysis, about 92% of the template had been removed from 3DMIO, which is similar to that for 2DMIO (~ 94%). Slightly high C and H contents were also observed after template removal and this may be due to the same reason that a small amount of ethanol remains in the pores.

TEM images recorded along different directions are shown in Figure 6. These images represent the highly ordered mesoporous structure of 3DMIO by examining many particles in different regions. Combining all the images, a cubic Fm3m symmetry of 3DMIO could be proposed.

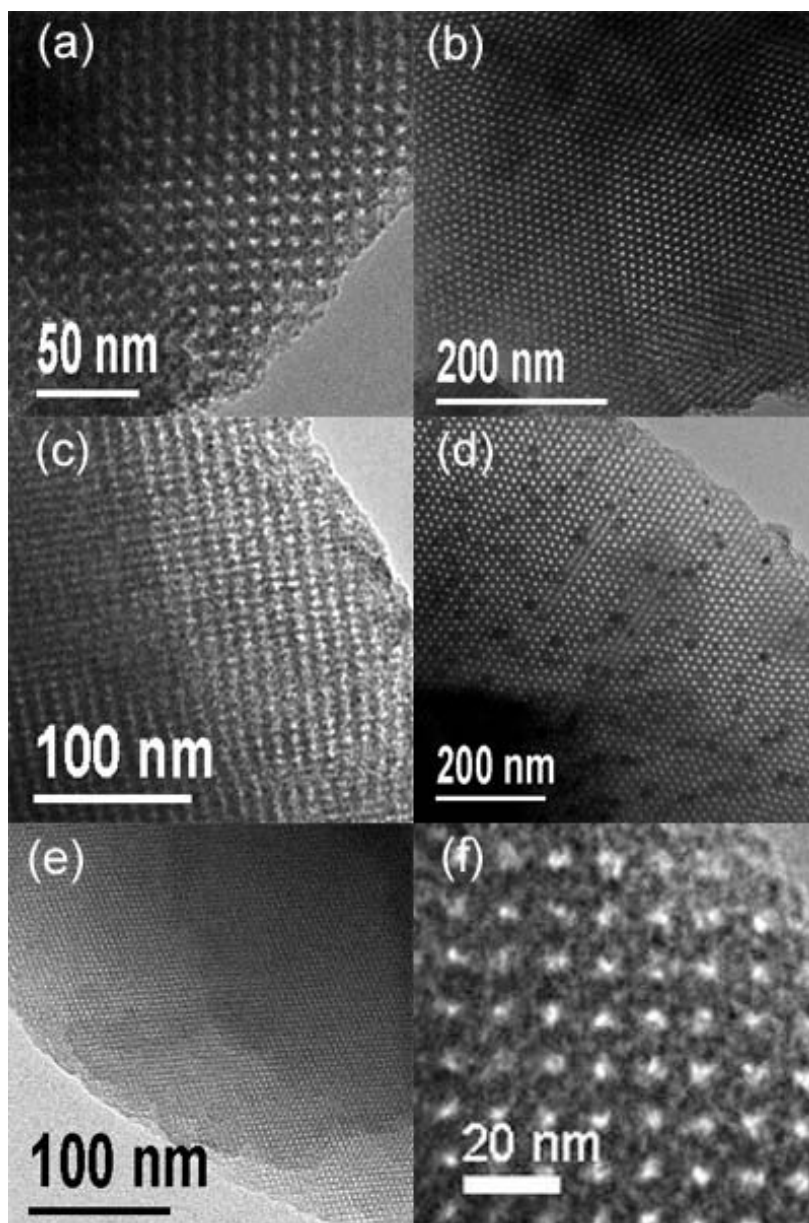


Figure 6. (a-e) TEM images for 3DMIO recorded along different directions; (f) HRTEM image for 3DMIO.

Mössbauer measurements (Figure 7) confirmed that the oxidation state is +3. A doublet was observed which indicates that there is no magnetic order in 3DMIO and the splitting indicated superparamagnetic behaviour similar to 2DMIO. The low-angle PXRD results (Figure 8) show a diffraction peak at $2\theta = 1.06^\circ$, corresponding to a

d -spacing of 104.6 Å. The unit cell parameter a_0 calculated from the PXRD pattern is 182 Å, which is in reasonable agreement with $a_0 = 192$ Å observed from the TEM analysis. Microporosity similar to that observed in 2DMIO is seen in the 3DMIO by HRTEM (Figure 6f) and in the N₂ adsorption-desorption analysis (Figure 5b). The BET surface area calculated from the desorption isotherm is approximately 610 m²g⁻¹, which is about twice that for 2DMIO, due perhaps to the higher accessible pore surface in the three dimensional structure.

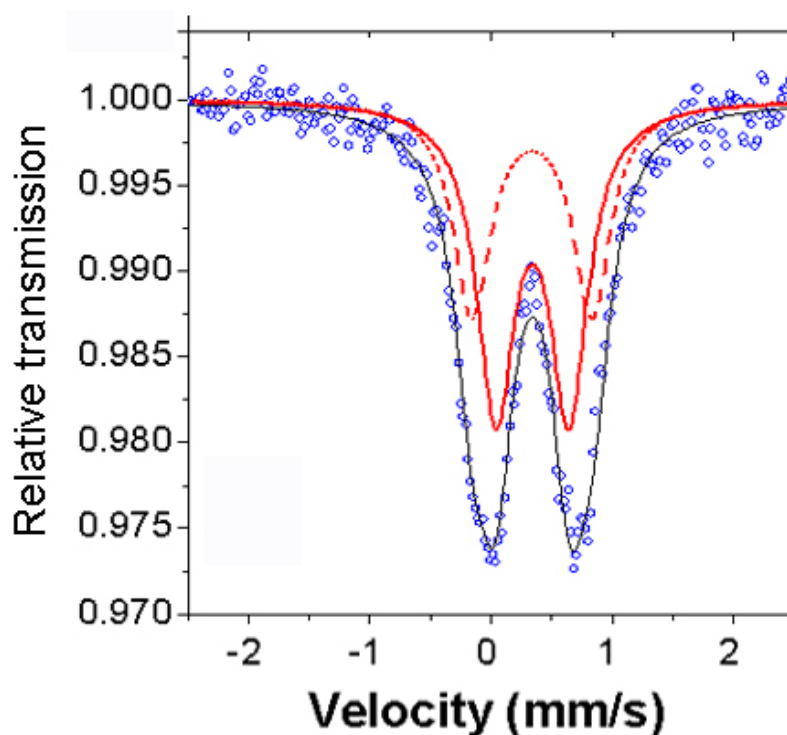


Figure 7. Mössbauer data for 3DMIO.

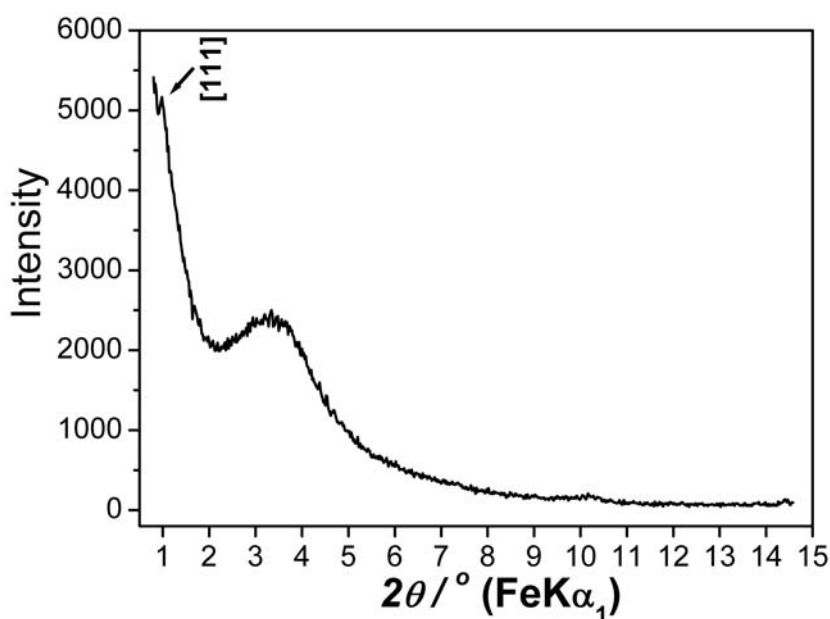


Figure 8. Low-angle PXRD pattern for 3DMIO.

3-3 Conclusions

2D and 3D mesoporous Fe_2O_3 have been synthesized for the first time using alkyl amine as surfactant and iron ethoxide as precursor. The simultaneous presence of microporosity and mesoporosity is unusual, especially in a transition metal compound. This is first time alkyl amine templates have been used as bi-functional surfactants, which can template micro- as well as meso-structures.

3-4 References

- ¹ P. D. Yang, D. Y. Zhao, D. I. Margolese, B. F. Chmelka, and G. D. Stucky, *Nature*, 1998, **396**, 152.
- ² D. M. Antonelli, A. Nakahira, and J. Y. Ying, *Inorganic Chemistry*, 1996, **35**, 3126.
- ³ D. M. Antonelli and J. Y. Ying, *Angewandte Chemie-International Edition in English*, 1995, **34**, 2014.
- ⁴ D. Larcher, C. Masquelier, D. Bonnin, Y. Chabre, V. Masson, J. B. Leriche, and J. M. Tarascon, *Journal of the Electrochemical Society*, 2003, **150**, A133.

- ⁵ F. Jiao and P. G. Bruce, *Angewandte Chemie-International Edition*, 2004, **43**, 5958.
- ⁶ D. Y. Zhao, J. L. Feng, Q. S. Huo, N. Melosh, G. H. Fredrickson, B. F. Chmelka, and G. D. Stucky, *Science*, 1998, **279**, 548.
- ⁷ J. S. Beck, J. C. Vartuli, W. J. Roth, M. E. Leonowicz, C. T. Kresge, K. D. Schmitt, C. T. W. Chu, D. H. Olson, E. W. Sheppard, S. B. McCullen, J. B. Higgins, and J. L. Schlenker, *Journal of the American Chemical Society*, 1992, **114**, 10834.
- ⁸ J. Liu, X. Zhang, Y. Han, and F. S. Xiao, *Chemistry of Materials*, 2002, **14**, 2536.
- ⁹ Y. Han, F. S. Xiao, S. Wu, Y. Y. Sun, X. J. Meng, D. S. Li, S. Lin, F. Deng, and X. J. Ai, *Journal of Physical Chemistry B*, 2001, **105**, 7963.

Chapter 4. Synthesis, characterization, and magnetic properties of mesoporous transition metal oxides prepared by the hard template method

4-1 Mesoporous Fe₂O₃ with crystalline walls: synthesis, structural characterization, and magnetic properties

Iron oxides represent a particularly important class of materials capable of use in a wide range of applications, including: catalysis, in magnetic devices, and in rechargeable lithium batteries.¹⁻³ They combine such functionality with low cost and low toxicity. Porous Fe₂O₃ with disordered and ordered mesoporous structures have been prepared using soft templating methods (See Chapter 3).⁴ However, such methods invariably lead to mesoporous materials with amorphous walls. Hard templating offers an alternative route to the formation of mesoporous Fe₂O₃. Although, in general, the formation of mesoporous transition metal oxides by the hard template method yields materials with highly crystalline walls, this has not been the case for Fe₂O₃.⁵ Yet such crystallinity is expected to have an important influence on the properties of the resulting mesoporous materials, especially their magnetic behaviour. It is therefore critical to synthesize ordered mesoporous Fe₂O₃ with crystalline walls. Here the first synthesis of ordered mesoporous Fe₂O₃ with highly crystalline walls has been demonstrated. This material exhibits unique magnetic properties, differing from bulk α -Fe₂O₃, nanoparticulate α -Fe₂O₃ and mesoporous Fe₂O₃ with disordered walls.

4-1-1 Experimental section

In a typical synthesis of mesoporous α -Fe₂O₃, 1 gram of Fe(NO₃)₃·9H₂O (98% Aldrich) was dissolved in 20 ml of ethanol followed by addition of 1 g of mesoporous silica KIT-6 (3D pore structure). The silica template was prepared according to the procedure described by Ryoo and co-workers. After stirring the mixture at room temperature until nearly dry powder had been obtained, the sample was heated slowly to 300 °C and calcined at that temperature for 3h. The impregnation procedure was repeated, followed by calcination at 500 °C for 3h resulting in mesoporous α -Fe₂O₃ with disordered walls. For the synthesis of mesoporous α -Fe₂O₃ with ordered walls, 1.5 g of Fe(NO₃)₃·9H₂O (98% Aldrich) was used. After stirred at room temperature until a fine and completely dry powder was formed, the sample was heated slowly to 600 °C and kept at that temperature

for 6h. Such differences in the synthesis conditions are sufficient to change significantly the atomic ordering within the walls and have a profound influence on the magnetic behaviour, as demonstrated later. The resulting samples were treated three times with hot 2M NaOH, to remove the silica template, centrifuged, washed several times with water and ethanol then dried at 60 °C in air.

To explore the co-operative magnetism in mesoporous α -Fe₂O₃ with ordered walls in greater detail, neutron powder diffraction analysis was taken on this form of the material at approximately 298 K on the diffractometer ROTAX at the ISIS Facility, Rutherford Appleton Laboratory, UK. The lattice parameters and the diffraction peak profile parameters were determined using a LeBail fit as implemented in the GSAS suite of programs. The shapes of the broadened peaks were modelled using pure Lorentzian functions. Crystal and magnetic structural parameters were refined using the Rietveld code in GSAS. An empirical absorption parameter for the wavelength-specific absorption of neutrons by the sample was refined.

4-1-2 Results and discussion

4-1-2-1 Mesoporous structure

Transmission electron micrographs (TEM) of mesoporous Fe₂O₃ with ordered walls are shown in Figure 1. The first image (Figure 1a) recorded at low magnification shows at least 90 % of the α -Fe₂O₃ particles exhibit a mesostructure. TEM images with a higher magnification (Figure 1b-d) were recorded along different directions, showing a highly ordered mesostructure. Based on these TEM data, this ordered mesoporous Fe₂O₃ with ordered walls has a symmetry Ia-3d, replicating that of the mesoporous silica KIT-6 template used in its formation. A lattice parameter, $a_0 = 232 \text{ \AA}$, was obtained from the TEM data. Figure 2 show the corresponding views of the α -Fe₂O₃ with ordered mesopores but disordered walls. A highly regular mesoporous structure can also be observed in most particles, with a symmetry Ia-3d, replicating that of the KIT-6 silica template used in their formation. In the case of α -Fe₂O₃ with disordered walls a lattice repeat, $a_0 = 210 \text{ \AA}$ is obtained, which is slightly smaller than that for mesoporous Fe₂O₃ with ordered walls.

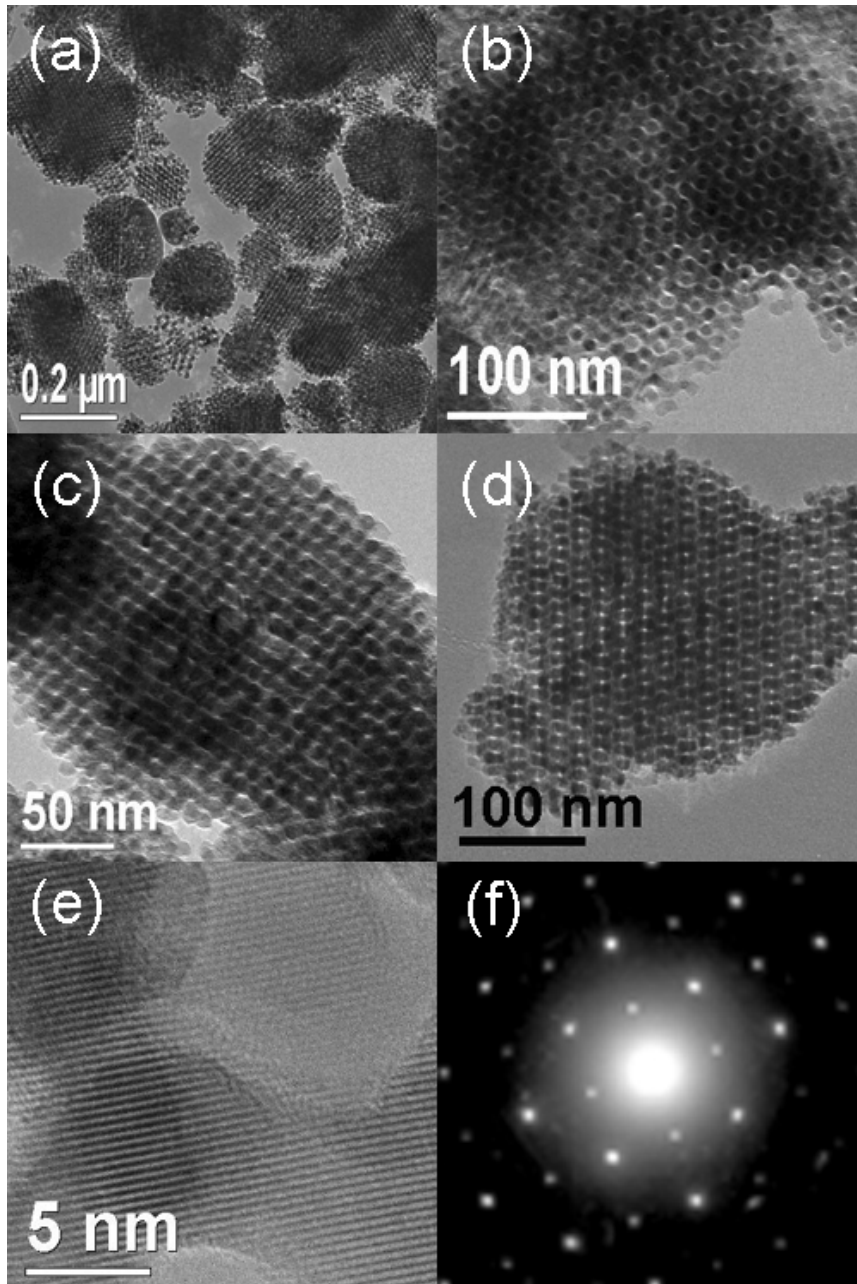


Figure 1. TEM images for mesoporous $\alpha\text{-Fe}_2\text{O}_3$ with ordered walls recorded (a) at very low magnification and along (b) [111], (c) [110], and (d) [311] directions; HRTEM image of (b) is shown in (e); (f) SAED patterns for mesoporous $\alpha\text{-Fe}_2\text{O}_3$ with ordered walls.

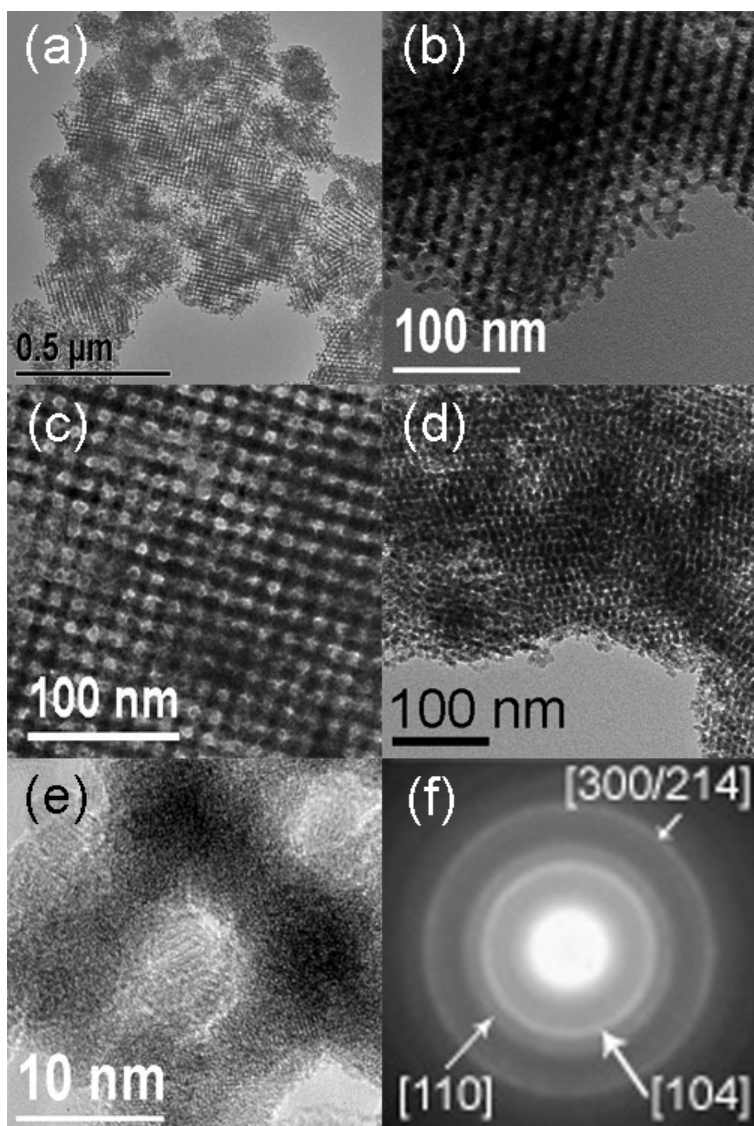


Figure 2. TEM images for mesoporous α -Fe₂O₃ with disordered walls recorded (a) at very low magnification and along (b) [111], (c) [100], and (d) [311] directions; HRTEM image of (c) is shown in (e); (f) SAED patterns for mesoporous α -Fe₂O₃ with disordered walls.

Low angle powder X-ray diffraction data for the two forms of mesoporous α -Fe₂O₃ are shown in Figure 3. Considering first the low angle data for the highly crystalline material (Figure 3A), two peaks are evident with the lower peak, [211] reflection in space group Ia-3d, corresponding to an a_0 parameter of 229 Å, in good agreement with the a_0 parameter, 232 Å obtained from TEM images, Figure 1. Although the degree of mesoporous ordering appeared from the TEM data to be similar for α -Fe₂O₃ with and

without ordered walls, only a single peak is evident in the low-angle diffraction data of the latter. The low angle PXRD peak in Figure 3(B) corresponds to a unit cell parameter of 221 Å, in good agreement with the date calculated from TEM analysis (210 Å). This is ~4% smaller than that for the crystalline material indicating that the differences in the degree of ordering within the walls have an effect on the mesoporous structure.

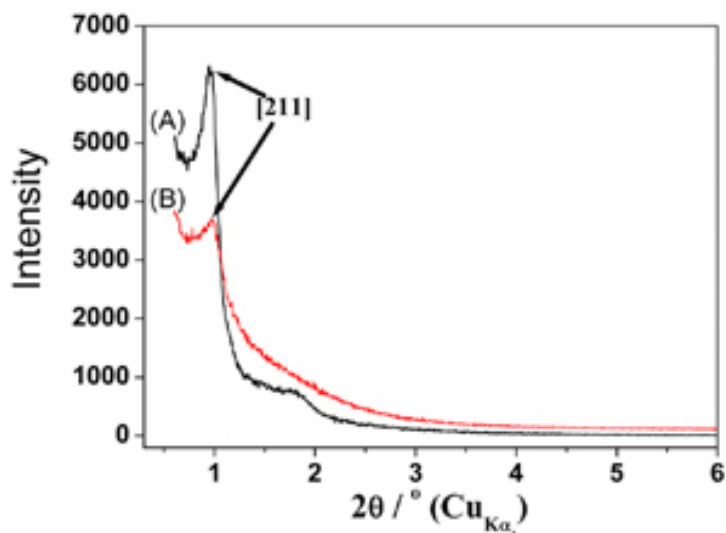


Figure 3. Low-angle XRD patterns for mesoporous α -Fe₂O₃ (A) with ordered walls and (B) with disordered walls.

In order to examine the pore size and its distribution, nitrogen adsorption-desorption measurements were carried out, Figure 4. In both cases, a type IV isotherm is observed. For the material with disordered walls, the type IV isotherm is less well defined which may be caused by a contribution from interparticle voids. However, the isotherms are similar to those observed for other mesoporous transition metal oxides formed by using hard template method.⁶ The pore size distributions, calculated from the desorption isotherms, are shown in the inset in Figure 4. For mesoporous α -Fe₂O₃ with ordered walls, the pore size is centred at a diameter of 3.85 nm and this is in good agreement with the pore diameters anticipated for a replica structure of KIT-6. For the sample with disordered walls, the pore size distribution is slightly wider and centred at a diameter of 3.78 nm, which is slightly smaller than the ordered material. The surface areas estimated from the Brunauer-Emmett-Teller (BET) method were also obtained from the nitrogen adsorption-desorption measurements and are 139 m²g⁻¹ and 210 m²g⁻¹ for the mesoporous α -Fe₂O₃ with ordered

and disordered walls, respectively. Whilst the origin of the difference is not clear at this moment, it is interesting to note that the pore size distribution appears to be somewhat greater in the case of the mesopore with disordered walls; this combined with the high surface area may indicate that the pore surface is rougher for the mesopore with disordered walls.

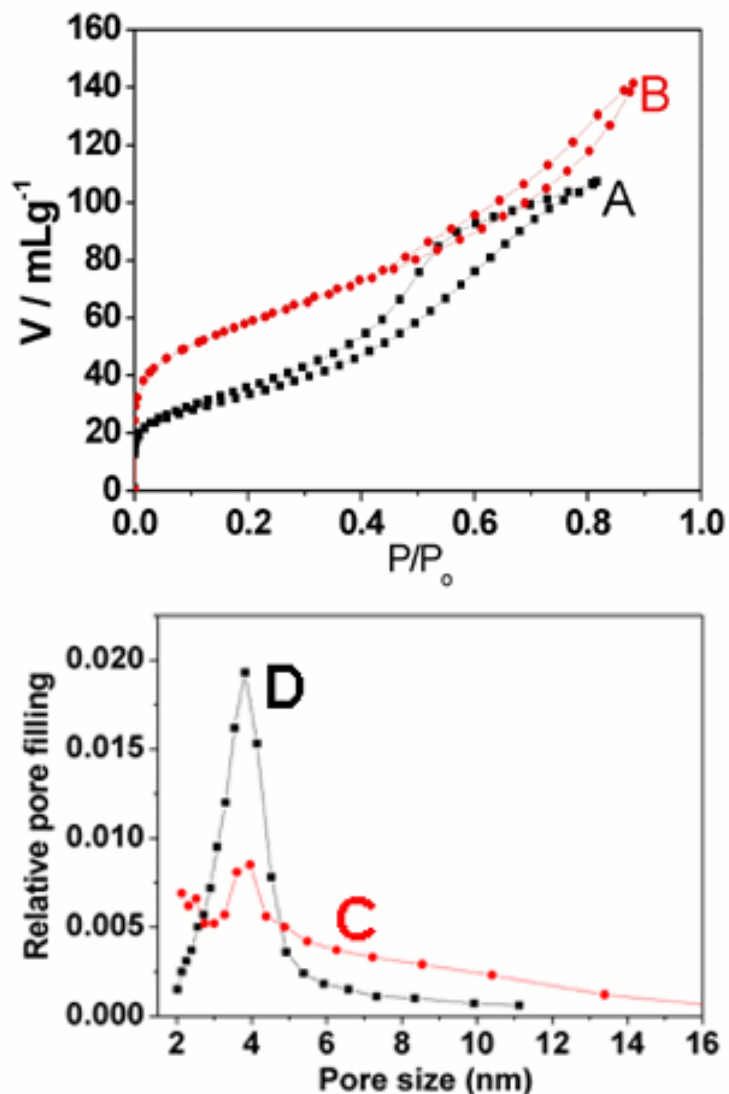


Figure 4. Nitrogen adsorption-desorption isotherms for mesoporous α -Fe₂O₃ (A) with ordered walls and (B) with disordered walls. The lower figure shows the pore size distributions for mesoporous α -Fe₂O₃ (C) with ordered walls and (D) with disordered walls.

4-1-2-2 Structure within the walls

Turning to the order within the walls, the high resolution image, Figure 1(e), demonstrates the high degree of atomic order in the walls of the ordered material. Not only are the walls crystalline but the lattice fringes indicate that there is a considerable degree of structural coherence throughout each particle, implying a near single crystal like arrangement of atoms within the walls. This is confirmed by selected area electron diffraction (SAED), Fig. 1(f), which exhibits a single crystal diffraction pattern. Wide angle PXRD data for the materials are shown in Figure 5. Well defined peaks corresponding to the crystal structure of α -Fe₂O₃ are clearly evident, in agreement with the HRTEM and SAED data. Although the high resolution image of the disordered material, shown in Figure 2(e), appears to demonstrate little evidence of order within the walls, a SAED pattern shows several diffraction rings corresponding to the d-spacings expected for α -Fe₂O₃, Figure 2(f). This is confirmed by the wide angle PXRD data in Figure 5, which clearly shows peaks corresponding to α -Fe₂O₃. However, the peaks are weak and broad compared with those for ordered α -Fe₂O₃, Figure 5(B). The SAED and PXRD data indicate that the walls of so called disordered Fe₂O₃ are not amorphous but contain small crystallites of α -Fe₂O₃ (~6 nm based on analysis of the PXRD peak widths by the Scherrer formula) that are orientationally disordered with respect to each other. This is consistent with EXAFS analysis presented later. It may be difficult to rule out the coexistence of some amorphous α -Fe₂O₃ but given that iron oxide is not a glass former, it is likely that the walls are composed of the α -Fe₂O₃ nanocrystallites. Note that the wall thickness is ~ 7 nm based on the pore dimensions of the KIT-6 template from which the mesoporous Fe₂O₃ is formed. 'Ordered' and 'disordered' will be used to refer to the two forms of mesoporous α -Fe₂O₃ recognizing the fact that the former consist of near single crystal like mesoporous particles, whereas the latter possesses α -Fe₂O₃ nanocrystallites.

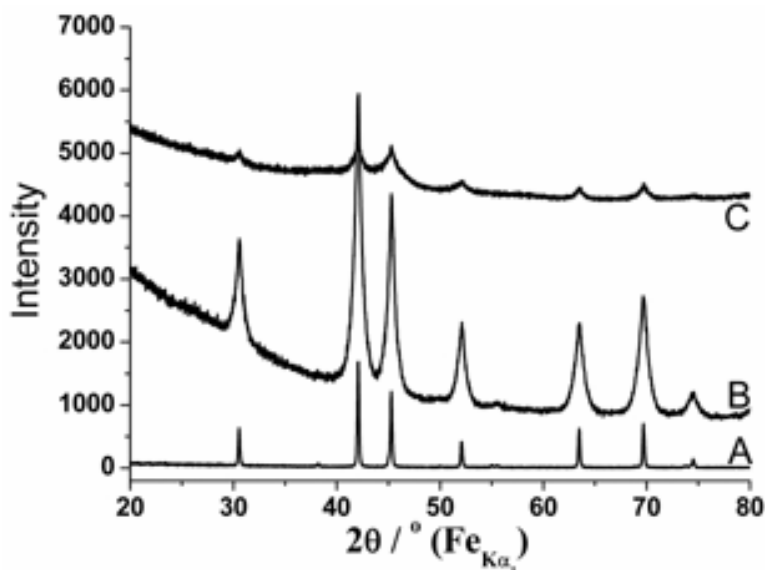


Figure 5. Wide-angle PXRD patterns: (A) bulk α -Fe₂O₃; (B) mesoporous α -Fe₂O₃ with ordered walls; (C) mesoporous α -Fe₂O₃ with disordered walls.

Confirmation that the iron ions are in the +3 oxidation state for both mesoporous materials was obtained by X-ray absorption near-edge structure (XANES) analysis, Figure 6.[†] Extended X-ray absorption fine structure (EXAFS) data collected simultaneously are shown in Figures 7.^{††} Data for bulk α -Fe₂O₃ are shown for comparison. Inter-atomic distances and R-factors indicating the goodness-of-fit are shown in Table 1. There is excellent agreement between the Fe-O bond lengths for all three samples, the standard bulk material and the two mesoporous phases, Figure 7. Considering the next nearest neighbour Fe-Fe distances, it is evident from Figure 7 that there is very good agreement between the crystalline mesoporous α -Fe₂O₃ and the bulk phase, which is not surprising given the extended crystalline nature of the walls in the mesoporous α -Fe₂O₃. Although the Fe-Fe peaks in Figure 7 for the disordered α -Fe₂O₃ mesopore are weaker, three peaks are again apparent corresponding to the 3 Fe-Fe distances observed for the crystalline mesopore and the bulk material, consistent with the presence of nanocrystallites of α -Fe₂O₃ in the walls of the disordered material. Reduction in peak intensities as the crystallite size is reduced to the nanometre range has been demonstrated before.⁷

[†] The XAS (XANES and EXAFS) analysis was done by Prof. Alan Chadwick at University of Kent, UK.

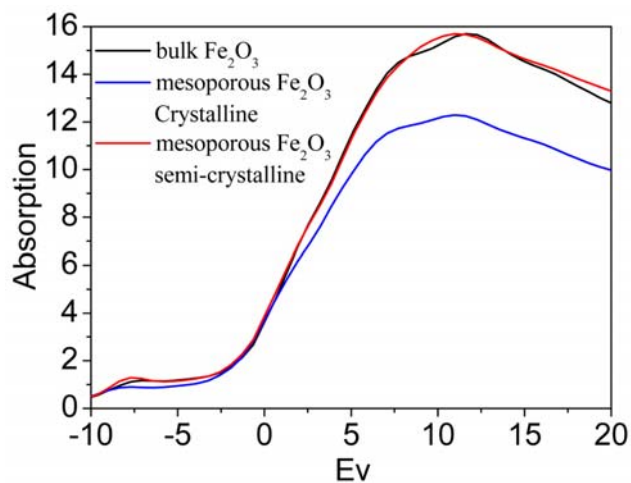


Figure 6. XANES spectra for bulk α -Fe₂O₃ (black line), mesoporous α -Fe₂O₃ with ordered walls (blue line), and mesoporous α -Fe₂O₃ with disordered walls (red line).

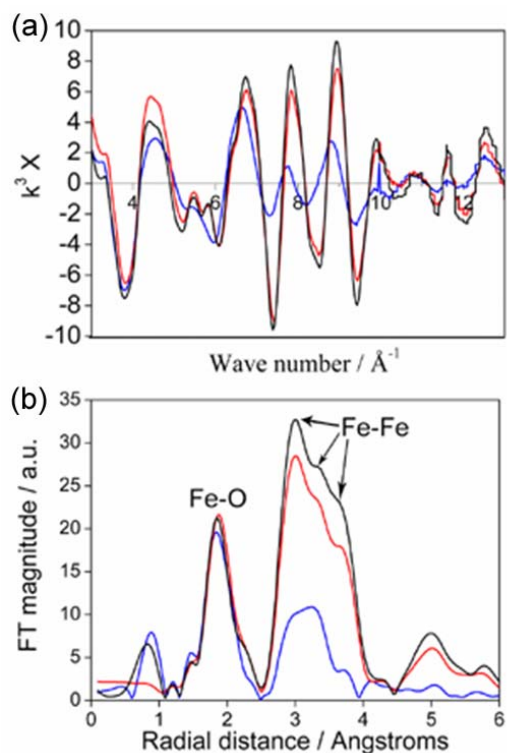


Figure 7. (a) Fe K-edge EXAFS spectrum for bulk α -Fe₂O₃ (black line), mesoporous α -Fe₂O₃ with ordered walls (red line), and mesoporous α -Fe₂O₃ with disordered walls (blue line). (b) The Fourier transform of the data shown in (a) for bulk α -Fe₂O₃ (black line), mesoporous α -Fe₂O₃ with ordered walls (red line), and mesoporous α -Fe₂O₃ with disordered walls (blue line).

Simplified XRD			Bulk α -Fe ₂ O ₃				Mesoporous α -Fe ₂ O ₃ with ordered walls				Mesoporous α -Fe ₂ O ₃ with disordered walls			
Atom	CN	R	Atom	CN	R	A	Atom	CN	R	A	Atom	CN	R	A
O	3	1.957	O	3	1.946	0.017	O	3	1.927	0.013	O	3	1.951	0.019
O	3	2.098	O	3	2.139	0.032	O	3	2.11	0.019	O	3	2.164	0.059
Fe	4	2.97	Fe	4	2.963	0.016	Fe	4	2.954	0.018	Fe	4	3.022	0.034
Fe	3	3.368	Fe	3	3.344	0.022	Fe	3	3.357	0.018	Fe	3	3.383	0.05
O	3	3.392	O	3	3.387	0.005	O	3	3.421	0.006	O	3	3.414	0.027
O	3	3.601	O	3	3.827	0.022	O	3	3.631	0.015	O	3	3.686	0.011
Fe	6	3.704	Fe	6	3.694	0.019	Fe	6	3.692	0.022	Fe	6	3.516	0.106
			R=34.38%				R=33.26%				R=36.34%			

Table 1. EXAFS results for bulk α -Fe₂O₃, mesoporous α -Fe₂O₃ with ordered and disordered walls. R is the distance (Å) and A is the Debye-Waller factor.

4-1-2-3 Magnetic Behaviour

The magnetic behaviour was first investigated by Mössbauer spectroscopy carried out on the two mesoporous α -Fe₂O₃ phases. The results are shown in Figure 8. Data for mesoporous α -Fe₂O₃ with disordered walls correspond to the doublet expected for high-spin Fe³⁺ in an octahedral oxygen environment, where the neighbouring spins do not induce order extending over a long-range. The quadrupole splitting is 0.76 mm/s, which is consistent with superparamagnetic behaviour identified in Mössbauer measurements of nanoparticulate α -Fe₂O₃ with a particle size below 8 nm.^{8,9} In other words, the long range magnetic order present in bulk α -Fe₂O₃ breaks down when the crystalline size is below 8 nm. This is consistent with the walls of the disordered material, containing α -Fe₂O₃ nanoparticles of ~ 6 nm. The data for mesoporous Fe₂O₃ with ordered walls exhibits the classic sextet spectrum of α -Fe₂O₃ in the bulk phase, typical of the long range magnetic ordering between spins in this material.¹⁰ The data show that despite the wall thickness in mesoporous α -Fe₂O₃ being less than 8 nm (based on the KIT-6 pore size), Figure 8(B), long range order exists.

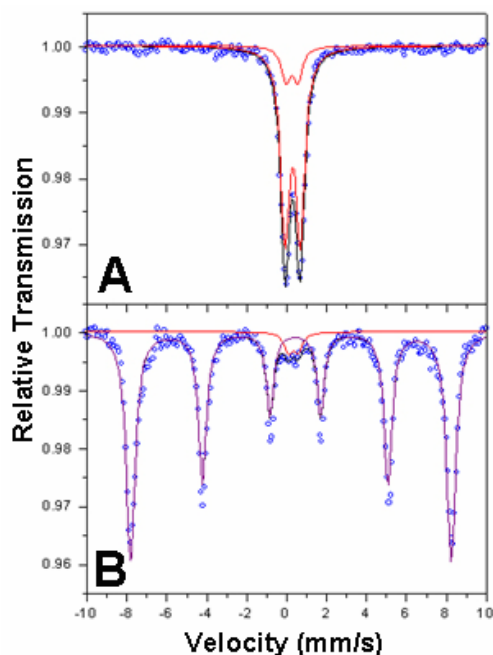


Figure 8. Mössbauer spectra for mesoporous α -Fe₂O₃ (A) with disordered walls and (B) with ordered crystalline walls.

It can be concluded that there are sufficient spin interactions occurring along the walls, *i.e.* within the continuous 2D sheet of α -Fe₂O₃ that forms the walls, to align the neighbouring spins. This emphasizes the unique properties of mesoporous α -Fe₂O₃ with ordered crystalline walls.

A more detailed characterization of the unique magnetic properties of mesoporous α -Fe₂O₃ with crystalline walls was carried out by magnetization and neutron diffraction measurements. The results of magnetization measurements are presented in Figure 9. Before considering the magnetism of the mesoporous materials, it is useful to recall the behaviour of bulk α -Fe₂O₃. Between the Néel temperature, T_N , of approximately 961 K and the Morin transition temperature, T_M , at \sim 265 K, the spins in α -Fe₂O₃ lie flat in the [111] planes of the rhombohedral cell such that the spins in each layer are approximately parallel to each other, but antiparallel to those in adjacent layers.¹¹⁻¹³ A Dzyaloshinski-Moriya interaction gives rise to a small canting of moments within each [111] plane, and these produce a new ferromagnetic moment of the order of 0.005 μ_B /iron atom. This phase is referred to as the weakly ferromagnetic (WF) form. Below T_M the moments rotate through almost 90° to lie nearly perpendicular to c-axis.^{14, 15} This phase – referred to as the

antiferromagnetic (AF) form - has no net magnetization, and so a sharp drop in susceptibility is expected at T_M . The sample of bulk α -Fe₂O₃ shows this very clearly, Figure 9(C).

The ordered mesoporous material shows a splitting between the field-cooled (FC) and zero-field-cooled (ZFC) data from the highest experimental temperature, compatible with some degree of spontaneous moment over the entire temperature range studied. There are also features suggestive of magnetic transitions in the region of 260 K and 75 K. The first of these is close to the Morin transition temperature, T_M , of bulk α -Fe₂O₃. However, the expected sharp drop in susceptibility at the Morin temperature does not occur, suggesting that mesoporous α -Fe₂O₃ with ordered walls does not go through such a transition over the temperature range of our measurements. It is well known that the Morin transition is sensitive to the size of the structural domains in α -Fe₂O₃ – so, for example, T_M is less than 4K for α -Fe₂O₃ particles of diameter 8 – 20 nm.^{8, 9, 16-19} It is possible that the confined dimension of the walls plays a role in suppressing T_M . In summary, despite the fact that understanding the transition at 265 K in the ordered material will require further study, the important conclusion can be drawn that the confined dimensions of crystalline α -Fe₂O₃ in the ordered mesoporous material is sufficient to suppress the Morin transition but not to suppress the long range magnetic order.

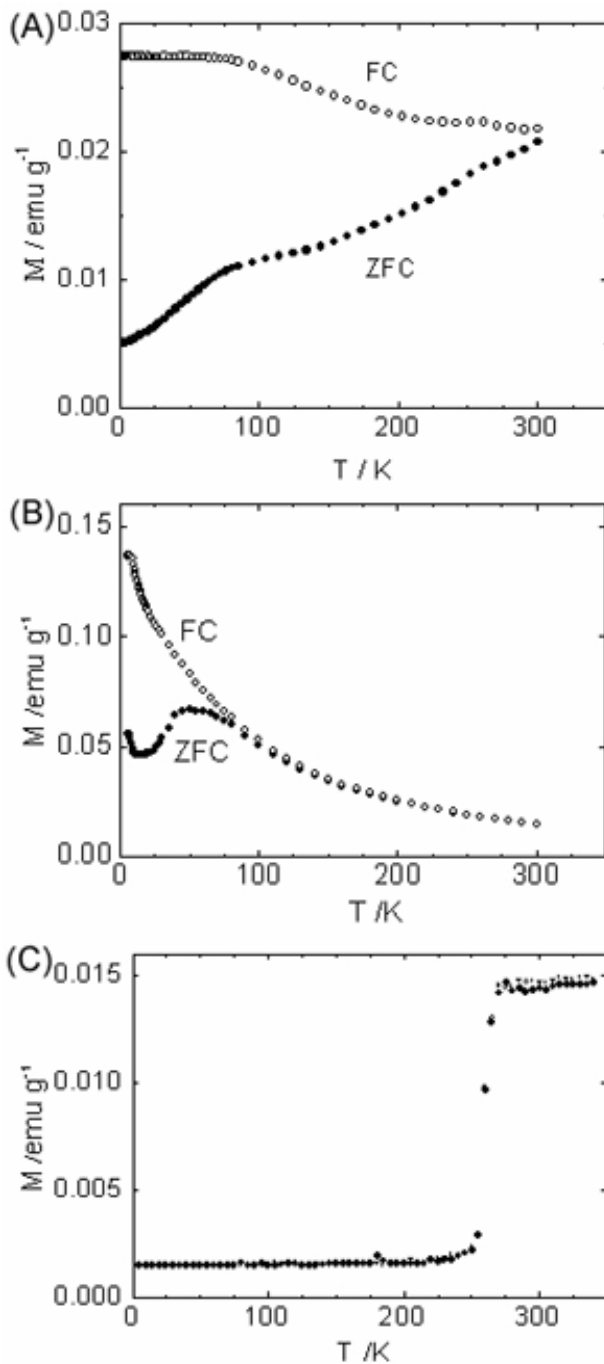


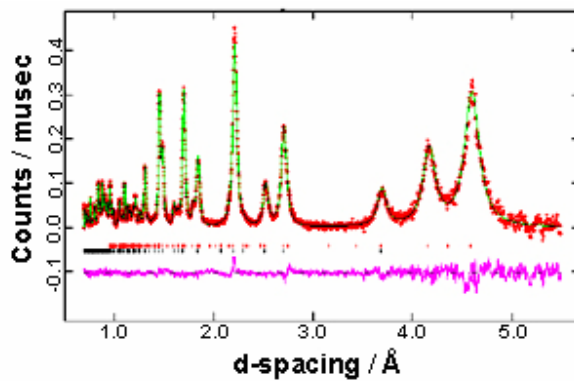
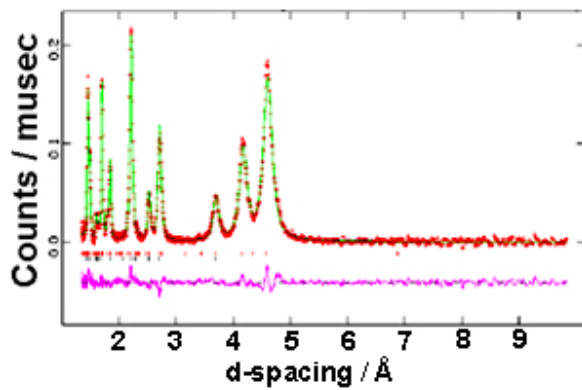
Figure 9. Magnetization data for the mesoporous $\alpha\text{-Fe}_2\text{O}_3$ (A) with ordered walls and (B) with disordered walls, taken in 0.01 T after first cooling in zero field (ZFC, closed circles) and then in an applied field of 0.01 T (FC, open circles). (C) shows the results of the same measurement on bulk $\alpha\text{-Fe}_2\text{O}_3$ prepared from the same iron sources with the same heating treatment.

The feature in the magnetization in the region of 75 K is also difficult to assign. Transitions of a similar form are observed in ferrihydrite, $\text{Fe}_2\text{O}_3 \cdot n\text{H}_2\text{O}$, but we believe it is very unlikely that any of this material is formed during the synthesis. It is more likely that this feature arises from a few regions of the sample composed of small crystallites and behaving more like finely-particulate $\alpha\text{-Fe}_2\text{O}_3$ than the bulk material.^{8,9,16-19} Such particles may possess a spontaneous magnetization down to 5K that is as large as that observed in the WF phase of the bulk material, and behave as superparamagnets at room temperature. On cooling, a blocking transition has been observed at a temperature, T_B , which is expected to depend on particle size: for example, for particles of 16 nm diameter, T_B is in the region of 25 – 30 K.¹⁷ It is conceivable therefore that the transition we observe around 75 K stems from regions of the material with short structural coherence lengths.

The most prominent feature of the susceptibility data for the mesoporous $\alpha\text{-Fe}_2\text{O}_3$ with disordered walls is a cusp near 50 K, above which there is FC-ZFC divergence. There is no sign of a Morin transition near that of the bulk material. In both respects, the collective magnetic properties of this material have similarities with those of small particles of $\alpha\text{-Fe}_2\text{O}_3$, with the suppression of the Morin transition and some form of blocking transition at a temperature that depends on the nature of the structural correlation length.

To examine the magnetic order in mesoporous $\alpha\text{-Fe}_2\text{O}_3$ with crystalline walls in more detail, neutron powder diffraction data were collected at room temperature. These data are shown in Figure 10, together with the Rietveld fit, performed using the GSAS package. The diffraction peaks are significantly broadened with respect to the instrument resolution of the neutron diffractometer. In addition to the diffraction peaks from the hematite crystal structure, peaks characteristic of the long-range magnetic order of the Fe^{3+} moments are observed. Most prominent is the peak centred near 4.6 Å, which may be indexed as [003] in the hexagonal setting of space group R-3c. This is characteristic of the WF magnetic phase, and absent in the AF phase. Rietveld refinement of the data was performed in space group R-3c, with Fe at (0, 0, z) and O at (x, 0, 1/4). The magnetic structure was refined in the space group P1, with the same dimensions as the nuclear unit cell, and, initially, the same disposition of moments found in the AF phase of bulk $\alpha\text{-Fe}_2\text{O}_3$. The form factor for Fe^{3+} was the spherical $\langle j_0 \rangle$ expansion implemented in GSAS. The introduction to the refinement of a component of moment perpendicular to the hexagonal c-

axis led to an unstable refinement, and did not improve the fit, so was abandoned; the small ferromagnetic component perpendicular to the hexagonal c-axis was neglected in these calculations. Refined parameters are in good agreement with previous studies of the crystal and magnetic structure and are as follows: $a = b = 5.03726(1) \text{ \AA}$; $c = 13.7663(5) \text{ \AA}$; cell volume = $302.497(13) \text{ \AA}^3$; $z(\text{Fe}) = 0.354986(35)$; $u(\text{Fe}) = 0.0097(2) \text{ \AA}^2$; $x(\text{O}) = 0.3074(1)$; $u(\text{O}) = 0.0075(2) \text{ \AA}^2$; magnetic moment of $\text{Fe}^{3+} = 4.02(2) \mu_{\text{B}}$ parallel to the hexagonal c-axis; weighted R(wp) 2.3 %; $\chi^2 = 1.9$.^{11, 14, 20, 21} The results of the neutron diffraction confirmed the existence of long range magnetic order in the mesoporous $\alpha\text{-Fe}_2\text{O}_3$ with crystalline walls.



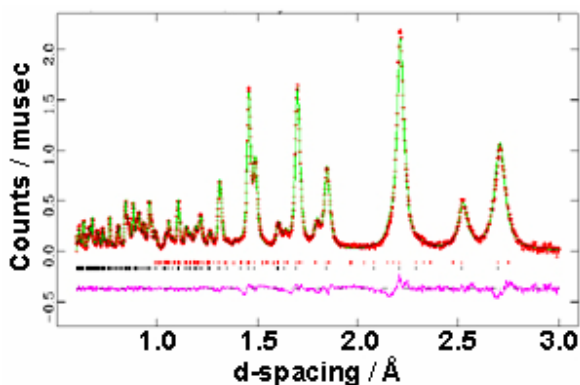


Figure 10. Powder neutron diffraction pattern for α -Fe₂O₃ with ordered walls collected at 298 K on three different detector banks at ROTAX: from top to bottom, the angle of the banks are at two-theta = 21.9°, 61.5° and 120.9° respectively. In each case the data (crosses) have been fitted (upper line through the data points) by Rietveld analysis to a nuclear and magnetic structure, depicted by the lower and upper tick marks respectively. The line at the bottom of each plot represents the difference between the data and the calculated profile.

4-1-3 Conclusions

α -Fe₂O₃ with an ordered mesoporous structure and crystalline walls has been prepared for the first time, and compared with α -Fe₂O₃ with an ordered mesoporous structure and disordered walls. The former exhibits near single crystal like order throughout the walls of each particle, whereas the walls of the later contain nanocrystallites of α -Fe₂O₃ (~ 6 nm) that are orientationally disordered with respect to each other. The magnetic behaviour of mesoporous α -Fe₂O₃ with disordered/amorphous walls is consistent with that of α -Fe₂O₃ nanoparticles of less than 8 nm, i.e. no long range magnetic order, absence of a Morin transition and the presence of superparamagnetic behaviour. The magnetic behaviour of mesoporous α -Fe₂O₃ with crystalline walls is unique. Mössbauer, magnetization susceptibility and powder neutron diffraction all indicate that despite the wall thickness being less than 8 nm, long range magnetic ordering persists due to interaction between Fe³⁺ ions along the walls. The material exhibits weakly ferromagnetic susceptibility and Bragg scattering characteristic of the WF phase of bulk α -Fe₂O₃. However, the confined dimensions are sufficient to suppress the Morin transition present in bulk α -Fe₂O₃.

4-1-4 References

- ¹ F. Jiao, B. Yue, K. K. Zhu, D. Y. Zhao, and H. Y. He, *Chemistry Letters*, 2003, **32**, 770.
- ² D. Larcher, C. Masquelier, D. Bonnin, Y. Chabre, V. Masson, J. B. Leriche, and J. M. Tarascon, *Journal of the Electrochemical Society*, 2003, **150**, A133.
- ³ C. Cannas, D. Gatteschi, A. Musinu, G. Piccaluga, and C. Sangregorio, *Journal of Physical Chemistry B*, 1998, **102**, 7721.
- ⁴ F. Jiao and P. G. Bruce, *Angewandte Chemie-International Edition*, 2004, **43**, 5958.
- ⁵ B. Z. Tian, X. Y. Liu, H. F. Yang, S. H. Xie, C. Z. Yu, B. Tu, and D. Y. Zhao, *Advanced Materials*, 2003, **15**, 1370.
- ⁶ B. Z. Tian, X. Y. Liu, L. A. Solovyov, Z. Liu, H. F. Yang, Z. D. Zhang, S. H. Xie, F. Q. Zhang, B. Tu, C. Z. Yu, O. Terasaki, and D. Y. Zhao, *Journal of the American Chemical Society*, 2004, **126**, 865.
- ⁷ S. R. Davis, A. V. Chadwick, and J. P. Wright, *Journal of Physical Chemistry B*, 1997, **101**, 9901.
- ⁸ R. D. Zysler, D. Fiorani, A. M. Testa, L. Suber, E. Agostinelli, and M. Godinho, *Physical Review B*, 2003, **68**.
- ⁹ J. L. Dormann, J. R. Cui, and C. Sella, *Journal of Applied Physics*, 1985, **57**, 4283.
- ¹⁰ Christia.J, H. E. Mahnke, U. Morfeld, Recknage.E, D. Riegel, and W. Witthuhn, *Zeitschrift Fur Physik*, 1973, **261**, 13.
- ¹¹ C. G. Shull, W. A. Strauser, and E. O. Wollan, *Phys. Rev.*, 1951, **83**, 333.
- ¹² F. Morin, *J. Phys. Rev.*, 1950, **78**, 819.
- ¹³ L. Neel and R. Pauthenet, *Compt. Rend.*, 1952, **234**, 2172.
- ¹⁴ R. Nathans, S. J. Pickart, H. A. Alperin, and P. J. Brown, *Phys. Rev.*, 1964, **136**, A1641.
- ¹⁵ S. Foner and S. J. Williamson, *J. Appl. Phys.*, 1965, **36**, 1154.
- ¹⁶ S. H. Gee, Y. K. Hong, J. C. Sur, D. W. Erickson, M. H. Park, and F. Jeffers, *Ieee Transactions on Magnetics*, 2004, **40**, 2691.
- ¹⁷ F. Bodker, M. F. Hansen, C. B. Koch, K. Lefmann, and S. Morup, *Physical Review B*, 2000, **61**, 6826.
- ¹⁸ N. Amin and S. Arajs, *Physical Review B*, 1987, **35**, 4810.

- ¹⁹ W. Kundig, H. Bommel, G. Constabaris, and R. H. Lindquist, *Phys. Rev.*, 1966, **142**, 327.
- ²⁰ G. Shirane, D. E. Cox, W. J. Takei, and S. L. Ruby, *J. Phys. Soc. Jpn.*, 1962, **17**, 1598.
- ²¹ R. L. Black, R. E. Hessevick, T. Zoltai, and L. W. Finger, *Am. Mineral.*, 1966, **51**, 123.

4-2 Nanowire and mesoporous Co₃O₄ with crystalline walls: synthesis and structural characterization

In order to achieve a high capacity to store charge within rechargeable lithium batteries, it is becoming increasingly important to go beyond intercalation as a basis for the electrode reactions.¹⁻³ The discovery of reversible conversion reactions with a capacity above 800 mAh/g makes it a promising route to achieve higher storage capacities.^{1, 3} Early work focused on the investigation of such conversion reactions with micron sized particles. However, it is vital to increase the charge/discharge rate, as well as the capacity, if lithium batteries are to meet the needs of the myriad of new applications, including hybrid vehicles and power tools. In an attempt to improve the rate of conversion reactions, and hence the rate of charge/discharge, nanoparticulate materials were investigated but found to exhibit considerable fade in their charge storage capacity on cycling.³⁻⁵ Co₃O₄, at least on initial discharge, exhibits the highest capacity on cycling, which makes it very interesting as an anode material. Here, the preparations of nanowire and mesoporous Co₃O₄ are described.

4-2-1 Experimental section

Preparations of the mesoporous silicas, SBA-15 and KIT-6, have been described previously in Chapter 2-1. A typical synthesis of mesoporous and nanowire Co₃O₄ were as following: 1 g of Co(NO₃)₂·6H₂O (98%, Aldrich) was dissolved in 20 mL of ethanol, followed by addition of 2 g of mesoporous silica (SBA-15 for nanowire and KIT-6 for mesopore, respectively). After stirring at room temperature until all solution had been absorbed, the sample was heated slowly to 300 °C and calcined at that temperature for 3 h. The impregnation procedure was repeated, followed by calcined at 500 °C for 3 h. The resulting sample was twice treated with a 10% HF solution in water to remove the silica template, followed by washing with water and ethanol several times, and then drying at 60 °C.

4-2-2 Results and discussion

The nanowire structure of Co₃O₄ arising from SBA-15 is shown in Figure 1. These nanowires are connected by small bridges (indicated by the arrow in Figure 1d), which originates from the microporosity in the SBA-15 template. The bridges serve not only to organize the wires into parallel bundles with a hexagonal symmetry (Figure 1c), but also to provide single crystal atomic order between the wires. By examining the HRTEM image (Figure 1d), it is clear that the lattice fringes are in the same direction for all wires, confirming the single-crystal like nature of the particle. The diameter and length of the

nanowires are 9.5 nm and up to several hundred nanometres respectively, based on TEM analysis.

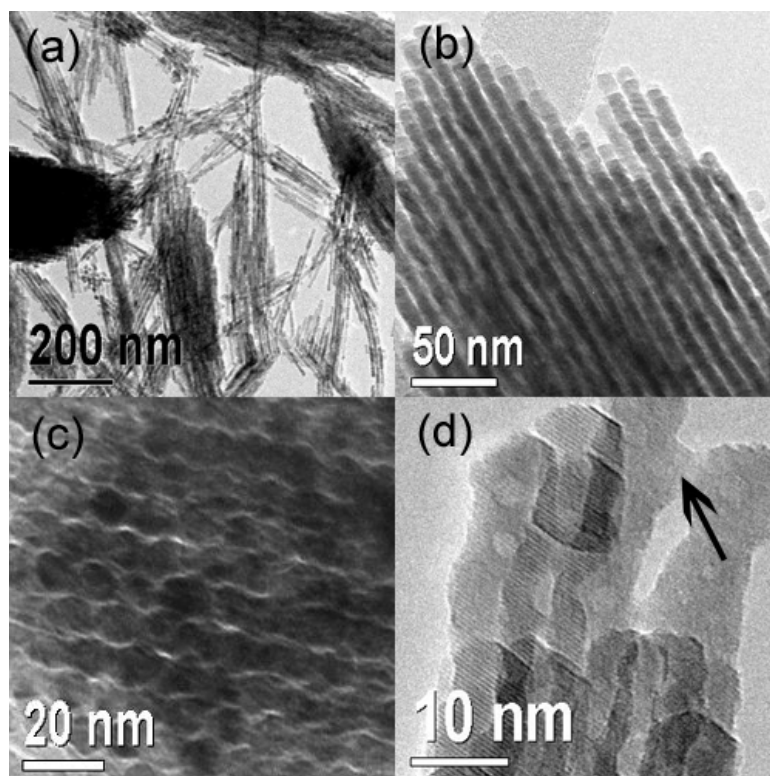


Figure 1. TEM images of Co_3O_4 nanowires: (a) at low magnification, (b) perpendicular and (c) parallel to the wire axis. (d) HRTEM images of Co_3O_4 nanowires.

TEM images for mesoporous Co_3O_4 prepared using KIT-6 as the hard template are shown in Figure 2. A highly ordered mesoporous structure is evident. By examining many particles, it can be confirmed that the mesoporosity is present in most of the particles.

TEM images recorded along different directions show that Co_3O_4 formed from KIT-6 has a cubic mesostructure with a space group of Ia-3d, replicating the pore structure of the template. Mesoporous Co_3O_4 , with Ia-3d symmetry, was prepared for the first time very recently. It was found necessary to functionalise the pores by attaching vinyl groups, thus providing superior coordination of Co ions and hence high loadings.⁶ However, as demonstrated here, this is not essential. The wall thickness of mesoporous Co_3O_4 is around 8 nm estimated by HRTEM analysis (Figure 2d), which is similar to the pore size of the template (7.6 nm) determined by nitrogen adsorption-desorption measurement. Based on the HRTEM analysis (Figure 2d), the lattice fringes all run in the same direction in the walls, indicating the single-crystal like nature of each particle, which is similar to the nanowires prepared by using SBA-15 as template.

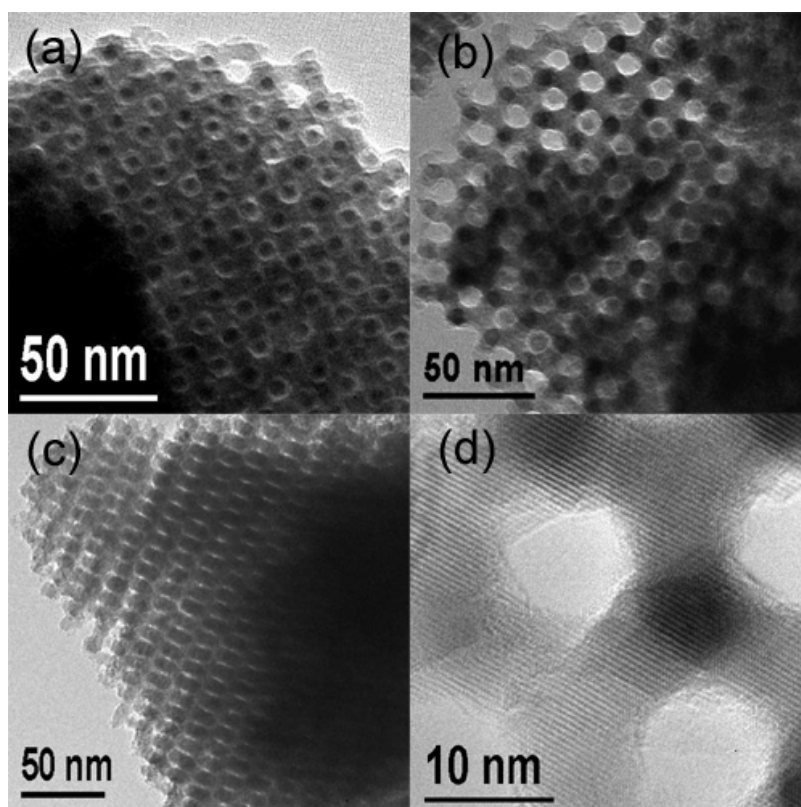


Figure 2. TEM images for mesoporous Co_3O_4 recorded along (a) [100], (b) [111], and (c) [311] directions. HRTEM images for mesoporous Co_3O_4 .

The wall structure for both nanowire and mesopore materials are confirmed by wide-angle powder X-ray diffraction (PXRD) analysis (Figure 3). The diffraction peaks corresponded well to that of Co_3O_4 spinel (JCPDS Number: 9-418), were clearly for nanowire and mesoporous materials, indicating that the highly crystalline structure of the walls. This is in good agreement with the HRTEM analysis results (Figures 1d and 2d).

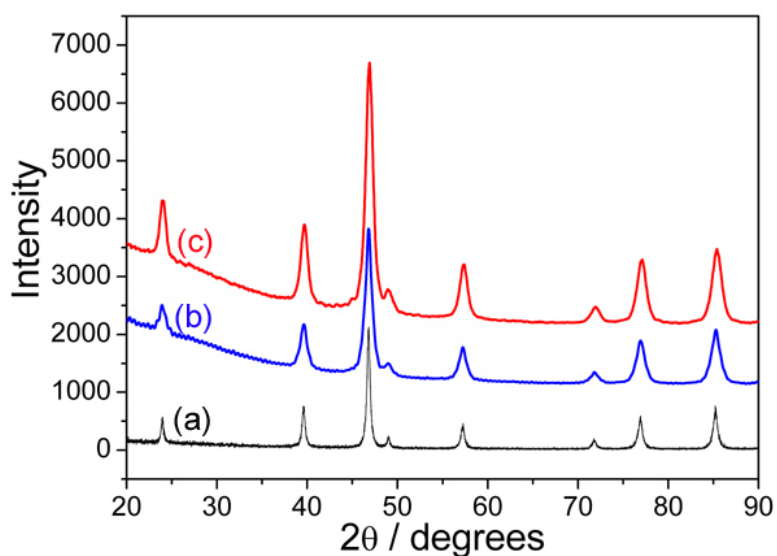


Figure 3. PXRD patterns for (a) bulk, (b) nanowire, and (c) mesoporous Co_3O_4 .

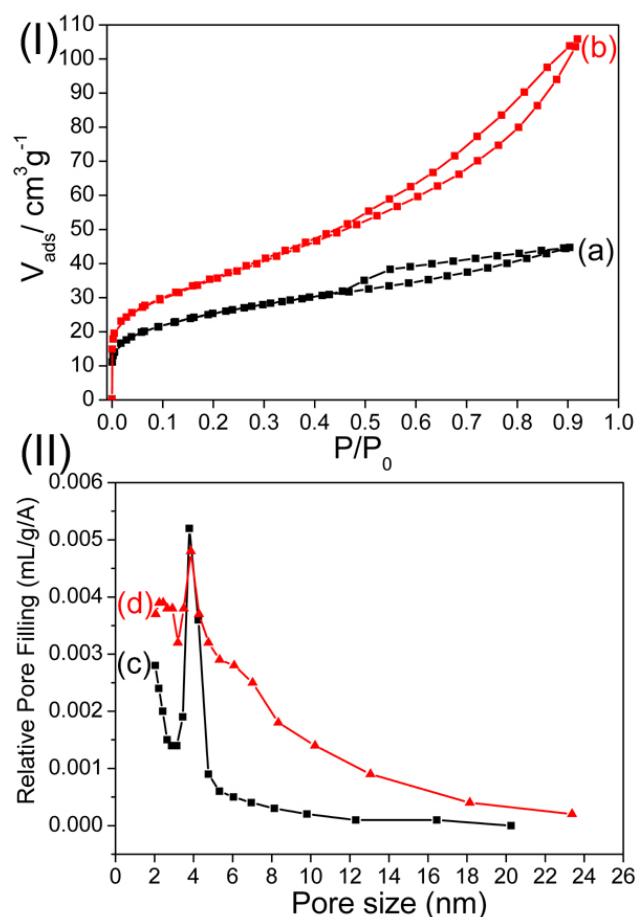


Figure 4. (I) N_2 adsorption-desorption isotherms for (a) nanowire and (b) mesoporous Co_3O_4 ; (II) pore size distributions for (c) nanowire and (d) mesoporous Co_3O_4 .

N_2 adsorption-desorption isotherms (Figure 4a, b) for both forms of nanostructured Co_3O_4 show type IV isotherms with an H_1 hysteresis loop, confirming the mesoporosity. The specific surface areas of nanowire and mesoporous Co_3O_4 estimated from the Brunauer-Emmett-Teller (BET) method are $90.4 \text{ m}^2 \text{g}^{-1}$ and $130.5 \text{ m}^2 \text{g}^{-1}$, respectively. The pore size distribution for nanowire Co_3O_4 is shown in Figure 4(II)c. A slightly broad pore size distribution with a peak position of 3.77 nm was observed, indicating that the links between those wires is weak resulting in the slightly distortion in the nanostructure and a wide pore size distribution. The diameter (9.5 nm) and pore size (3.77 nm) of Co_3O_4 nanowires are consistent with the pore size (9.5 nm) and wall thickness (3.5 nm) for the mesoporous silica SBA-15 template, calculated from TEM, low-angle PXRD, and N_2 adsorption analysis. Turning to the pore size distribution [Figure 4(II)d] for mesoporous Co_3O_4 , a narrow distribution with a sharp peak centred at 3.85 nm was observed. The narrow pore size distribution indicated that this material has a highly ordered mesoporous structure.

4-2-3 Conclusions

Ordered nanowire and mesoporous Co_3O_4 with crystalline walls have been prepared for the first time using SBA-15 and KIT-6 as the hard template respectively. Both materials exhibit highly ordered mesostructure and crystalline walls with a high surface area ($>100 \text{ m}^2\text{g}^{-1}$) and an average pore size of $\sim 4 \text{ nm}$.

4-2-4 References

- ¹ P. Poizot, S. Laruelle, S. Grugeon, L. Dupont, and J. M. Tarascon, *Nature*, 2000, **407**, 496.
- ² Y. Idota, T. Kubota, A. Matsufuji, Y. Maekawa, and T. Miyasaka, *Science*, 1997, **276**, 1395.
- ³ D. Larcher, G. Sudant, J. B. Leriche, Y. Chabre, and J. M. Tarascon, *Journal of the Electrochemical Society*, 2002, **149**, A234.
- ⁴ S. Grugeon, S. Laruelle, L. Dupont, and J. M. Tarascon, *Solid State Sciences*, 2003, **5**, 895.
- ⁵ V. Pralong, J. B. Leriche, B. Beaudoin, E. Naudin, M. Morcrette, and J. M. Tarascon, *Solid State Ionics*, 2004, **166**, 295.
- ⁶ Y. Q. Wang, C. M. Yang, W. Schmidt, B. Spliethoff, E. Bill, and F. Schuth, *Advanced Materials*, 2005, **17**, 53.

4-3 Mesoporous β -MnO₂ with crystalline walls: synthesis and structural characterization

Nanomaterials have the potential to deliver a step change in the performance of rechargeable lithium batteries.^{1, 2} Such materials could enable the development of a new generation of rechargeable lithium batteries, essential for addressing applications such as hybrid vehicles and clean energy storage, in order to tackle Global Warming.¹⁻³ Mesoporous transition metal oxides as potential candidates have attracted much attention.⁴⁻⁸ Here the first synthesis of mesoporous β -MnO₂ (rutile structure) with a highly ordered pore structure and highly crystalline walls is demonstrated. The material is capable of reversibly accommodating lithium, up to a composition Li_{0.92}MnO₂ (equivalent to charge storage of 284 mAh/g) in sharp contrast to bulk crystalline β -MnO₂, which can accommodate little or no Li on electrochemical discharge. The electrochemical properties are discussed in Chapter 5. Here, the synthesis and structural characterization of mesoporous β -MnO₂ are described.

4-3-1 Experimental section

Preparation of the mesoporous silica KIT-6 has been described previously in Chapter 2-1. A typical synthesis of mesoporous β -MnO₂ was as follows: 30 g of Mn(NO₃)₂·6H₂O (98%, Aldrich) was mixed with 20 mL of water to form a saturated Mn(NO₃)₂ solution. 5 g of mesoporous silica KIT-6 was dispersed in 200 mL of dried n-hexane. After stirring at room temperature for 3 h, 5 mL of saturated Mn(NO₃)₂ solution was added slowly under stirring. The mixture was stirred overnight, filtered and dried at room temperature until a completely dried powder was obtained. The sample was heated slowly to 400 °C and calcined at that temperature for 3 h. The resulting material was treated twice with a hot aqueous solution of 2M NaOH to remove the silica template, followed by washing with water several times, and then drying at 60 °C.

4-3-2 Results and discussion

TEM data for mesoporous β -MnO₂, Figure 1, demonstrate the highly ordered three-dimensional pore structure, replicating that of KIT-6 (space group Ia-3d). Examining many particles confirmed that the ordered pore structure is representative of the entire sample. From the TEM data an a_0 lattice parameter of 24.9 nm for the mesostructure was extracted, in good agreement with the value obtained from the low angle powder x-ray diffraction (PXRD) data, $a_0 = 24.6$ nm (Figure 2).

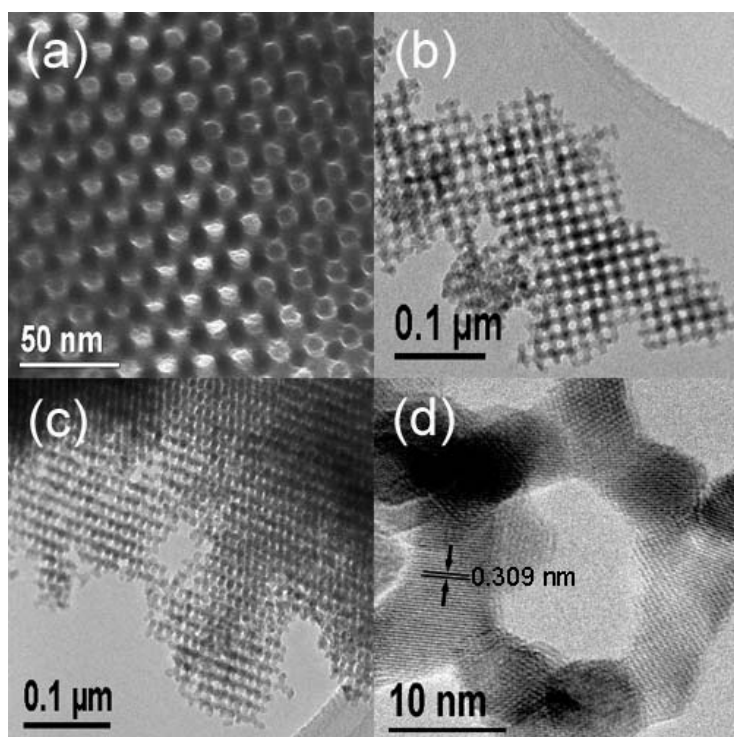


Figure 1. TEM images of mesoporous β -MnO₂ recorded along (a) [111], (b) [100] and (c) [311] directions. (d) HRTEM image of mesoporous β -MnO₂.

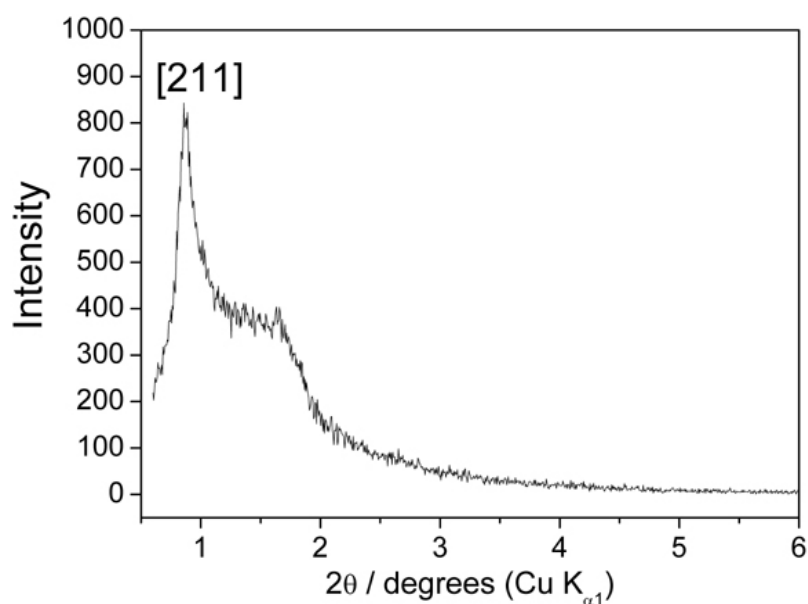


Figure 2. Low-angle PXRD pattern for mesoporous β -MnO₂.

HRTEM images in Figure 1d show that the walls are highly crystalline with a typical wall thickness of 7.5 nm. The lattice spacing of 3.09 Å, Figure 1d, agrees well with the value of 3.11 Å for the [110] planes of β -MnO₂ (JCPDS No. 24-735). The wide angle PXRD data match well with the PXRD data for bulk β -MnO₂, Figure 3, confirming that the walls of the mesoporous material possess the rutile structure. Further characterization of the

mesostructure was carried out by N₂-sorption measurements, Figure 4, which show a type IV isotherm, consistent with mesoporosity. The pore size distribution, calculated from the desorption branch of the isotherm, is narrow and centred around a diameter of 3.65 nm. The BET surface area is 127 m²g⁻¹. Confirmation of the composition and oxidation state of manganese (4+) was obtained by atomic absorption and redox titration.⁹

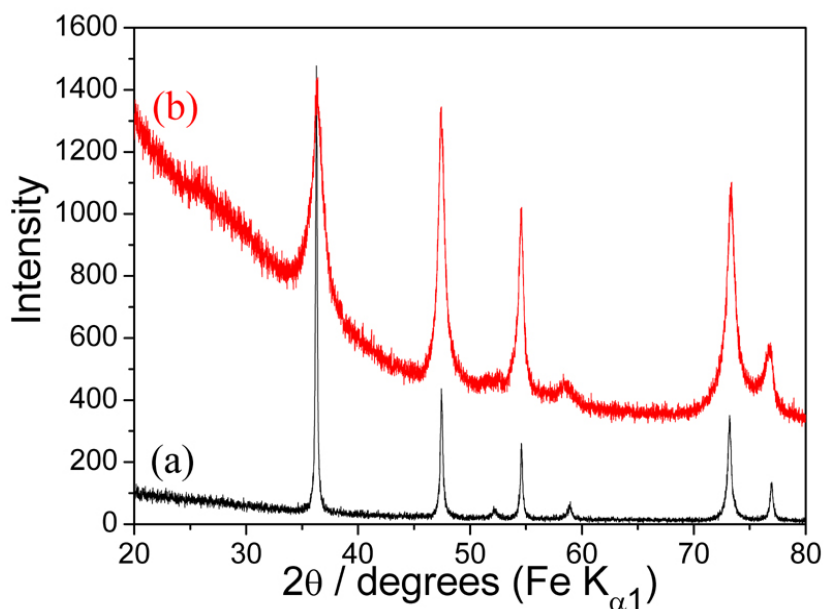


Figure 3. Wide angle PXRD patterns for (a) bulk and (b) mesoporous β -MnO₂.

Further confirmation that mesoporous compound with the composition β -MnO₂ has been prepared was obtained from EXAFS. The Fourier transformed EXAFS data are presented in Figure 4 along with data for the bulk phase (raw data deposited). The data for the mesoporous and corresponding bulk materials are identical, confirming the results from the powder X-ray diffraction measurements.

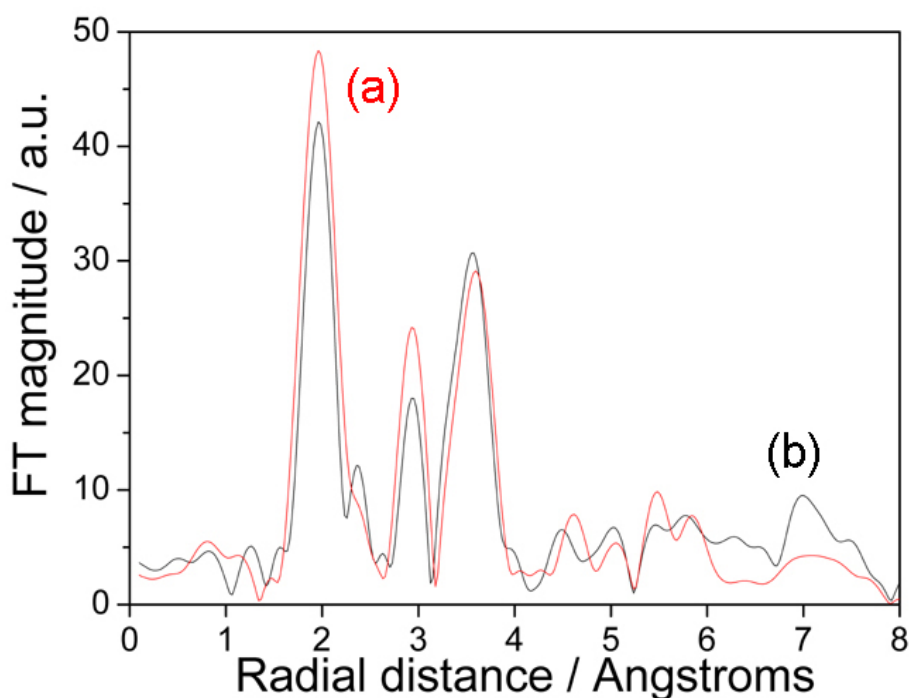


Figure 4. EXAFS results for (a) mesoporous β -MnO₂ (red line) and (b) bulk β -MnO₂ (black line).

4-3-3 Conclusions

Mesoporous β -MnO₂ with highly crystalline walls has been prepared by using mesoporous silica KIT-6 as a hard template. TEM, low-angle PXRD and N₂ adsorption measurements confirm that this material has a highly ordered three dimensional pore structure. HRTEM, wide-angle PXRD, and EXAFS analysis confirm the walls of mesoporous β -MnO₂ are highly crystalline.

4-3-4 References

- ¹ A. S. Arico, P. Bruce, B. Scrosati, J. M. Tarascon, and W. Van Schalkwijk, *Nature Materials*, 2005, **4**, 366.
- ² L. Taberna, S. Mitra, P. Poizot, P. Simon, and J. M. Tarascon, *Nature Materials*, 2006, **5**, 567.
- ³ J. M. Tarascon and M. Armand, *Nature*, 2001, **414**, 359.
- ⁴ D. M. Antonelli and J. Y. Ying, *Current Opinion in Colloid & Interface Science*, 1996, **1**, 523.
- ⁵ U. Ciesla and F. Schuth, *Microporous and Mesoporous Materials*, 1999, **27**, 131.

- ⁶ D. E. De Vos, M. Dams, B. F. Sels, and P. A. Jacobs, *Chemical Reviews*, 2002, **102**, 3615.
- ⁷ B. Z. Tian, X. Y. Liu, L. A. Solovyov, Z. Liu, H. F. Yang, Z. D. Zhang, S. H. Xie, F. Q. Zhang, B. Tu, C. Z. Yu, O. Terasaki, and D. Y. Zhao, *Journal of the American Chemical Society*, 2004, **126**, 865.
- ⁸ P. D. Yang, D. Y. Zhao, D. I. Margolese, B. F. Chmelka, and G. D. Stucky, *Nature*, 1998, **396**, 152.
- ⁹ M. J. Katz, R. C. Clarke, and W. F. Nye, *Anal. Chem.*, 1956, **28**, 507.

4-4 Mesoporous Mn₂O₃ with crystalline walls: synthesis and structural characterization

Manganese oxides have attracted much attention because they are cheap, non-toxic and important in various applications, such as catalysis, energy storage and conversion, and magnetic devices.¹⁻³ In a previous section (Chapter 4-3), the synthesis of mesoporous β -MnO₂ with highly crystalline walls and an ordered pore structure was described. By modifying the synthesis conditions, this method could also be used to prepare mesoporous Mn₂O₃. The following paragraphs discuss the synthesis and structural characterization of mesoporous Mn₂O₃.

4-4-1 Experimental section

Preparation of mesoporous Mn₂O₃ was modified from the method for the synthesis of mesoporous β -MnO₂. In a typical synthesis of mesoporous Mn₂O₃, 30 g of Mn(NO₃)₂·6H₂O (98%, Aldrich) was dissolved in ~ 20 mL of water to form a saturated Mn(NO₃)₂ solution. 5 g of mesoporous KIT-6 were dispersed in 200 mL of dried n-hexane. After stirring at room temperature for 3 h, 5 mL of the saturated Mn(NO₃)₂ solution was added slowly with stirring. The mixture was stirred overnight, filtered and dried at room temperature until a completely dried powder was obtained. The sample was heated slowly to 600 °C, calcined at that temperature for 3 h and the resulting material treated twice with a hot aqueous solution of 2M NaOH, to remove the silica template, followed by washing with water several times, and then drying at 60 °C.

4-4-2 Results and discussion

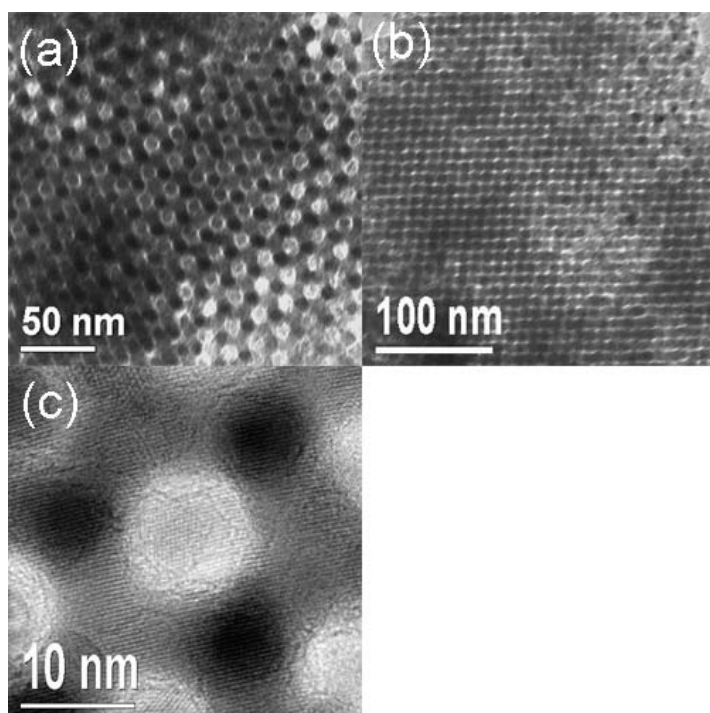


Figure 1. TEM images for mesoporous Mn₂O₃ recorded along (a) [111] and (b) [110] directions, (c) HRTEM image for mesoporous Mn₂O₃.

A highly ordered mesoporous structure with an Ia-3d symmetry is evident in the TEM images (Figure 1a and b), confirming that mesoporous Mn₂O₃ fully replicates the mesostructure of the KIT-6 template. By examining many particles in different regions, the ordered mesoporous structure is present throughout the whole sample. The unit cell parameter, a_0 , extracted from the TEM data for mesoporous Mn₂O₃, is 25.1 nm, which is similar to the value for mesoporous β -MnO₂ (24.6 nm) prepared using the same KIT-6 hard template and ‘bi-solvent’ method.

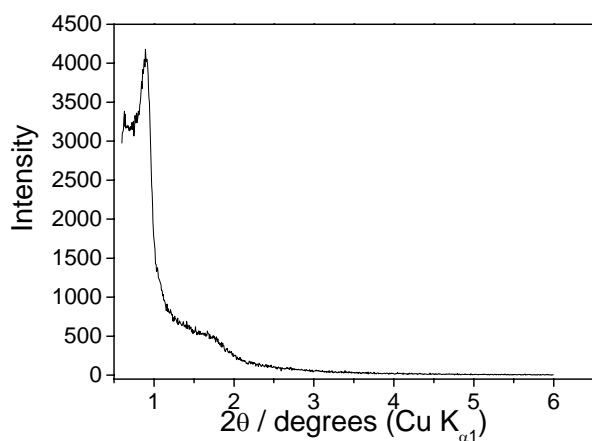


Figure 2. Low angle PXRD patterns for mesoporous Mn₂O₃.

The mesostructure of Mn_2O_3 was also confirmed by low-angle powder X-ray diffraction (PXRD), Figure 2, which exhibits one sharp peak at $\sim 0.9^\circ$, that could be indexed as the [211] reflection in Ia-3d symmetry, and one broad peak at $1.7\text{-}1.8^\circ$, which indicates the high degree of ordering between the pores. The d -value calculated from the first peak is 101.2 \AA , which corresponds to a unit cell parameter, a_0 , 24.8 nm , in good agreement with the TEM results.

The surface area and pore size of mesoporous Mn_2O_3 were examined by nitrogen adsorption-desorption measurements. Type IV isotherms were observed for mesoporous Mn_2O_3 , which indicates the mesoporosity (Figure 3a). The Brunauer- Emmett-Teller (BET) surface area is $138.7 \text{ m}^2\text{g}^{-1}$. The pore size distribution calculated from the desorption isotherm is shown in Figure 3b, exhibits a narrow distribution centred at 3.51 nm . This value is similar to those values for other mesoporous materials, such as $\alpha\text{-Fe}_2\text{O}_3$, Co_3O_4 , and $\beta\text{-MnO}_2$, prepared using KIT-6 as the hard template.

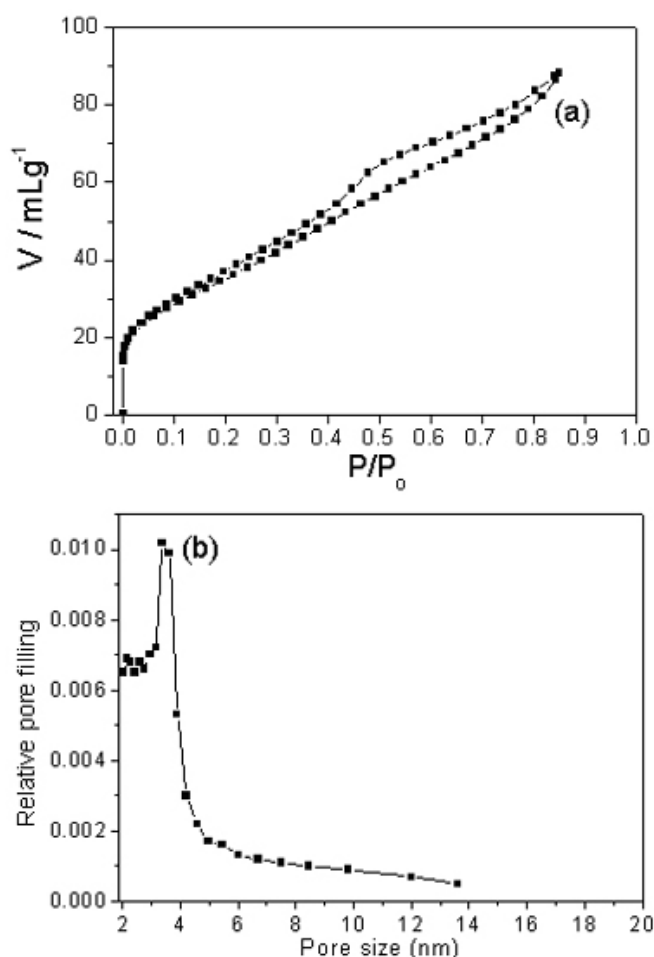


Figure 3. (a) N_2 adsorption-desorption isotherms for mesoporous Mn_2O_3 and (b) the pore size distribution calculated from the desorption isotherm.

The wall structure was first examined by high-resolution TEM (HRTEM) analysis. A typical HRTEM image (Figure 1c) shows clear lattice fringes, indicating the walls of mesoporous Mn_2O_3 are highly crystallized. Wide-angle PXRD patterns for mesoporous and bulk Mn_2O_3 (Figure 4) exhibit several well-defined peaks at the same positions, which correspond to the diffraction pattern for Mn_2O_3 (JCPDS Nos. 24-508). These results confirm that the material has highly crystalline walls with the Mn_2O_3 structure.

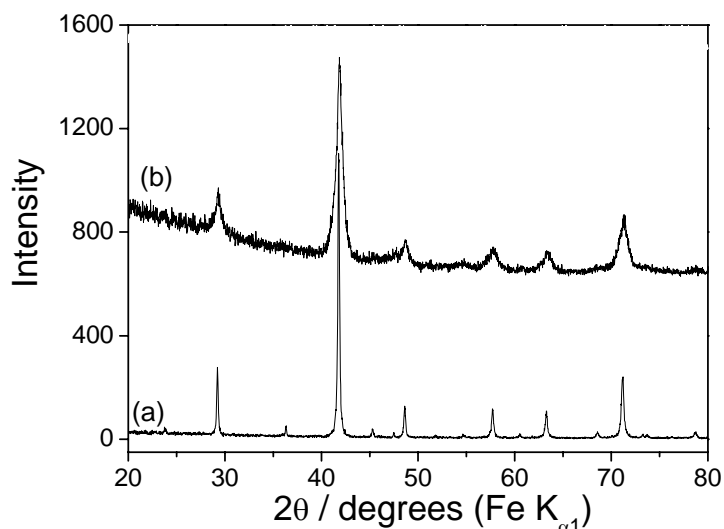


Figure 4. Wide-angle PXRD patterns for (a) bulk Mn_2O_3 , and (b) mesoporous Mn_2O_3 .

4-4-3 Conclusions

Mesoporous Mn_2O_3 with highly crystalline walls has been successfully synthesized for the first time. The ordered mesostructure is demonstrated by TEM, N_2 adsorption-desorption, and low-angle PXRD measurements. The crystal nature of the walls was examined by HRTEM and wide-angle PXRD analysis.

4-4-4 References

- ¹ M. M. Thackeray, *Progress in Solid State Chemistry*, 1997, **25**, 1.
- ² Z. R. Tian, W. Tong, J. Y. Wang, N. G. Duan, V. V. Krishnan, and S. L. Suib, *Science*, 1997, **276**, 926.
- ³ Y. Moritomo, A. Asamitsu, H. Kuwahara, and Y. Tokura, *Nature*, 1996, **380**, 141.

Chapter 5 Electrochemical properties of nanowire and mesoporous transition metal oxides with crystalline walls

5-1 Electrochemical properties of nanowire and mesoporous Co₃O₄

Co₃O₄, a potential candidate as a negative electrode in lithium-ion batteries, shows a high capacity compared with commercialized graphite electrode materials.¹⁻³ In previous section (Chapter 4-2), the synthesis and structural characterization of nanowire and mesoporous Co₃O₄ have been discussed. Here, the electrochemical properties of nanowire and mesoporous Co₃O₄ are investigated.

5-1-1 Experimental section

Electrochemical cells were constructed by mixing the active material, Kynar (a co-polymer based on polyvinylidene fluoride), and Super S carbon in the weight ratios 70:15:15. The mixture was cast onto Cu foil from THF using a Doctor-Blade technique. After solvent evaporation at room temperature and heated at 80 degrees under vacuum for 8 hours, the electrodes were assembled into cells with a Li electrode and LP 30 electrolyte (Merck; 1M LiPF₆ in 1:1 v/v EC:DMC). The cells were constructed and handled in an Ar-filled MBraun glovebox. Electrochemical measurements were carried out using a Biologic MacPile II system.

Nanoparticulate Co₃O₄ examined in this study was synthesized using the method reported previously by Tarascon and co-workers.² Micron-sized Co₃O₄ used here is from Aldrich (Product No. 221643, < 10 μm). The surface areas of the nanoparticulate and microparticulate Co₃O₄ materials determined by BET method are 45 and 1 m²/g⁻¹, respectively.

5-1-2 Results and discussion

Composite electrodes were prepared as described and incorporated into lithium cells. The charge-discharge curves for the four anodes, mesoporous, nanowire, nanoparticulate, and microparticulate (bulk) Co₃O₄ on the first cycle are shown in Figure 1. The curves from nano- and micro-particulate Co₃O₄ are very similar to those reported previously.¹⁻⁴ The early stages of discharge for the nanoparticulate material exhibits a plateau at approximately 1.25 V versus Li⁺/Li that extends up to approximately 150

mAh/g, i.e. to a lithium content of 1.5 per Co_3O_4 . This plateau has been interpreted previously as arising from formation of $\alpha\text{-CoO}$. In contrast, microparticulate Co_3O_4 exhibits a plateau at 1.1 V, the voltage later rising to 1.2 V. the lower voltage plateau has been interpreted previously as arising from lithium intercalation into the cobalt oxide spinel to form, $\text{Li}_x\text{Co}_3\text{O}_4$.^{2, 5} Mesoporous and nanowire Co_3O_4 show features in their discharge curves more reminiscent of nanoparticulate Co_3O_4 than the microparticulate form of the spinel. However, PXRD data collected at the early stage of discharge (< 150 mAh/g) for these materials show no evidence of $\alpha\text{-CoO}$, only $\text{Li}_x\text{Co}_3\text{O}_4$, Figure 2.

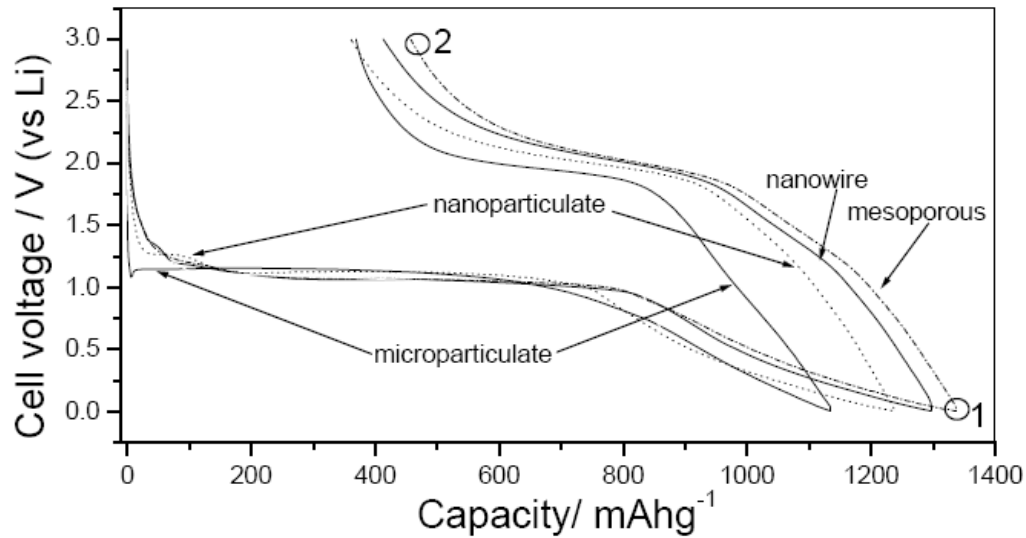


Figure 1. The first cycle charge-discharge curves for mesoporous, nanowire, nanoparticulate, and microparticulate Co_3O_4 at 100 mA/g in the voltage range 0.005-3.00 V. the circles 1 and 2 in the voltage profile for mesoporous Co_3O_4 represent the points at which the TEM/SAED were performed.

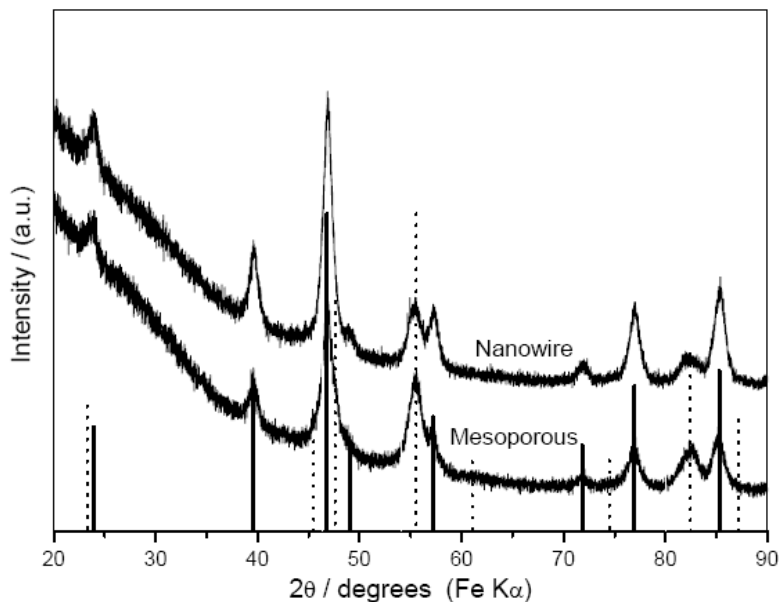


Figure 2. PXRD patterns for mesoporous and nanowire Co_3O_4 after discharging to a capacity corresponding to 1 Li per Co_3O_4 formula unit at 10 mA/g. The relative intensities and peak positions of Co_3O_4 (solid lines) and $\text{Li}_x\text{Co}_3\text{O}_4$ (dotted lines) from the JCPDS file are also shown for comparison.

Considering the discharge curves in Figure 1, beyond ~ 170 mAh/g, all four forms of Co_3O_4 exhibit a long plateau associated with the conversion reaction $\text{Co}_3\text{O}_4 + 8\text{Li}^+ + 8\text{e}^- \rightarrow 4\text{Li}_2\text{O} + 3\text{Co}$.²⁻⁴ Thereafter, the voltage falls gradually to the cut-off potential of 5.0 mV, this region being associated with the formation of a polymeric layer on the surface of the electrode particles or with the storage of charge/mass at the interface between the Li_2O and Co nanoparticles within the nanocomposite.^{2, 3, 6, 7} Confirmation that the nanostructured materials undergo the same conversion reaction as has previously been observed for the micron-sized particles was obtained by TEM and selected area electron diffraction. Such data, collected at the states of charge and discharge shown in Figure 1, for mesoporous Co_3O_4 are shown in Figure 3. At the end of discharge the electron diffraction data show that Co_3O_4 has completely disappeared and been replaced by Li_2O and Co. On charging, the rings associated with Li_2O and Co disappear and are replaced by those corresponding to CoO. Formation of CoO on charging rather than the spinel Co_3O_4 is well known.^{1, 2, 4}

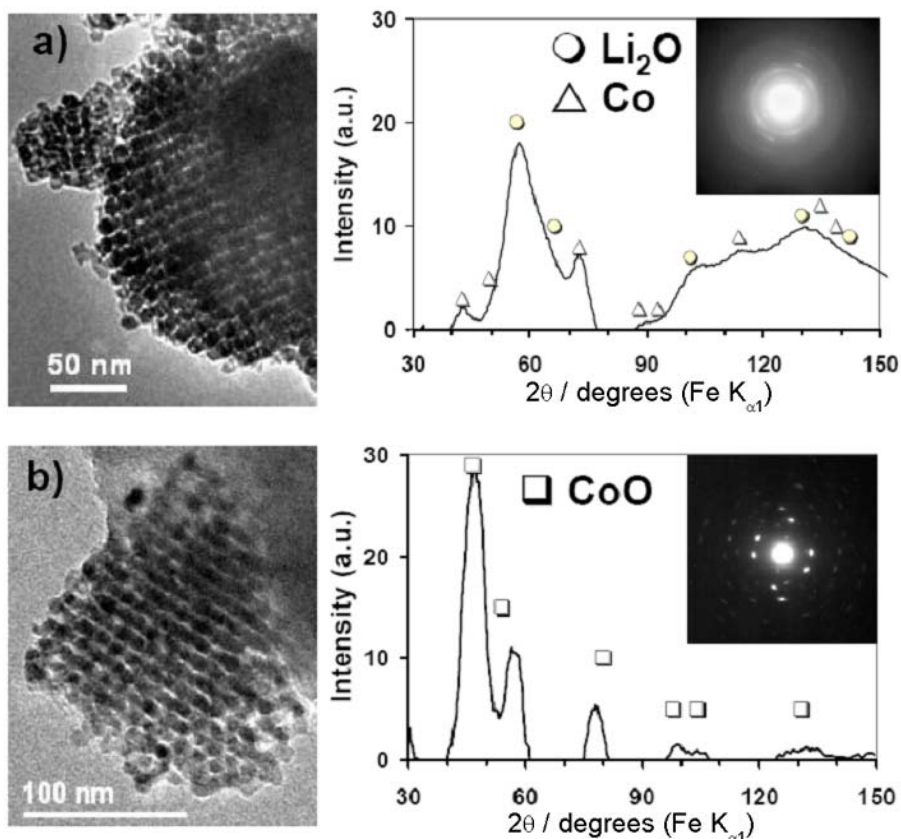


Figure 3. TEM and SAED data for mesoporous Co_3O_4 collected (a) after first discharge to 0.005 V and (b) recharged to 3.00 V. The positions of the diffraction rings and their assignments are also shown.

Considering further the charge/discharge curves in Figure 1, it is clear the capacity associated with the long plateau (conversion reaction) extends further for the nanoparticles and further still for the mesoporous and nanowire materials than for the microparticles. In all cases the observed capacity associated with the conversion reaction is less than the theoretical value of 890 mAh/g. Interestingly, despite an increase in the surface area by 45, 90 and 130 times on going from the micron particles to the nanoparticles, nanowires, and mesoporous material respectively, the capacities associated with the surface layer formation/space charge (sloping region of the discharge curves) do not increase by the same factors. This indicates that the total surface area is not the limiting factor for the polymer layer growth. We suggest that the Co_3O_4 surface area is not completely covered on the first discharge or the growth within the pores or between

the wires is limited to some extent, perhaps because of slower mass transport of the constituents that go to make up the polymer layer.

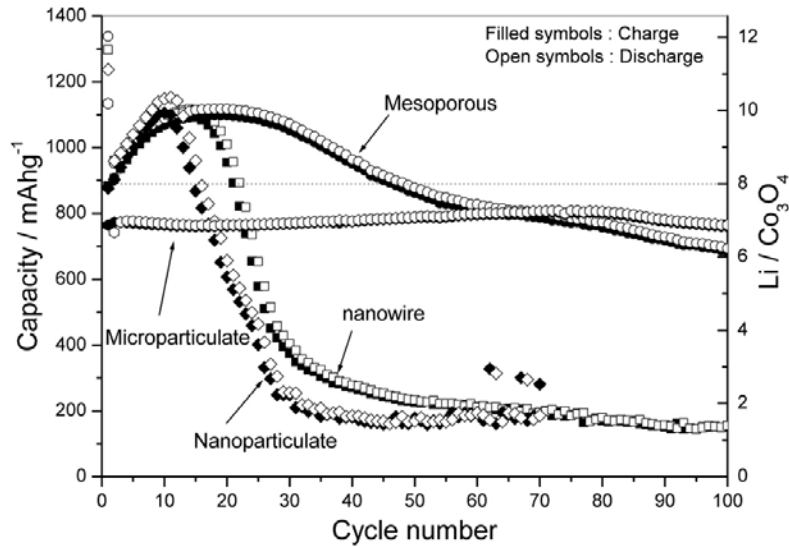


Figure 4. Charge and discharge capacities as a function of cycle numbers for mesoporous, nanowire, nanoparticulate, and microparticulate Co_3O_4 measured in the voltage range, 0.005-3.00 V at a rate of 100 mA/g.

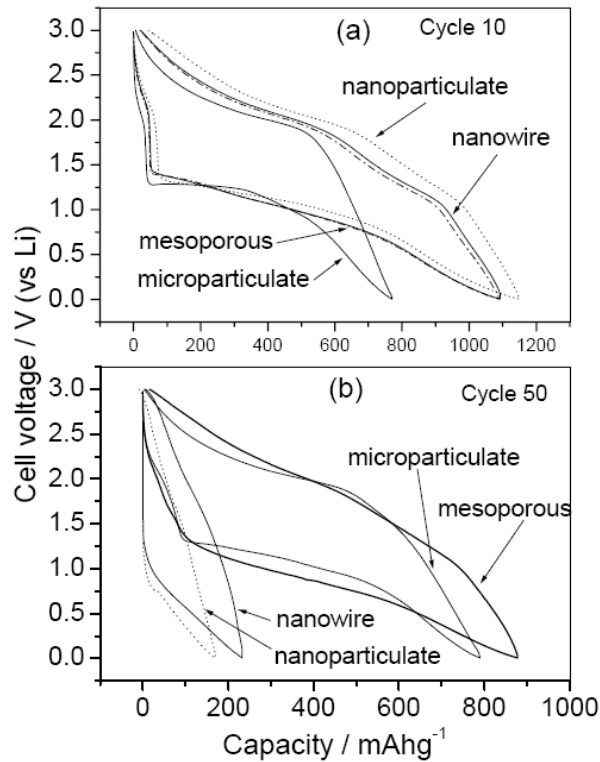


Figure 5. Charge-discharge voltage profiles for mesoporous, nanowire, nanoparticulate, and microparticulate Co_3O_4 at 100 mA/g in the voltage range, 0.005-3.00 V: (a) for the 10th cycle and (b) for the 50th cycle.

The variation of charge and discharge capacity with cycle number is shown in Figure 4, along with the theoretical capacity for the conversion reaction. The data for microparticulate Co_3O_4 are similar to previous observations.^{2, 3} The behaviour of the nanowires and nanoparticles is, however, significantly different from the mesoporous material. All three nanomaterials show a marked increase in capacity on initial cycling, up to 10-15 cycles. The capacities exceed the theoretical value for the conversion reaction, indicating that the excess capacity is associated with increased charge storage within the polymeric surface layer. We propose that the higher surface areas of the nanomaterials, permits, on cycling, an increase in the extent of polymer layer formation per unit mass of electrode material. Unfortunately, despite a relatively clear distinction between the regions associated with the conversion reaction (plateau) and surface layer formation (sloping voltage) on the first discharge, this is not the case on subsequent cycling, with the plateau and low voltage sloping regions overlapping too much for a satisfactory separation of their capacities into the two contribution, Figure 5a. Even differential capacity plots do not resolve these processes satisfactorily. Therefore, we cannot associate directly the increase of the overall capacity with the component of that capacity due to the polymer layer. However, the gradual increase of this excess capacity over the first 10-15 cycles is consistent with the proposal, discussed above, that not all the surface layer is covered on the first discharge or the internal surface within the pores or between the wires which are more difficult to access. It would appear that the polymer layer builds-up slowly, over a number of cycles.

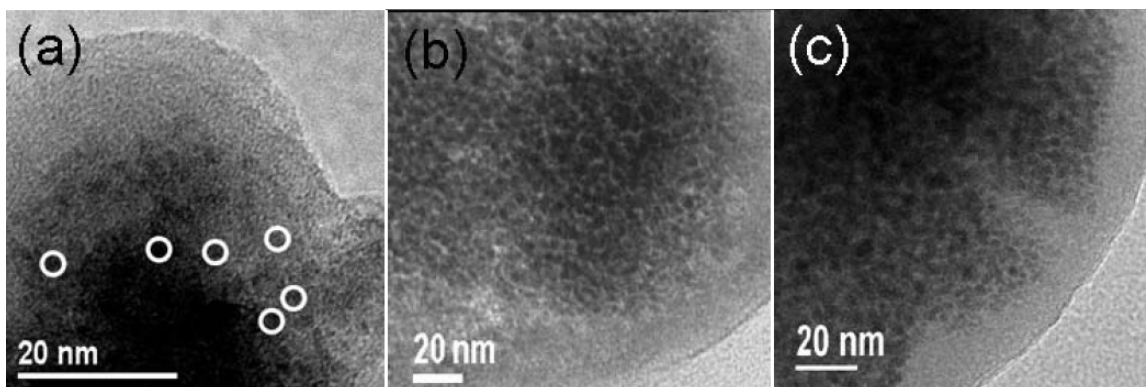


Figure 6. TEM images for (a) nanowire, (b) mesoporous, and (c) micronanoparticulate Co_3O_4 after 50 cycles. Nanoparticles are highlighted by circles in (a).

Although all three nanomaterials exhibit anomalously high capacities, which increase on cycling, this only occurs up to ~ 15 cycles. Thereafter, the capacities decrease, but to different degrees. The nanoparticulate material and the nanowires behave somewhat similarly, but the behaviour of the mesoporous material is markedly different. Considering first the nanowires, their capacity drops rapidly after 15 cycles and to values that are much lower than the micron-sized particles, suggesting a drastic loss in the electrochemical activity for the nanowires. Examining the TEM data for the nanowires after fifty cycles, Figure 6a, reveals that the nanowire morphology has disappeared and the material is composed of nanoparticles that appear to be, in many cases, isolated one from another. Taking the TEM evidence, along with rise then severe fall in capacity on cycling together, we suggest that the nanowires convert to grains surrounded by a polymer layer that initially increases the capacity but later leads to severe electrical isolation. Turning to the mesoporous material, the TEM data for the mesoporous material after fifty cycles demonstrate that the mesoporous structure has disappeared, to be replaced by a nano-composite structure which is very similar to that observed for micron-sized particles of Co_3O_4 on cycling, Figure 6. The nanostructure of the cycled nanowire and mesoporous Co_3O_4 are different, Figure 6, the former more dispersed particles than the latter, which is more dense. The similarity between the nano-structures of the mesoporous and micron-sized particles after cycling is in accord with the coalescence of the capacities for the two materials after 50 cycles, Figure 4.

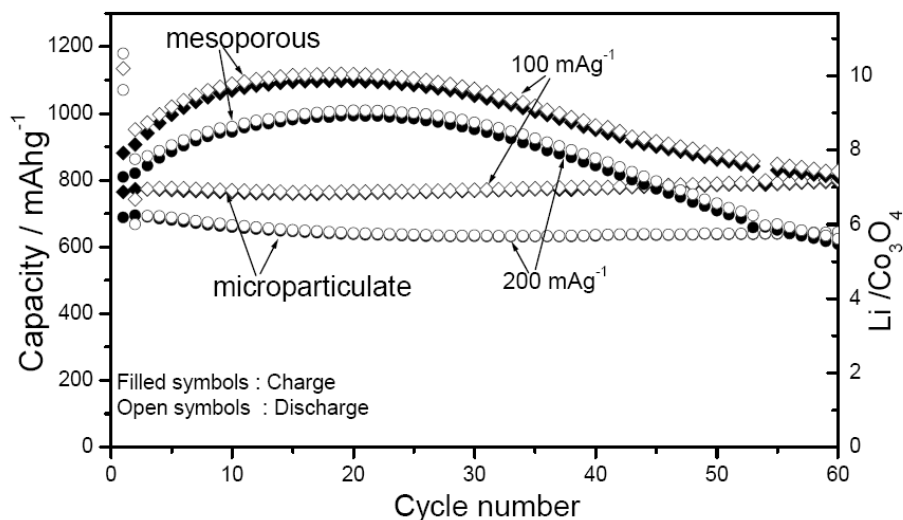


Figure 7. Cycleabilities for mesoporous and microparticulate Co_3O_4 at different rates.

One of the advantages of nanostructured materials is their potential to deliver superior rate capability, i.e. fast charge/discharge. Since the main advantage of employing conversion reactions is their superior capacity compared with intercalation electrodes, it is necessary to investigate the rate capability of such conversion reactions over a wide composition (voltage) range. This includes at least three different processes, formation of $\text{Li}_x\text{Co}_3\text{O}_4$, the conversion reaction itself and surface film formation. Not only can the rate be different for each process, but it may also vary with cycle number, especially given the changes in morphology on cycling, noted above. The rate capability of nanowire and nanoparticulate Co_3O_4 was not measured because of their poor capacity retention on cycling, Figure 4. The rate capability for mesoporous and microparticulate Co_3O_4 is presented in Figure 7. There is no significant difference in the rate performance of the two materials.

5-1-3 Conclusions

The electrochemical reactions of lithium with mesoporous and nanowire Co_3O_4 have been investigated and compared with micron- and nano-particulate forms of the same compound. The nanostructured materials undergo the same conversion reaction and polymer film formation as observed for other forms of Co_3O_4 . The nanostructured materials exhibit a capacity that exceeds the theoretical value for the conversion reaction

and that increases for the first 10-15 cycles. This has been attributed to the increasing formation of a polymer surface layer on these high surface area materials, which contributes to charge storage. At higher cycle numbers, the capacities decrease. In the case of the nanowires the decrease is severe and is interpreted in terms of the formation of grains isolated one from another, probably by a thick polymer layer. For the mesoporous material the morphology and the capacity become very similar to that for the micron-sized particles after 20-30 cycles. Finally, the rate capability of the mesoporous and microparticulate materials are similar, which indicates that the rate capability of Co_3O_4 cannot be improved significantly by reducing the diffusion path of Li ions from micron scale to a nanometre scale.

5-1-4 References

- ¹ S. Grugeon, S. Laruelle, L. Dupont, and J. M. Tarascon, *Solid State Sciences*, 2003, **5**, 895.
- ² D. Larcher, G. Sudant, J. B. Leriche, Y. Chabre, and J. M. Tarascon, *Journal of the Electrochemical Society*, 2002, **149**, A234.
- ³ P. Poizot, S. Laruelle, S. Grugeon, L. Dupont, and J. M. Tarascon, *Nature*, 2000, **407**, 496.
- ⁴ V. Pralong, J. B. Leriche, B. Beaudoin, E. Naudin, M. Morcrette, and J. M. Tarascon, *Solid State Ionics*, 2004, **166**, 295.
- ⁵ M. M. Thackeray, S. D. Baker, K. T. Adendorff, and J. B. Goodenough, *Solid State Ionics*, 1985, **17**, 175.
- ⁶ J. Maier, *Faraday Discussions*, 2007, **134**, 51.
- ⁷ J. Maier, *Nature Materials*, 2005, **4**, 805.

5-2 Electrochemical properties of mesoporous β -MnO₂ with crystalline walls

First generation rechargeable lithium batteries consist of a graphite negative electrode and a LiCoO₂ positive electrode, separated by a non-aqueous liquid electrolyte.¹ Charge and discharge involve the removal of lithium from the LiCoO₂ intercalation host and its reinsertion. The positive electrode is the only source of lithium in the cell.^{2, 3} Lithium metal can store more than ten times the charge compared with graphite (3860 mAh/g versus 360 mAh/g). Recent advances in the cycleability of lithium metal electrodes in non-aqueous electrolytes brings closer the time when the use of such a negative electrode may be possible.^{2, 4} Furthermore, the advent of chemical methods for pre-lithiating the negative electrode, including *in situ*, makes it possible to use a variety of materials, e.g. graphite, Si, Sn, with positive electrodes that are devoid of lithium. Manganese oxides are highly favoured as positive electrodes because of their lower cost, lower toxicity and superior safety compared with those based on V, Co, or Ni, including LiCoO₂.⁵⁻⁹ However, it has proved difficult to prepare Li-Mn-O compounds with a reversible capacity greater than 110 mAh/g. Of the highly crystalline lithium-free manganese dioxides, α -MnO₂ and γ -MnO₂ can sustain reversible lithium intercalation, however the β -polymorph cannot.¹⁰ The behaviour of crystalline mesoporous β -MnO₂ is in sharp contrast to the bulk crystalline β -MnO₂.

5-2-1 Experimental section

Electrochemical cells were constructed by mixing the active material, Kynar (a co-polymer based on polyvinylidene fluoride), and Super S carbon in the weight ratios 70:15:15. The mixture was cast onto Al foil from THF using a Doctor-Blade technique. After solvent evaporation at room temperature and heated at 80 degrees under vacuum for 8 hours, the electrodes were assembled into cells with a Li electrode and LP 30 electrolyte (Merck; 1M LiPF₆ in 1:1 v/v EC:DMC). The cells were constructed and handled in an Ar-filled MBraun glovebox. Electrochemical measurements were carried out using a Biologic MacPile II system.

5-2-2 Results and discussion

The synthesis and structural characterization of mesoporous $\beta\text{-MnO}_2$ were described previously in Chapter 4-3. Mesoporous $\beta\text{-MnO}_2$ was incorporated as the positive electrode in an electrochemical cell composed of a lithium metal counter/reference electrode and a non-aqueous lithium electrolyte (see experimental details). The cycling results are shown in Figure 1, from which it is apparent that the material can deliver a high capacity of around 284 mAh/g and, after some initial fade, can retain a capacity of 200 mAh/g at a rate of 15 mA g^{-1} . Remarkably, the mesostructure is preserved throughout cycling, as demonstrated by the TEM data in Figure 2. After 30 cycles of intercalating and deintercalating Li within the walls, the ordered mesostructure is clearly present and the high resolution data indicate preservation of the detailed pore structure.

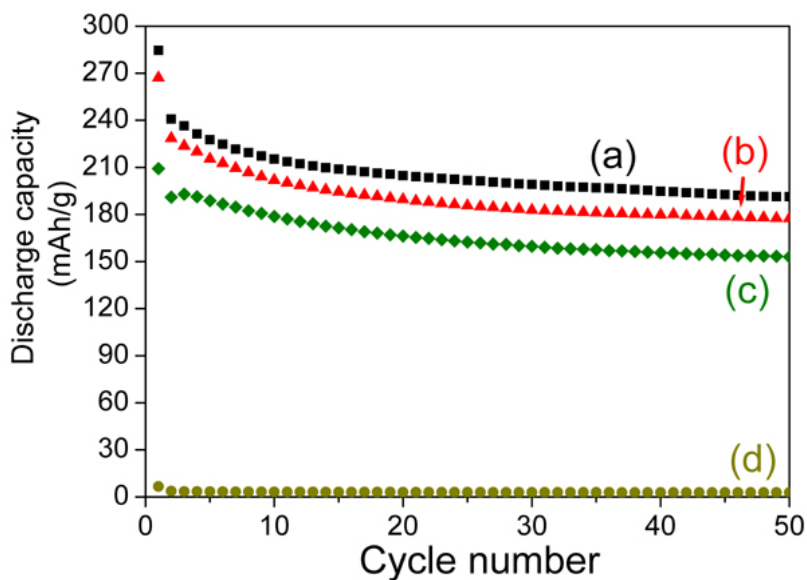


Figure 1. Capacity retention for mesoporous $\beta\text{-MnO}_2$ cycled at (a) 15 mA/g, (b) 30 mA/g, and (c) 300 mA/g; (d) bulk $\beta\text{-MnO}_2$ cycled at 15 mA/g.

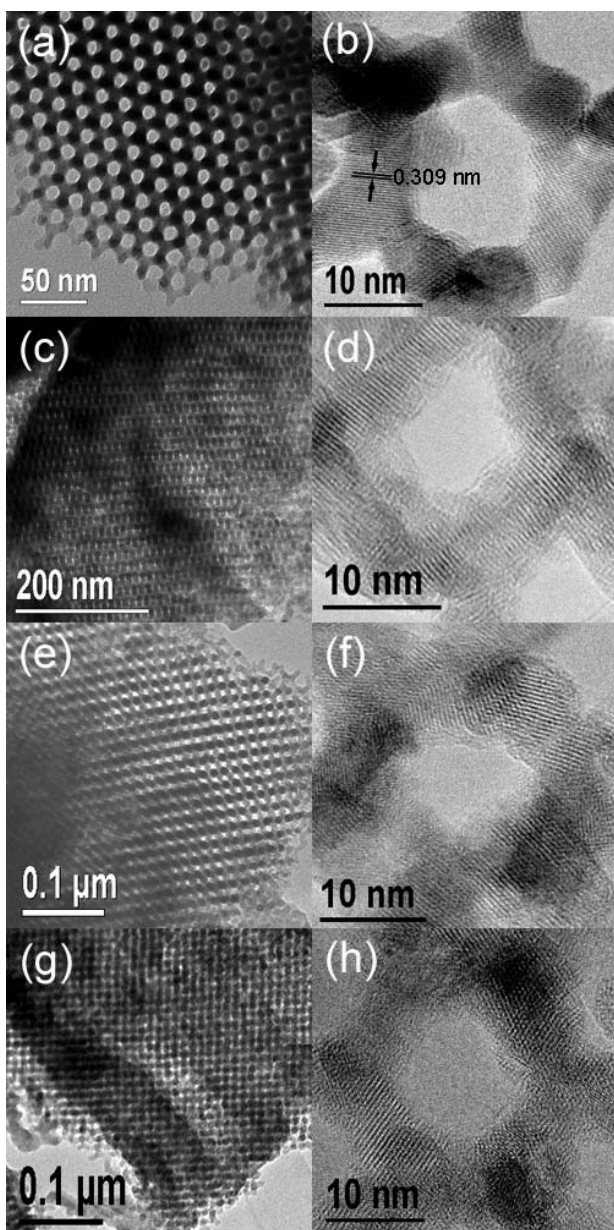


Figure 2. TEM and HRTEM images of mesoporous β -MnO₂: (a, b) as-prepared, (c, d) after first discharge, (e, f) end of discharge after 30 cycles, and (g, h) end of charge after 30 cycles.

The electrochemical behaviour of highly crystalline mesoporous β -MnO₂ is in sharp contrast to bulk crystalline β -MnO₂, which shows no ability to electrochemically intercalate lithium, Figure 1(d).¹⁰ Both materials are composed of micron sized particles, the difference being that the mesoporous material also contains pores within the particles. A previous report suggested a very limited amount of Li, 0.25Li per MnO₂- β , could be

intercalated electrochemically into bulk crystalline β - MnO_2 , but our results do not support the existence of even this small capacity.^{7, 10} Nanoparticles of β - MnO_2 , if synthesised along with acetylene black thus forming an intimate nanocomposite of carbon coated nanoparticles, show some similarity in their behaviour to mesoporous β - MnO_2 , in that both can sustain electrochemical cycling, however the former converts to a spinel structure on cycling whereas the latter does not, as discussed below.¹¹ The stark difference between the behaviour of bulk and mesoporous β - MnO_2 is due to kinetics. Something that is borne out by the fact that carbon coated nanoparticulate β - MnO_2 can be electrochemically cycled. In view of the fact that the kinetics of the bulk material as so poor as to render it electrochemically inactive, it is remarkable that the capacity of the mesoporous material decreases by only 19% on increasing the rate from 15 to 300 mA g^{-1} i.e. by a factor of 20. A capacity of 154 mAh/g is obtained after 50 cycles at a rate of 300 mAh/g , corresponding to $\sim 2C$ (where C rate is defined as complete discharge in one hour). The origin of the difference in electrochemical activity between the mesoporous and bulk materials lies in the fact that electrolyte can flood the pores within the μm sized particles of the former, giving a high contact area; this, along with the thin walls, which ensures short diffusion distances for Li^+ , results in more facile intercalation/de-intercalation in contrast to the almost non-existent electrochemistry for the bulk material.

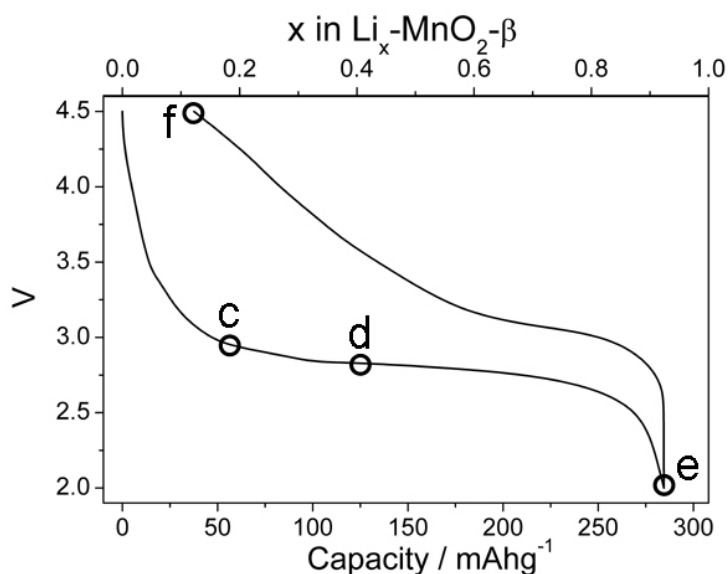


Figure 3. Variation of voltage with state of charge (capacity) for mesoporous β - MnO_2 . The PXRD patterns were taken at different stages, e.g. c, d, e, and f.

The variation of voltage on discharge (lithium intercalation) and then charge (lithium de-intercalation) is shown in Figure 3. The potential falls rapidly to a plateau at ~ 2.8 V, at the end of which the voltage decreases to the 2V cut-off. On charging, a plateau is again observed. The plateaux in the charge/discharge curves are consistent with a two phase reaction. PXRD data were collected at each of the points shown in Figure 3, and are presented in Figure 4(ii). Examination of PXRD data on the plateau, corresponding to point d in Figure 3, shows that, in addition to peaks associated with β -MnO₂, there are peaks at 47, 53, and 67 ° in 2θ . These peaks may be indexed on the same β -MnO₂ structure (space group P4₂/mnm) but with an increased cell volume, corresponding to expansion along **a** and a slight contraction along **c**, compared with pure β -MnO₂ (β -MnO₂ **a** = 4.40 Å, **c** = 2.88 Å and Li_x-MnO₂- β **a** = 4.96 Å, **c** = 2.82 Å). Considering the PXRD data in Figure 4.ii(e), corresponding to point e in Figure 3, i.e. at the end of discharge, the same two closely related phases are apparent, but with **a** and **c** having further expanded and contracted respectively (**a** = 5.01 Å and **c** = 2.81 Å). At the end of the subsequent charge, point f in Figure 3, the structure remains a mixture of pure β -MnO₂ and Li_x-MnO₂- β , removal of lithium from Li_x-MnO₂- β has resulted in a contraction along **a** and expansion along **c**. It can be concluded from the electrochemical and PXRD data that intercalation of lithium into the walls of mesoporous β -MnO₂ occurs with minimal distortion of the structure, simply involving two closely related phases, β -MnO₂ and a lithiated β -MnO₂ with different lattice dimensions.

It has been shown that reaction of bulk β -MnO₂ with n-butyllithium results in conversion of the structure to the spinel phase LiMn₂O₄ (or the lithiated form LiMn₂O₄), involving a major change in the oxygen arrangement from hexagonal close packing (strictly tetragonal packing) to cubic close packing.⁷ The PXRD patterns for LiMn₂O₄ and Li₂Mn₂O₄ are shown in Figure 4.ii(e); there is no evidence supporting the formation of these or any other phases at the end of the first discharge, except Li_x-MnO₂- β . This further illustrates the difference between mesoporous β -MnO₂ and the bulk material. PXRD data collected after 30 cycles at the end of discharge, Figure 4.ii(h), demonstrate that the material still contains β -MnO₂ and Li_x-MnO₂- β , with no evidence of a structural transformation to LiMn₂O₄ or Li₂Mn₂O₄. In contrast, the intimate composite between

nanoparticulate β -MnO₂ and acetylene black, referred to above, converts to spinel on the second discharge when electrochemically cycled. It may be concluded that the behaviour of mesoporous β -MnO₂ is unique, distinct from bulk or nanoparticulate β -MnO₂. A new peak does appear at 57° [asterisk in Figure 4.ii(h)], which we cannot identify at present.

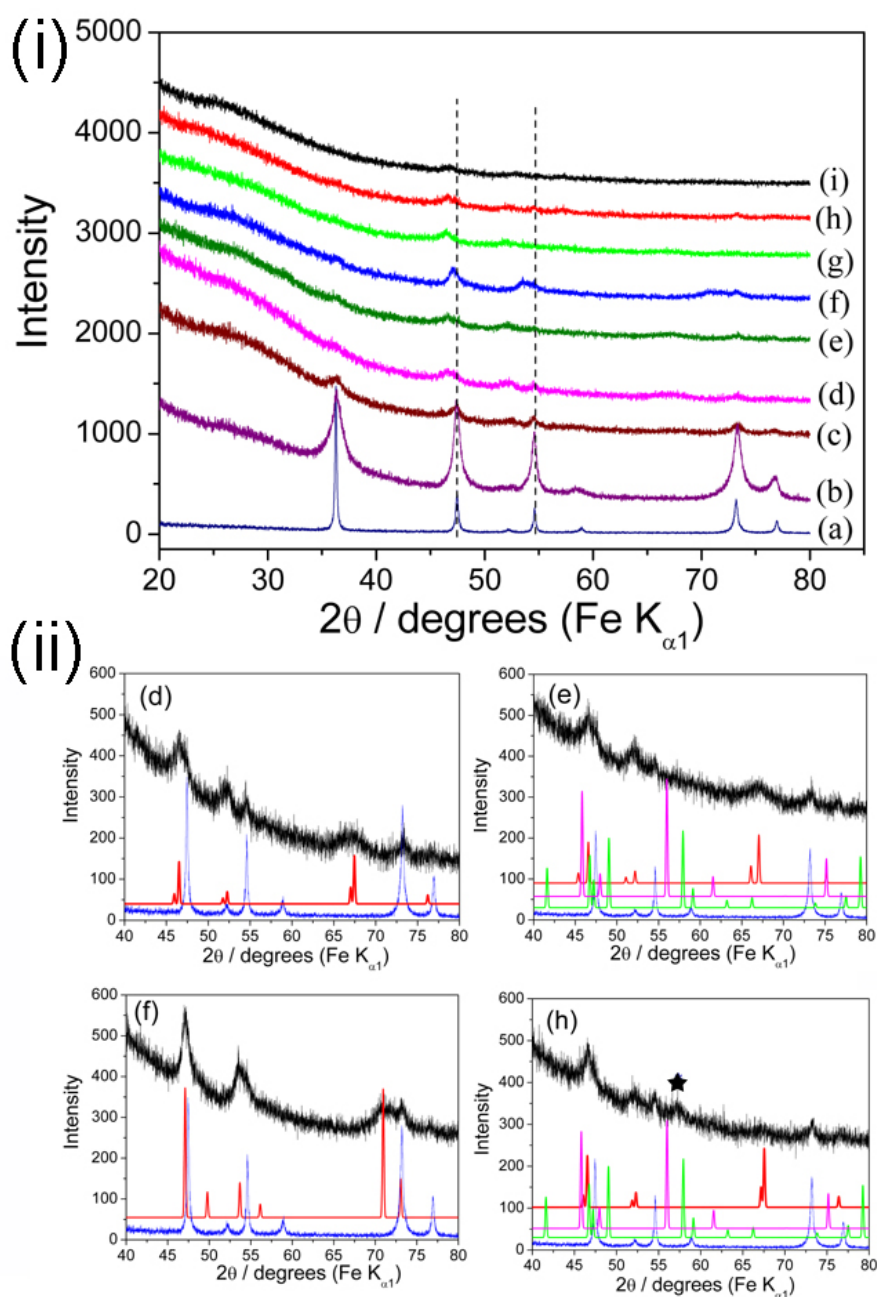


Figure 4. (i) PXR D patterns for as-prepared (a) bulk and (b) mesoporous β -MnO₂, (c) mesoporous β -MnO₂ discharged to 2.8V, (d) 2.7 V, (e) 2.0 V, then (f) charged to

4.5V, (g) end of discharge after 2 cycles, (h) end of discharge after 30 cycles, and (i) end of charge after 50 cycles; (ii) Expanded region of (d), (e), (f), and (h) PXRD patterns, bulk β -MnO₂ (blue line) and simulations of Li_x-MnO₂- β (red line), LiMn₂O₄ (pink line) and Li₂Mn₂O₄ (green line).

5-2-3 Conclusions

In conclusion, mesoporous β -MnO₂ with highly crystalline walls has shown to accommodate reversibly a large amount of lithium (0.92 Li/Mn) on intercalation, with 81% capacity retention on increasing the rate 20 fold after 50 cycles. This may be contrasted with bulk crystalline β -MnO₂ which accommodates little or no Li on electrochemical intercalation. The ordered mesoporous structure is preserved on cycling as is the β -MnO₂ crystal structure of the walls, unlike chemical intercalation into bulk β -MnO₂ or electrochemical reaction with nanoparticulate β -MnO₂, both of which convert rapidly to LiMn₂O₄ spinel. The thin walls of the mesoporous material can accommodate the volume changes as Li is cycled in β -MnO₂ and this is likely to be responsible for preservation of the crystal structure on cycling, rather than conversion to spinel, as well as explaining the maintenance of the ordered mesostructure. Li intercalation into crystalline mesoporous β -MnO₂ is unique, exhibiting differences from crystalline bulk and nanoparticulate β -MnO₂.

5-2-4 References

- ¹ T. Nagaura and K. Tozawa, *Prog. Batteries Solar Cells*, 1990, **9**, 209.
- ² W. A. Van Schalkwijk and B. Scrosati, *Advances in Lithium-Ion Batteries*, 2002, Kluwer Academic/Plenum Publishers New York.
- ³ P. G. Bruce, *Chemical Communications*, 1997, 1817.
- ⁴ L. Sannier, R. Bouchet, S. Grugeon, E. Naudin, E. Vidal, and J. M. Tarascon, *Journal of Power Sources*, 2005, **144**, 231.
- ⁵ P. G. Bruce, A. R. Armstrong, and R. L. Gitzendanner, *Journal of Materials Chemistry*, 1999, **9**, 193.
- ⁶ P. G. Bruce, A. R. Armstrong, and H. T. Huang, *Journal of Power Sources*, 1997, **68**, 19.
- ⁷ M. M. Thackeray, *Progress in Solid State Chemistry*, 1997, **25**, 1.
- ⁸ M. M. Thackeray, W. I. F. David, P. G. Bruce, and J. B. Goodenough, *Materials Research Bulletin*, 1983, **18**, 461.

- ⁹ M. M. Thackeray, P. J. Johnson, L. A. Depicciotto, P. G. Bruce, and J. B. Goodenough, *Materials Research Bulletin*, 1984, **19**, 179.
- ¹⁰ L. I. Hill, A. Verbaere, and D. Guyomard, *Journal of Power Sources*, 2003, **119**, 226.
- ¹¹ W. P. Tang, X. J. Yang, Z. H. Liu, and K. Ooi, *Journal of Materials Chemistry*, 2003, **13**, 2989.

Chapter 6. Characterization of mesoporous materials synthesized by post-templating method

6-1 Mesoporous Fe₃O₄ and γ -Fe₂O₃: synthesis, structure characterization and magnetic properties

The synthesis of mesoporous transition metal oxides usually includes a templating approach (see Chapter 3 and 4 for examples).¹⁻⁴ This can restrict the range of transition metal oxides that may be prepared to those containing transition metal ions stable in solution and/or to compounds that form within the thermal stability range of the template.⁵ Reduced mesoporous iron oxides are of particular interest because of their potential use in magnetic storage or as catalysts but have not been prepared previously.^{6,7}

Here, by introducing a post-templating method, mesoporous α -Fe₂O₃ may be converted to Fe₃O₄ by reduction, then to γ -Fe₂O₃ by oxidation, whilst preserving the mesostructure. The materials exhibit highly crystalline walls throughout the solid-solid conversion. This is the first synthesis of mesoporous Fe₃O₄ or indeed any reduced iron oxide because such materials cannot easily be prepared directly due to the instability of Fe²⁺ in the whole synthesis process.⁵

6-1-1 Synthesis

Three dimensional mesoporous silica (KIT-6) with Ia-3d symmetry was used as hard template. The synthesis of mesoporous KIT-6 has been described in Chapter 2. In a typical synthesis of mesoporous Fe₃O₄: 1 g of Fe(NO₃)₃·9H₂O (98%, Aldrich) was dissolved in 20 mL of ethanol, followed by addition of 1 g of mesoporous silica, KIT-6. After stirring at room temperature until all the solution had been absorbed and a dry powder obtained, the sample was heated slowly to 600 °C in air and calcined at that temperature for 6 h. The resulting sample was twice treated with a hot 2M NaOH solution to remove the silica template, followed by washed with water and ethanol several times, and then drying at 60 °C. This procedure leads to mesoporous α -Fe₂O₃ with crystalline walls as described in Chapter 4-1. Reduction was achieved by heating at 350 °C for 1h under a 5% H₂-95% Ar atmosphere. Mesoporous Fe₃O₄ was stored under Ar and all structure characterization was carried out without exposure to air. For the preparation of mesoporous γ -Fe₂O₃, the as-prepared mesoporous Fe₃O₄ was heated at 150 °C for 2 h in air.

6-1-2 Structure characterization

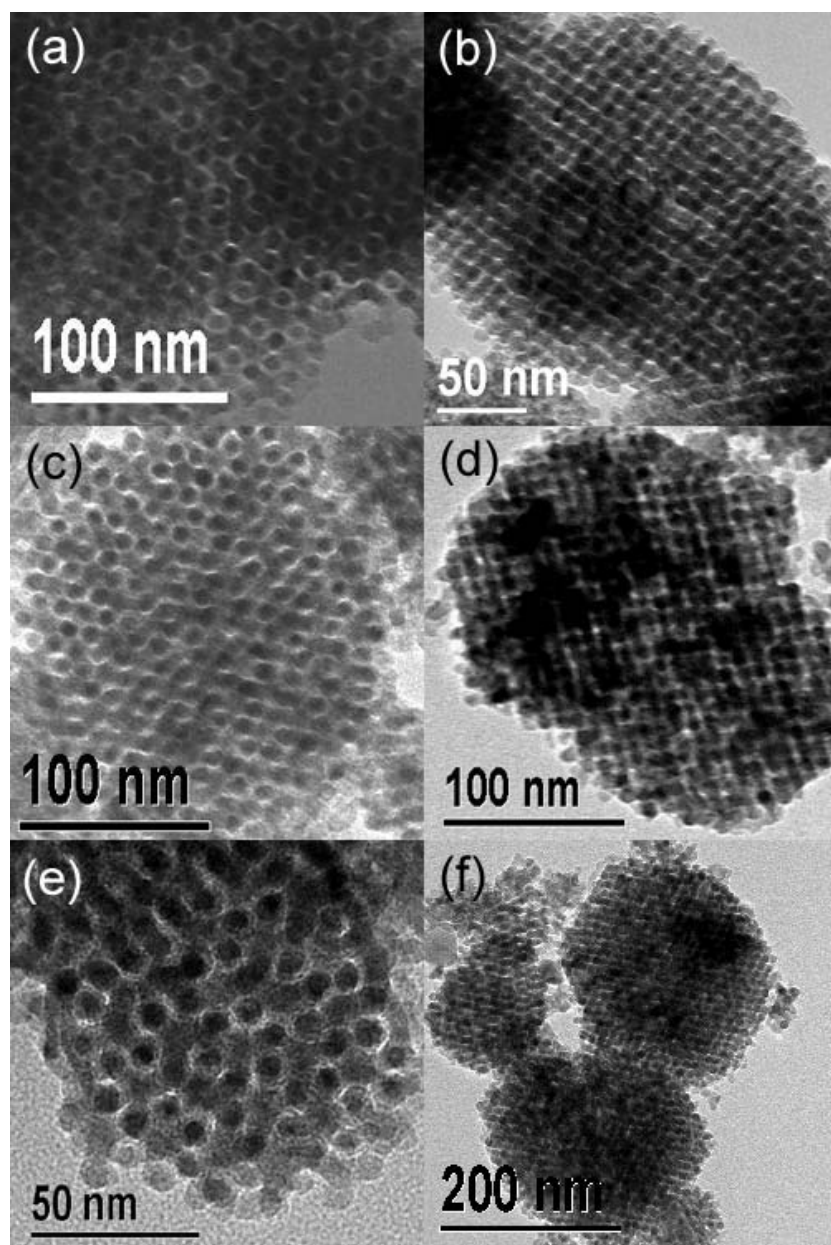


Figure 1. TEM images for mesoporous (a, b) α -Fe₂O₃, (c, d) Fe₃O₄ and (e, f) γ -Fe₂O₃ recorded along the [111] and [110] directions, respectively.

The highly ordered mesostructures of α -Fe₂O₃, Fe₃O₄ and γ -Fe₂O₃ are evident in Figure 1. Although the synthesis of ordered mesoporous α -Fe₂O₃ using KIT-6 and its characterization by TEM, PXRD and N₂ adsorption-desorption have been discussed previously in Chapter 4-1, the TEM data are included here to demonstrate retention of the mesoporous structure during the reduction and oxidation. For all three mesoporous materials the symmetry is that anticipated for a replica of the KIT-6 template structure (1a-3d). The a_0 parameters extracted from the TEM data are 23.2 nm (α -Fe₂O₃), 24.4 nm (Fe₃O₄) and 23.0

nm (γ -Fe₂O₃). These data indicate that the mesostructure is maintained throughout the reduction and oxidation with only a slight expansion on conversion from α -Fe₂O₃ to Fe₃O₄ and contraction on transformation from Fe₃O₄ to γ -Fe₂O₃. The high-resolution TEM (HRTEM) images in Figure 2 show the detailed structure of the mesopores. The ordered mesostructures and pore shapes of α -Fe₂O₃, Fe₃O₄ and γ -Fe₂O₃ seen in Figure 1 are typical of those observed throughout the materials, based on examining many different regions and many particles. The results of low angle powder X-ray diffraction data for Fe₃O₄ and γ -Fe₂O₃ are shown in Fig. 3a and b. Both materials exhibit a peak around 0.9° in 2 θ assigned to the [211] reflection, with a weaker secondary peak at about 1.7° (Cu_{K α 1}). From the low angle [211] reflection, the a_0 parameters for Fe₃O₄ and γ -Fe₂O₃ were determined to be 24.5 nm and 23.4 nm respectively, values that are in good agreement with those obtained from the TEM data in Figure 1.

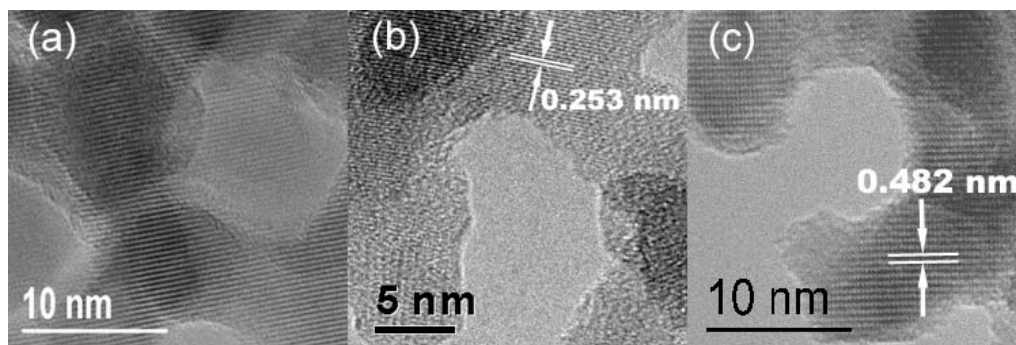


Figure 2. HRTEM images for mesoporous (a) α -Fe₂O₃, (b) Fe₃O₄ and (c) γ -Fe₂O₃.

The above results demonstrate that mesoporous α -Fe₂O₃ can convert to Fe₃O₄ then to γ -Fe₂O₃ with retention of the mesostructure. During the transformation, the oxygen subarrays convert from hcp to ccp, involving the sheaving of oxygen layers, from AB to ABC stacking. The thin walls endow the mesoporous solids with a flexibility that aids such solid/solid transformations whilst preserving the mesostructure.

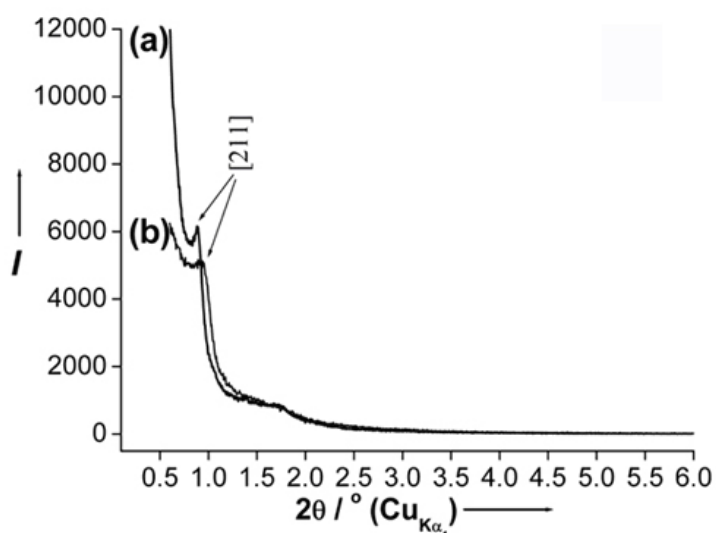


Figure 3. Low-angle PXRD patterns for mesoporous (a) Fe_3O_4 and (b) $\gamma\text{-Fe}_2\text{O}_3$.

N_2 sorption isotherms were collected for $\gamma\text{-Fe}_2\text{O}_3$ and are presented in Fig. 4a. Because, mesoporous Fe_3O_4 is oxidised to γ -phase Fe_2O_3 on exposure to air, it was not possible to obtain reliable sorption isotherms for Fe_3O_4 . The data for $\gamma\text{-Fe}_2\text{O}_3$ exhibit a type IV isotherm, typical of a mesoporous transition metal oxide prepared by the hard-templating method.^{3, 8, 9} The pore size distribution is shown in Fig. 4b. The peak is centred around 3.6 nm, which is in good agreement with the value expected for a replica of the KIT-6 structure. The Brunauer- Emmett-Teller (BET) surface area for mesoporous $\gamma\text{-Fe}_2\text{O}_3$ is $86 \text{ m}^2\text{g}^{-1}$.

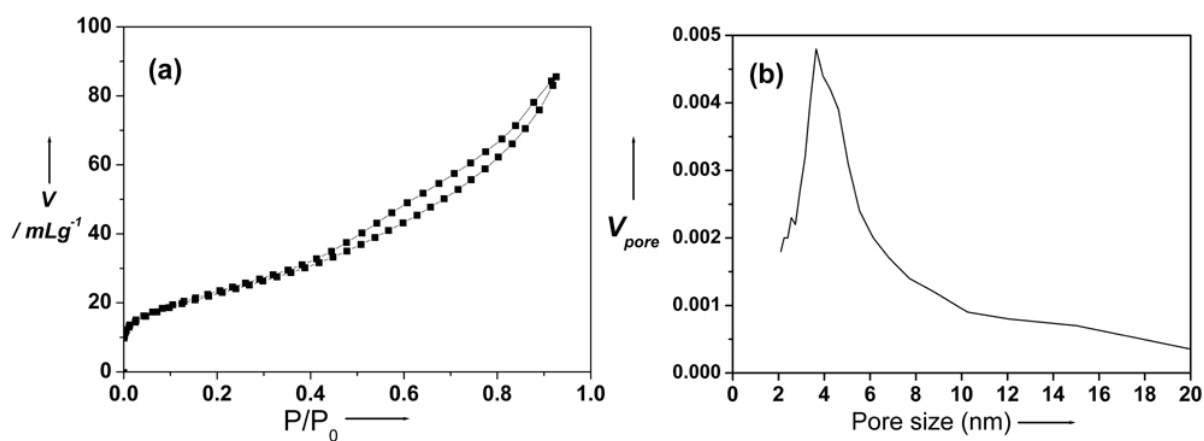


Figure 4. (a) N_2 adsorption-desorption isotherms and (b) pore size distribution for mesoporous $\gamma\text{-Fe}_2\text{O}_3$.

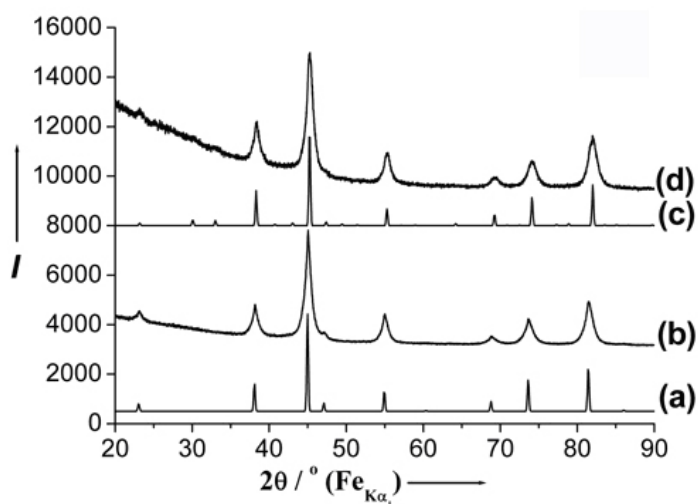


Figure 5. Wide-angle PXRD patterns for (a) bulk Fe_3O_4 , (b) mesoporous Fe_3O_4 , (c) bulk $\gamma\text{-Fe}_2\text{O}_3$ and (d) mesoporous $\gamma\text{-Fe}_2\text{O}_3$.

Turning to the structures of the walls, it is evident from the wide-angle powder X-ray diffraction data, Fig. 5b and d, that the walls are highly crystalline; the PXRD data exhibit well-defined peaks corresponding to the crystal structures of Fe_3O_4 (Figure 5b) and $\gamma\text{-Fe}_2\text{O}_3$ (Figure 5d). Although the diffraction patterns look similar for both compounds, they are different with different space groups ($Fd\bar{3}m$ and $P4_332$ for Fe_3O_4 and $\gamma\text{-Fe}_2\text{O}_3$, respectively) and lattice parameters that differ significantly (8.385 \AA and 8.346 \AA for Fe_3O_4 and $\gamma\text{-Fe}_2\text{O}_3$, respectively, JCPDS Nos. 19-629 and 25-1402). Refinement using the Rietveld method yielded cubic lattice parameters of $8.383(2) \text{ \AA}$ (Fe_3O_4) and $8.343(2) \text{ \AA}$ ($\gamma\text{-Fe}_2\text{O}_3$) for the mesoporous materials, in excellent agreement with literature values (Figure 6).

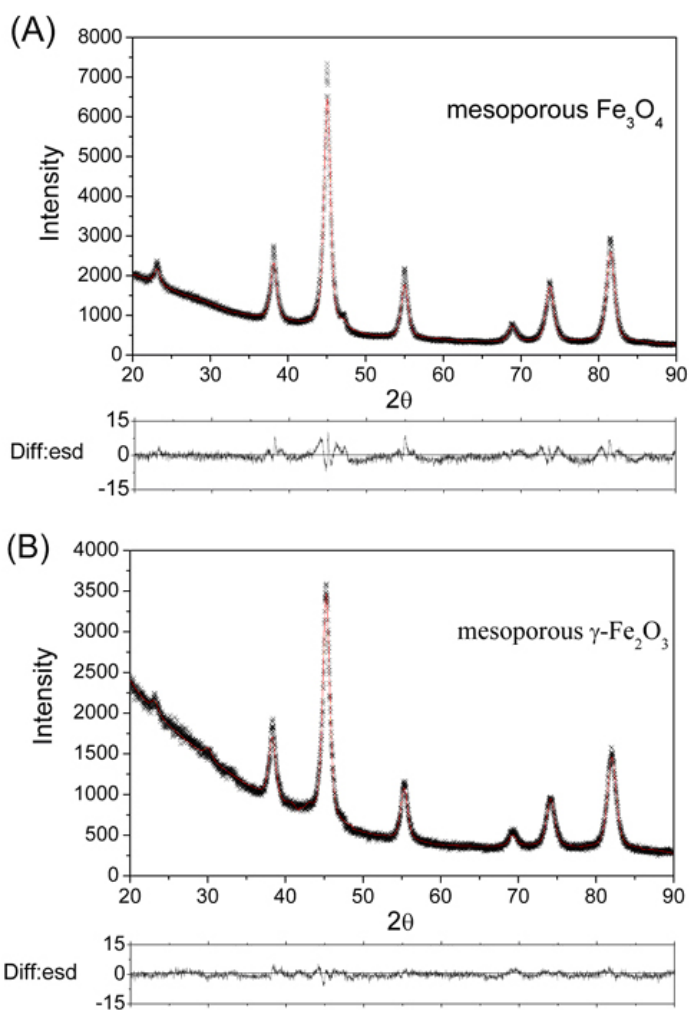


Figure 6. The PXRD refinements and difference curves for (A) mesoporous Fe_3O_4 and (B) mesoporous $\gamma\text{-Fe}_2\text{O}_3$ (\times for experimental data and red line for best fit).

These results demonstrate that Fe_3O_4 spinel has been successfully synthesized and converted to $\gamma\text{-Fe}_2\text{O}_3$; further corroboration of the Fe_3O_4 formation and conversion to $\gamma\text{-Fe}_2\text{O}_3$ has been obtained from EXAFS/XANES and is discussed later. Although the PXRD data indicate that the walls are highly crystalline, examination of the HRTEM images in Figure 2b and c show that each particle is not a single crystal, instead the lattice fringes run in different directions in different regions of the particles. Lattice fringe spacings 2.53 Å and 4.82 Å are highlighted in Figure 2b and c and correspond well with the d spacings of the [311] and [113] reflections for Fe_3O_4 and $\gamma\text{-Fe}_2\text{O}_3$, respectively, in agreement with the values of 2.532 Å and 4.82 Å obtained from the JCPDS database (JCPDS Nos. 19-629 and 25-1402).

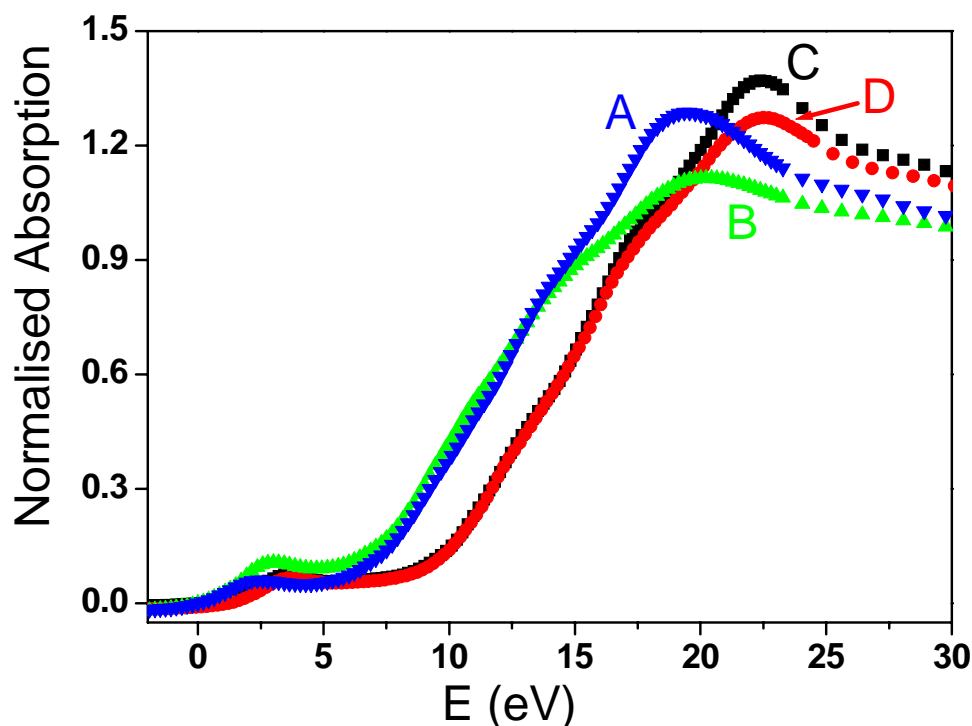


Figure 7. XANES data for (A) bulk Fe_3O_4 (blue line), (B) mesoporous Fe_3O_4 (green line), (C) bulk $\gamma\text{-Fe}_2\text{O}_3$ (black line) and (D) mesoporous $\gamma\text{-Fe}_2\text{O}_3$ (red line).

Further confirmation that a mesoporous compound with the composition Fe_3O_4 has been prepared and then converted to $\gamma\text{-Fe}_2\text{O}_3$ was obtained from EXAFS/XANES. The Fe L_1 XANES of mesoporous Fe_3O_4 and $\gamma\text{-Fe}_2\text{O}_3$ are presented in Figure 7, after the smooth pre-edge background subtraction and normalization. The XANES data for the bulk materials are also shown for comparison. It is clear that mesoporous Fe_3O_4 and $\gamma\text{-Fe}_2\text{O}_3$ have average oxidation states of +2.66 and +3, respectively. The Fourier transformed EXAFS data are presented in Figure 8 along with data for the corresponding bulk phases. The data for the mesoporous and corresponding bulk materials are identical, confirming the results from the powder X-ray diffraction measurements. The differences between the spectra for Fe_3O_4 and $\gamma\text{-Fe}_2\text{O}_3$ further confirm that the two different forms of iron oxide have been prepared.

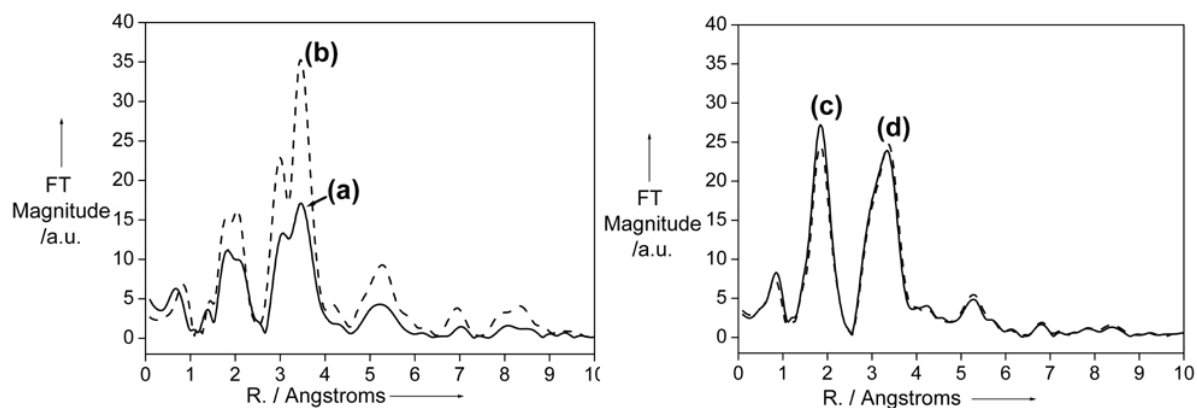


Figure 8. EXAFS results for (a) mesoporous Fe_3O_4 (solid line), (b) bulk Fe_3O_4 (dash line), (c) mesoporous $\gamma\text{-Fe}_2\text{O}_3$ (solid line) and (d) bulk $\gamma\text{-Fe}_2\text{O}_3$ (dash line).

6-1-3 Magnetic properties

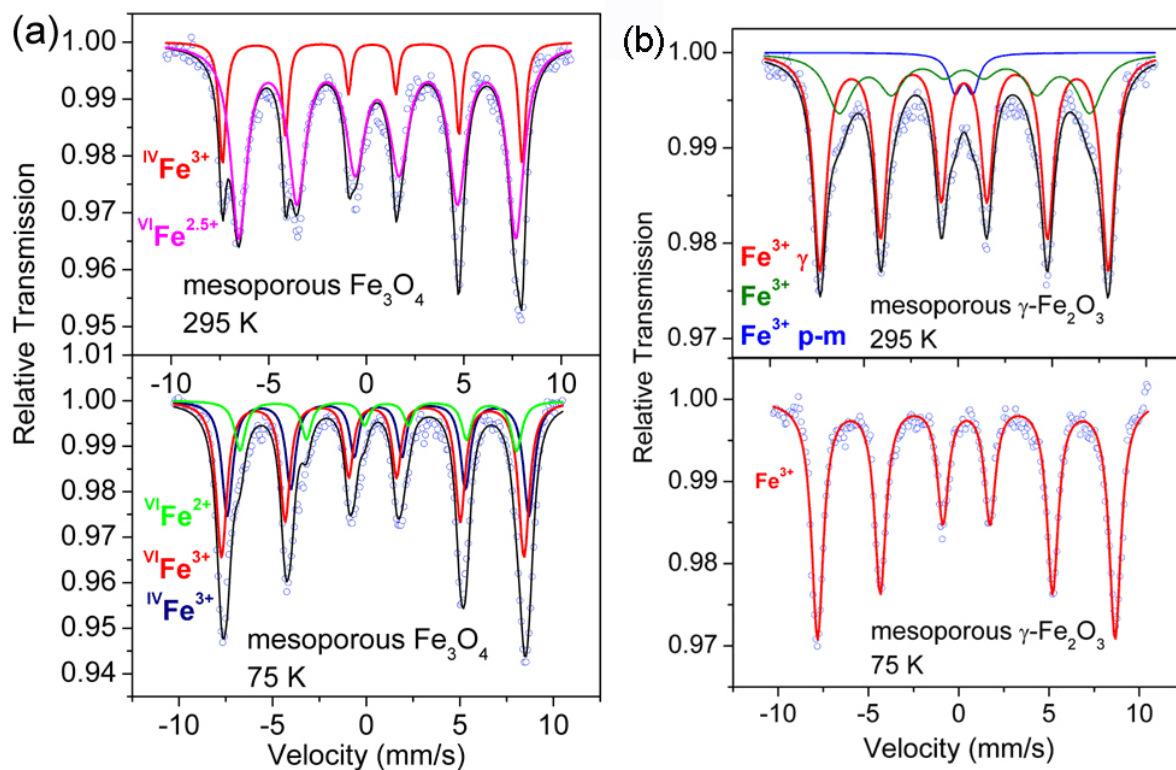


Figure 9. Mössbauer data recorded at 295 K and 75 K for mesoporous (a) Fe_3O_4 and (b) $\gamma\text{-Fe}_2\text{O}_3$ (open circles: experimental data and solid black line: best fit).

Mössbauer data are presented in Figure 9 for mesoporous Fe_3O_4 and $\gamma\text{-Fe}_2\text{O}_3$ at 75 and 295 K. The data for Fe_3O_4 , inverse spinel ($\text{Fe}_{\text{tet}}^{3+}[\text{Fe}^{2+}\text{Fe}^{3+}]_{\text{oct}}\text{O}_4$) at 295K are composed of two sextuplets, one corresponding to the tetrahedral site Fe^{3+} ion and the other to an average oxidation state of $\text{Fe}^{2.5+}$ in an octahedral site (Figure 8a). The latter is consistent with

electron exchange between the high spin Fe^{2+} and Fe^{3+} ions in the 16d octahedral sites of the Fd3m spinel structure being sufficiently rapid, on the timescale of the Mössbauer experiment, to ensure that the individual iron ions are indistinguishable. Bulk magnetite undergoes the characteristic Verwey transition in the region of 120 K, manifested most distinctively by a metal-insulator transition on cooling. The traditional rationalisation of this transition involves a localisation and ordering of charge on the Fe^{2+} and Fe^{3+} ions of the octahedral sites in the low temperature state, though there is still considerable debate about this.^{10, 11} Data taken at 75 K on mesoporous Fe_3O_4 are compatible with such charge ordering: three sextuplets may be distinguished, corresponding to tetrahedral Fe^{3+} , octahedral Fe^{3+} and octahedral Fe^{2+} (Figure 9a). At both temperatures the Mössbauer data are consistent with magnetic ordering. The magnetisation data (Figure 10a) are also consistent with this conclusion: a divergence in field-cooled (fc) and zero-field-cooled (zfc) data indicate that spin freezing has occurred at the highest experimental temperature of 340 K (bulk Fe_3O_4 undergoes a paramagnetic to ferromagnetic transition around 850 K). The Verwey transition is sometimes manifested in Fe_3O_4 as an anomaly in the magnetisation, but we see no sign of such a feature; however this can, in some cases, be difficult to detect by dc magnetisation.^{12, 13}

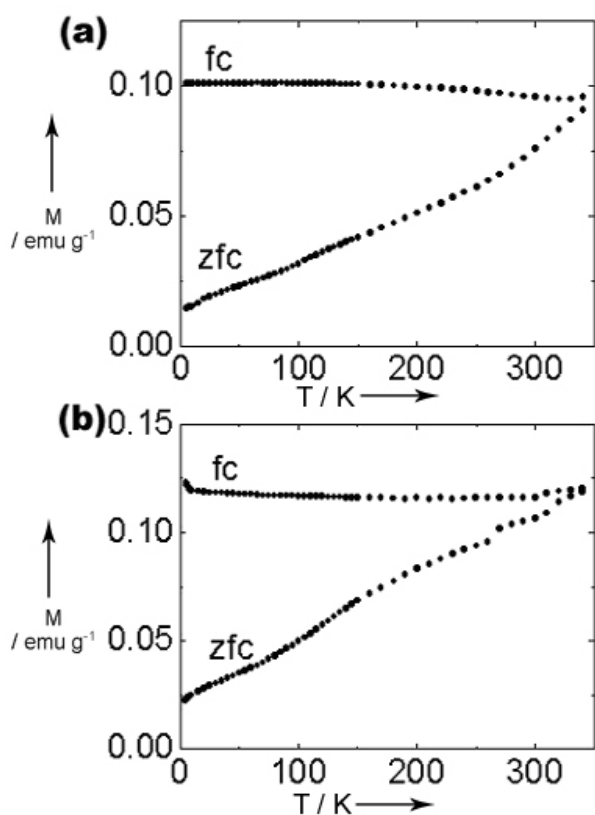


Figure 10. Magnetisation measured after cooling in zero field (zfc) and then in a field of 0.01 T (fc) for mesoporous (a) Fe_3O_4 and (b) $\gamma\text{-Fe}_2\text{O}_3$.

Considering the Mössbauer data for γ -Fe₂O₃ and beginning with the data at 75 K, these data may be fitted by a single sextuplet (Fig. 9b). The literature on bulk γ -Fe₂O₃ indicates that although Fe³⁺ is present on both the tetrahedral and the octahedral sites of the spinel structure, the sextuplets of both sites overlap significantly, consistent with our observations at low temperatures for mesoporous γ -Fe₂O₃.¹⁴ At room temperature, the spectrum is again dominated by a sextuplet of Fe³⁺, in accord with the bulk material (Fig. 9b, labelled Fe³⁺ γ). However, there are two other contributions from Fe³⁺ to the data for mesoporous γ -Fe₂O₃ at room temperature, a sextuplet of much lower intensity (labelled Fe³⁺) and a weak doublet corresponding to paramagnetic Fe³⁺ (Fe³⁺ p-m). At both temperatures the Mössbauer data are consistent with magnetic order. The magnetisation data under zfc and fc conditions (Fig. 10b) indicate that spin freezing has occurred by 340 K, and are broadly consistent with data for bulk samples (magnetic ordering occurs in bulk γ -Fe₂O₃ below approximately 900 K); they are also compatible with magnetic order.

Further work is required to characterize the magnetic structures of mesoporous Fe₃O₄ and γ -Fe₂O₃ in more detail to address in particular the absence of the Verwey transition signature in the dc magnetisation measurements for Fe₃O₄ and to fully understand the various contributions to the Mössbauer data for γ -Fe₂O₃ at room temperature. However it is clear that mesoporous Fe₃O₄ and γ -Fe₂O₃ exhibit magnetic order. These results are in accord with recent observations of magnetic ordering in mesoporous α -Fe₂O₃ with crystalline walls, which has been discussed previously. In that case, long-range magnetic ordering was observed for a wall thickness of approximately 7 nm, despite the fact that nanoparticles of dimensions less than 8 nm exhibit a breakdown of magnetic order and superparamagnetic behaviour. The magnetic interactions along the 2D walls are sufficient to promote magnetic order. A similar mechanism may explain the observations of magnetic freezing in mesoporous Fe₃O₄ and γ -Fe₂O₃; such freezing is absent in nanoparticles of these phases at such temperatures if less than 8 nm in diameter. The retention of magnetic order at relatively high temperatures in mesoporous Fe₃O₄ and γ -Fe₂O₃ may be significant for technological applications.

6-1-4 Conclusions

Mesoporous Fe₃O₄ has been synthesized. This is the first synthesis of mesoporous Fe₃O₄ or any reduced mesoporous oxide, something that is difficult to carry out directly. Starting from ordered mesoporous α -Fe₂O₃ with crystalline walls, reduction results in the formation of Fe₃O₄ and then oxidation yields γ -Fe₂O₃ while preserving the same ordered mesostructure and crystalline walls throughout these solid/solid transformations, emphasizing the flexibility of mesoporous solids to such transformations. The magnetic properties of mesoporous Fe₃O₄ and γ -Fe₂O₃ have been characterized by Mössbauer and SQUID measurements. The materials exhibit magnetic freezing above 340 K despite wall thicknesses of ~ 7 nm; whereas nanoparticles of the corresponding iron oxides lose magnetic order below a particle size of 8 nm down to much lower temperatures.

6-1-5 References

- ¹ D. M. Antonelli, A. Nakahira, and J. Y. Ying, *Inorganic Chemistry*, 1996, **35**, 3126.
- ² D. M. Antonelli and J. Y. Ying, *Current Opinion in Colloid & Interface Science*, 1996, **1**, 523.
- ³ B. Z. Tian, X. Y. Liu, L. A. Solovyov, Z. Liu, H. F. Yang, Z. D. Zhang, S. H. Xie, F. Q. Zhang, B. Tu, C. Z. Yu, O. Terasaki, and D. Y. Zhao, *Journal of the American Chemical Society*, 2004, **126**, 865.
- ⁴ P. D. Yang, D. Y. Zhao, D. I. Margolese, B. F. Chmelka, and G. D. Stucky, *Nature*, 1998, **396**, 152.
- ⁵ T. Brezesinski, M. Groenewolt, M. Antonietti, and B. Smarsly, *Angewandte Chemie-International Edition*, 2006, **45**, 781.
- ⁶ C. T. Yavuz, J. T. Mayo, W. W. Yu, A. Prakash, J. C. Falkner, S. Yean, L. L. Cong, H. J. Shipley, A. Kan, M. Tomson, D. Natelson, and V. L. Colvin, *Science*, 2006, **314**, 964.
- ⁷ D. A. Bazylinski, B. R. Heywood, S. Mann, and R. B. Frankel, *Nature*, 1993, **366**, 218.
- ⁸ F. Jiao, A. Harrison, J. C. Jumas, A. V. Chadwick, W. Kockelmann, and P. G. Bruce, *Journal of the American Chemical Society*, 2006, **128**, 5468.
- ⁹ Y. Q. Wang, C. M. Yang, W. Schmidt, B. Spliethoff, E. Bill, and F. Schuth, *Advanced Materials*, 2005, **17**, 53.
- ¹⁰ J. Garcia and G. Subias, *Journal of Physics-Condensed Matter*, 2004, **16**, R145.
- ¹¹ J. P. Wright, J. P. Attfield, and P. G. Radaelli, *Physical Review B*, 2002, **66**.
- ¹² G. F. Goya, T. S. Berquo, F. C. Fonseca, and M. P. Morales, *Journal of Applied Physics*, 2003, **94**, 3520.
- ¹³ S. P. Sena, R. A. Lindley, H. J. Blythe, C. Sauer, M. Al-Kafarji, and G. A. Gehring, *Journal of Magnetism and Magnetic Materials*, 1997, **176**, 111.
- ¹⁴ I. Tamura and M. Hayashi, *Journal of Magnetism and Magnetic Materials*, 1988, **72**, 285.

6-2 Mesoporous Mn₃O₄ with crystalline walls: synthesis, structural characterization and magnetic properties

The introduction of hard templates (eg mesoporous silica) results in sufficiently high processing temperatures to yield ordered mesopores with crystalline walls.¹⁻⁵ However, when used to synthesized transition metal oxides, the method is restricted in the oxidation states that are accessible.¹⁻³ In this section, the first synthesis of highly ordered mesoporous Mn₃O₄ with highly ordered (near single crystal) walls by first synthesizing highly ordered mesoporous Mn₂O₃, then reducing it to form highly crystalline Mn₃O₄, while retaining the ordered pore structure, is demonstrated.

6-2-1 Synthesis

Preparation of mesoporous silica KIT-6 has been described previously (Chapter 2). In a typical synthesis of mesoporous Mn₃O₄, 30 g of Mn(NO₃)₂·6H₂O (98%, Aldrich) was dissolved in ~ 20 mL of water to form a saturated Mn(NO₃)₂ solution. 5 g of mesoporous KIT-6 was dispersed in 200 mL of dried n-hexane. After stirring at room temperature for 3 h, 5 mL of the saturated Mn(NO₃)₂ solution was added slowly with stirring. The mixture was stirred overnight, filtered and dried at room temperature until a completely dried powder was obtained. The sample was heated slowly to 600 °C, calcined at that temperature for 3 h and the resulting material treated twice with a 2M hot NaOH solution in water, to remove the silica template, followed by washed with water several times, and then drying at 60 °C. This procedure results in mesoporous Mn₂O₃ (see Chapter 4-4). Reduction of mesoporous Mn₂O₃ to Mn₃O₄ was achieved by heating at 280 °C for 3h under a 5% H₂-95% Ar atmosphere.

6-2-2 Results and discussion

Although the structural characterization of mesoporous Mn₂O₃ with crystalline walls has been described in Chapter 4-4, some characterization data are included here to demonstrate the mesostructure retention during conversion from Mn₂O₃ to Mn₃O₄. TEM data, Figure 1, confirm the highly ordered mesostructure of Mn₃O₄ is preserved. The pore structure replicates that of the KIT-6 template, space group Ia-3d. Examining many different particles demonstrated that mesoporous structures are presented throughout the

mesoporous Mn_3O_4 material. The unit cell parameter, a_0 , extracted from the TEM data, is 24.9 nm for mesoporous Mn_3O_4 , which is similar to that for mesoporous Mn_2O_3 (25.1 nm). These data indicate that the mesostructure is maintained throughout the conversion from Mn_2O_3 to Mn_3O_4 . The low-angle powder X-ray diffraction (PXRD) pattern (Figure 2b) for mesoporous Mn_3O_4 exhibits one sharp peak at $\sim 0.9^\circ$, which could be indexed as the [211] reflection in Ia-3d space group and one broad peak at 1.7-1.8°, similar to the pattern for mesoporous Mn_2O_3 , further demonstrating the ordered mesostructure. The d-spacing value calculated from the first peak is 101.0 Å, which corresponds to the unit cell parameter, a_0 , 24.7 nm for mesoporous Mn_3O_4 , in good agreement with the TEM results (24.9 nm).

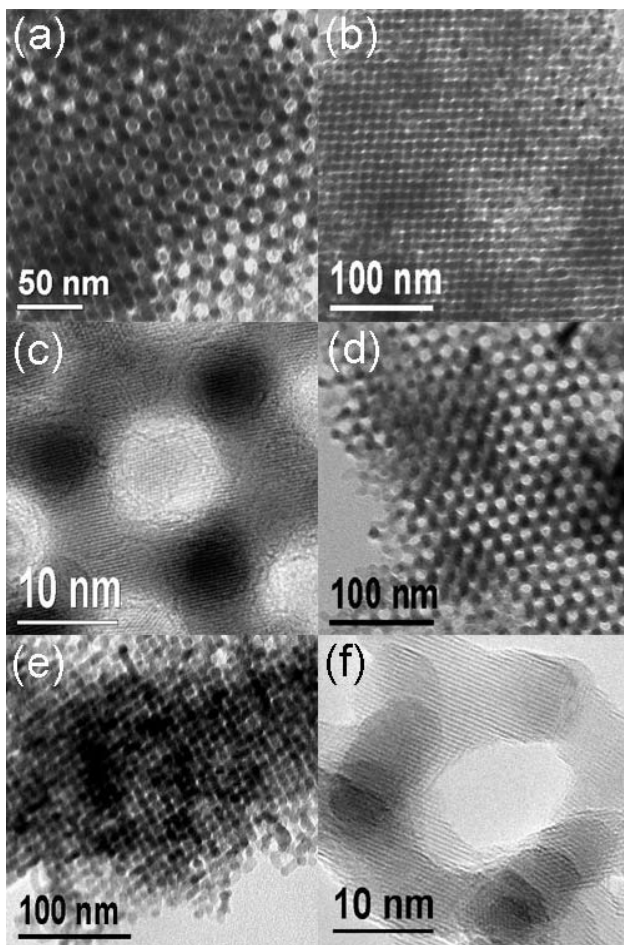


Figure 1. TEM images for mesoporous Mn_2O_3 recorded along the (a) [111] and (b) [110] direction, (c) HRTEM image for mesoporous Mn_2O_3 ; TEM images for mesoporous Mn_3O_4 recorded along the (d) [111] and (e) [110] directions, (f) HRTEM image for mesoporous Mn_3O_4 .

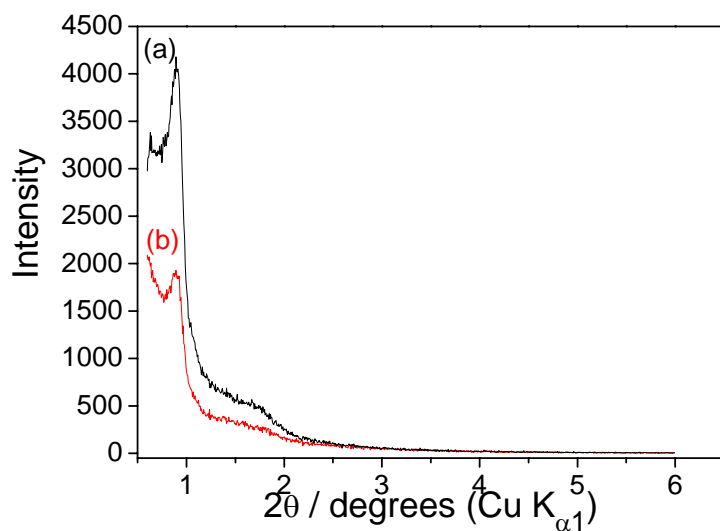


Figure 2. Low angle PXRD patterns for (a) mesoporous Mn_2O_3 and (b) mesoporous Mn_3O_4 .

The maintenance of mesostructure was further confirmed by nitrogen adsorption-desorption measurements. Type IV isotherms (Figure 3a) were observed for mesoporous Mn_3O_4 , consistent with the mesoporosity observed by TEM and low angle PXRD. The Brunauer-Emmett-Teller (BET) surface area for mesoporous Mn_3O_4 is $99.7 \text{ m}^2\text{g}^{-1}$, which is slightly lower than that for mesoporous Mn_2O_3 ($138.7 \text{ m}^2\text{g}^{-1}$). The pore size distributions calculated from desorption isotherms are shown in Figure 3b, exhibiting a narrow distribution centred at 3.68 nm for mesoporous Mn_3O_4 .

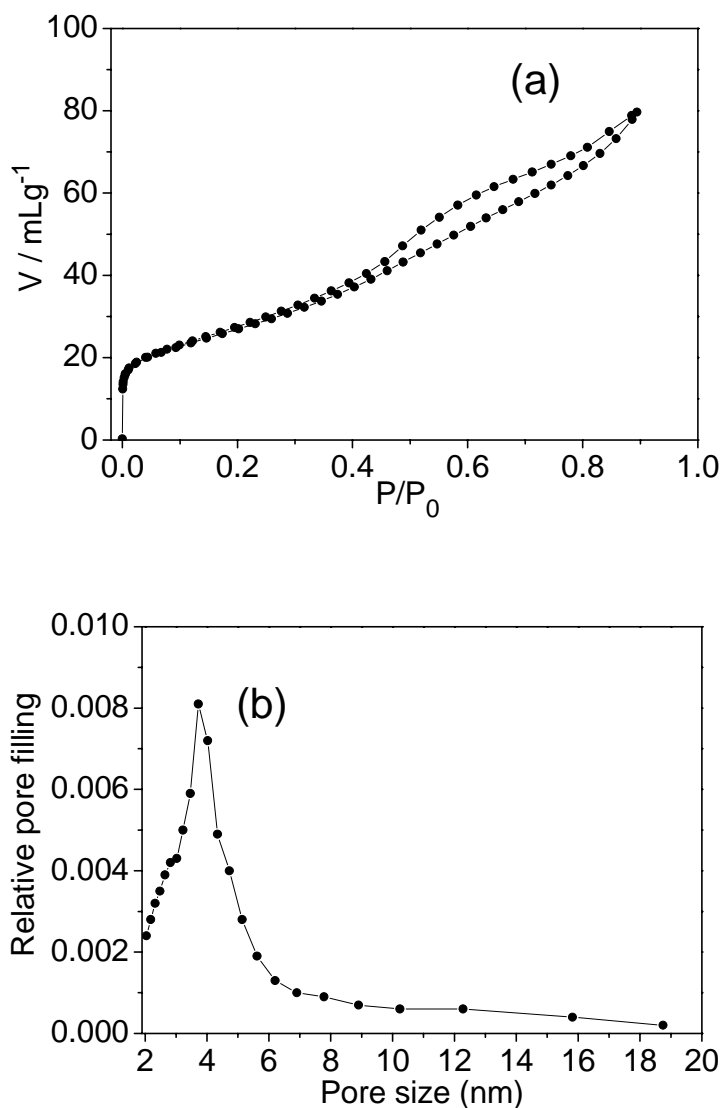


Figure 3. (a) N₂ adsorption-desorption isotherms and (b) the pore size distributions for mesoporous Mn₃O₄.

The high-resolution TEM (HRTEM) images (Figures 1c and f) showed the detailed structures of the pores. It is evident that the basic pore sharp is retained on conversion from Mn₂O₃ to Mn₃O₄, although the pore size for mesoporous Mn₃O₄ (Figure 1f) is slightly larger than that for Mn₂O₃ (Figure 1c), consistent with the nitrogen adsorption-desorption results. HRTEM results also indicate that the walls of mesoporous Mn₃O₄ are crystalline, which is further confirmed by the wide-angle PXRD results (Figure 4). Peaks corresponding to the crystal structures of Mn₂O₃ and Mn₃O₄ (JCPDS

Nos. 24-508 and 24-734, respectively) are evident in the figure. Further evidence supporting the conversion of Mn_2O_3 to Mn_3O_4 has been obtained by XANES analysis. The XANES results (Figure 5) clearly confirm the oxidation state of Mn in mesoporous Mn_3O_4 is +2.67.

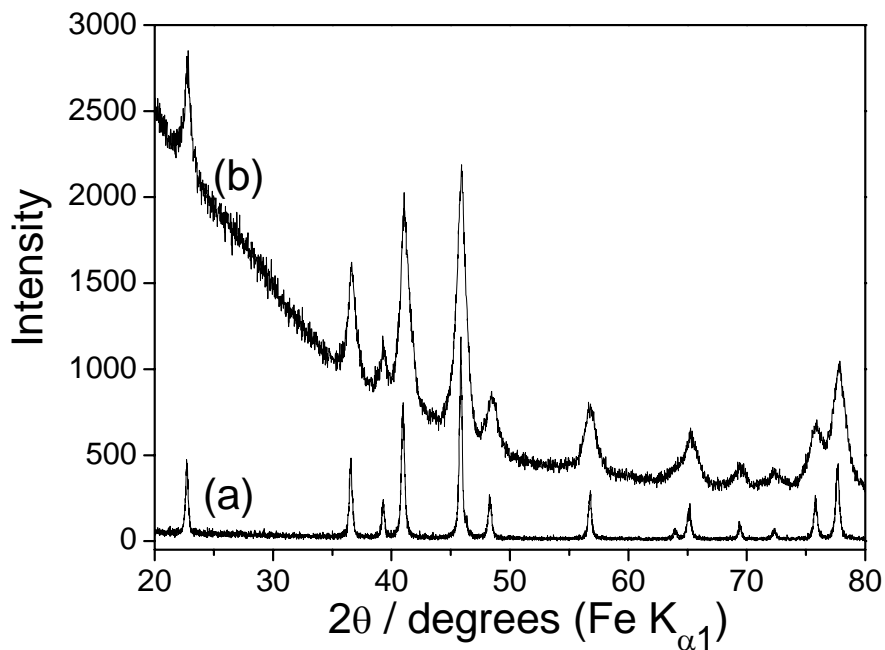


Figure 4. Wide-angle PXRD patterns for (a) bulk Mn_3O_4 and (b) mesoporous Mn_3O_4 .

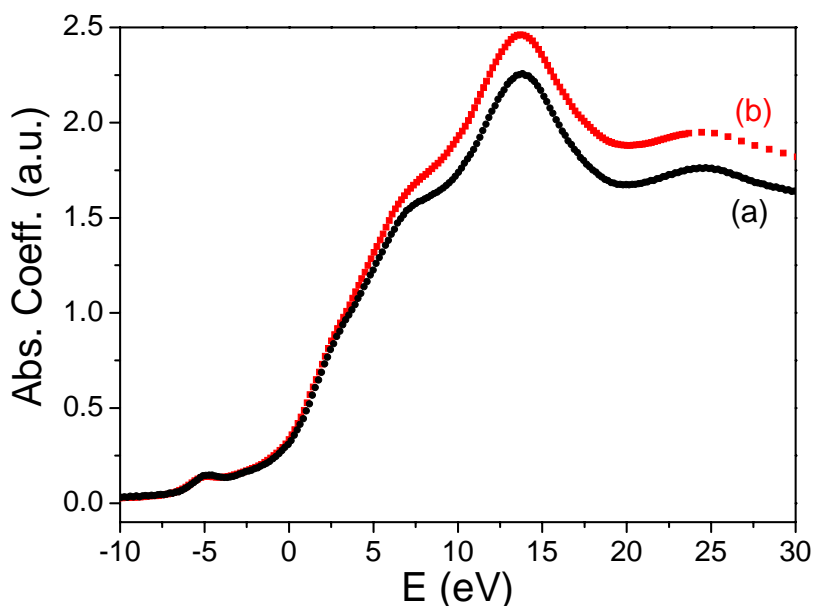


Figure 5. XANES data for (a) bulk Mn_3O_4 and (b) mesoporous Mn_3O_4 .

Conversion of Mn_2O_3 (corundum structure) to Mn_3O_4 (spinel structure) involves a significant loss of oxygen and change of structure from hexagonal to cubic close packing. Such a transformation requires shearing of the AB stacked planes (hcp) to the ABC stacking (ccp). The ability to do so while preserving the mesoporous structure demonstrates that the thin (< 8 nm thick) walls can accommodate the strain of such a structural transformation without severe fracture. The loss of oxygen on transformation results in shrinkage of the walls (i.e. larger pores) while preserving the basic pore shape, further testifying to the flexibility of the mesostructure in its accommodation of structural change.

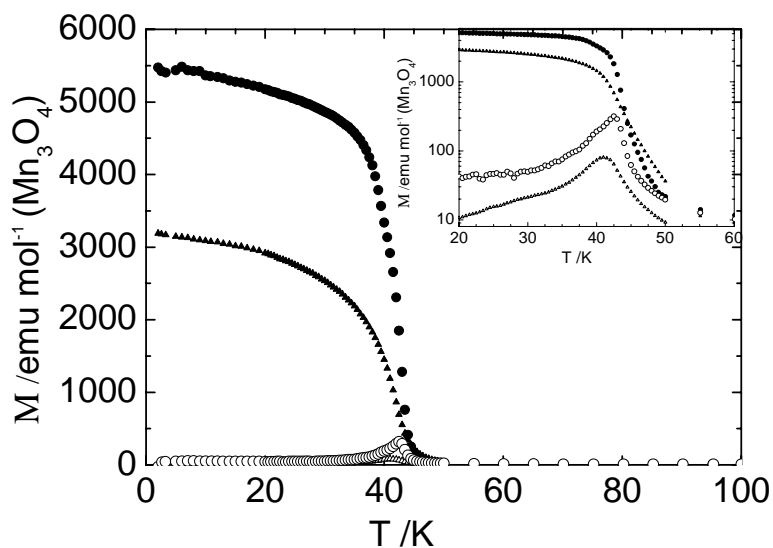


Figure 6. Magnetisation data for the mesoporous Mn_3O_4 with crystalline walls taken in 0.01 T after first cooling in zero field (zfc, open circles) and then in an applied field of 0.01 T (fc, closed circles); the results of the same measurement on bulk Mn_3O_4 with the same heat treatment were shown as triangles with the same distinction between open (zfc) and closed (fc) forms as for the data for the mesoporous sample. The smaller inserted graph depicts the data in greater detail centred around 40 K, with the y-axis on a logarithmic scale to accentuate the zfc behaviour.

The imposition of a mesostructure on a material may influence its magnetic properties, as a result we performed SQUID magnetometry measurements to explore the magnetic properties of mesoporous Mn_3O_4 . Figure 6 displays the susceptibility of the mesoporous Mn_3O_4 as well as bulk Mn_3O_4 (Aldrich, 97%), measured in an applied field of 0.01 T first after cooling in zero field (zfc) and then after cooling in a field of 0.01 T (fc). The bulk material is known to undergo long-range magnetic ordering to a collinear ferrimagnetic array on cooling through $T_c = 42$ K; on further cooling this transforms to a spiral spin structure at 39 K, and finally a canted spin array is formed at 33 K.⁶⁻⁹ Whilst the highest-temperature transition is very distinct in both samples, and there is a hint of a transition at 39 K in the zfc data of the bulk sample, no other transitions are marked by distinct features in Figure 6 in either sample for either fc or zfc data. There are two clear

differences between the two samples apparent in Figure 6: the transition above 40 K is broader for the mesoporous form, and for the zfc data it is centred at a lower temperature; the saturation magnetisation is lower for the mesoporous sample. A simple interpretation of both observations may be based on the greater fraction of manganese atoms at the surface of the mesoporous sample, and the likely lower degree of crystallinity of such samples. The former will reduce the mean exchange field, and perhaps also increase the distribution of sites, with an increasing fraction not possessing the same number of nearest-neighbours with which to undergo magnetic exchange; the latter will also have an influence on the homogeneity of the mean exchange field.

6-2-3 Conclusions

Mesoporous Mn_3O_4 has been successfully synthesized by first synthesizing mesoporous Mn_2O_3 and then converting to mesoporous Mn_3O_4 without destroying the ordered mesostructure. This is also the first synthesis of mesoporous Mn_3O_4 or any reduced mesoporous manganese oxides. Such materials are unlikely to be prepared directly. The preservation of the ordered mesostructure is demonstrated by TEM, N_2 adsorption-desorption, and low-angle PXRD measurements. The structures of the walls were confirmed by HRTEM and wide-angle PXRD analysis and XANES results confirmed the oxidation state of Mn after reduction was +2.67, which is in good agreement with the oxidation state of Mn in Mn_3O_4 . The magnetic properties of mesoporous Mn_3O_4 have been characterized by SQUID measurements.

6-2-4 References

1. Jiao, F.; Harrison, A.; Jumas, J. C.; Chadwick, A. V.; Kockelmann, W.; Bruce, P. G. *J. Am. Chem. Soc.* **2006**, *128*, 5468.
2. Wang, Y. Q.; Yang, C. M.; Schmidt, W.; Spliethoff, B.; Bill, E.; Schuth, F. *Adv. Mater.* **2005**, *17*, 53.
3. Tian, B. Z.; Liu, X. Y.; Solovyov, L. A.; Liu, Z.; Yang, H. F.; Zhang, Z. D.; Xie, S. H.; Zhang, F. Q.; Tu, B.; Yu, C. Z.; Terasaki, O.; Zhao, D. Y. *J. Am. Chem. Soc.* **2004**, *126*, 865.

4. Tian, B. Z.; Liu, X. Y.; Yang, H. F.; Xie, S. H.; Yu, C. Z.; Tu, B.; Zhao, D. Y. *Adv. Mater.* **2003**, *15*, 1370.
5. Jiao, F.; Yue, B.; Zhu, K. K.; Zhao, D. Y.; He, H. Y. *Chem. Lett.* **2003**, *32*, 770.
6. Dwight, K.; Menyuk, N. *Phys. Rev. B* **1960**, *199*, 1470.
7. Jensen, G. B.; Nielsen, O. V. *J. Phys. C* **1974**, *7*, 409.
8. Srinivasan, G.; Seehra, M. S. *Phys. Rev. B* **1983**, *28*, 1.
9. Jacobs, I. S. *J. Phys. Chem. Solids* **1959**, *11*, 1.

6-3 Mesoporous/nanowire low temperature LiCoO₂: synthesis, structural characterization and electrochemical activity

There is much current interest in mesoporous and nanotube/wire metal oxides.¹⁻⁷ The synthesis of such solids, especially the mesoporous materials often requires a templating approach.^{2, 3, 8} Recent advances in the hard silica templating method permits the preparation of porous solids with ordered walls and good thermal stability.^{2, 6, 7, 9-11} However, it is difficult to prepare metal oxides containing alkali metals by such a route because of reaction between the alkali metal and the SiO₂ template.

Here, the first examples of nanowire and mesoporous low temperature LiCoO₂ (LT-LiCoO₂), a Li intercalation compound, are reported. Synthesis involves first preparing mesoporous or nanowire Co₃O₄, then, after hard silica template removal, reacting with a lithium source whilst retaining the nanostructured morphology. Hence, the lithium containing compounds may be prepared by avoiding reaction between the lithium precursor and the silica template, which would occur if the compounds were prepared directly.

6-3-1 Synthesis

Preparation of the mesoporous silica, SBA-15 and KIT-6, has been described in Chapter 2. A typical synthesis of nanostructured LT-LiCoO₂ was as follows: 1 g of Co(NO₃)₂·6H₂O (98%, Aldrich) was dissolved in 20 mL of ethanol, followed by addition of 2 g of mesoporous silica. After stirring at room temperature until all the solution had been absorbed, the sample was heated slowly to 300 °C and calcined at that temperature for 3 h. The impregnation procedure was repeated, followed by calcination at 500 °C for 3 h. The resulting sample was twice treated with a 10% HF solution in water to remove the silica template, followed by washing with water and ethanol several times, and then drying at 60 °C. This procedure leads to mesoporous/nanowire Co₃O₄, discussed previously in Chapter 4-2. To prepare nanostructured LT-LiCoO₂, 0.2 g of the as-prepared mesoporous/nanowire Co₃O₄ were mixed with excess (0.6 g) LiOH·H₂O in 20 mL of ethanol. The solvent was removed by stirring overnight at room temperature, and the mixture calcined at 400 °C for 1 h. The final product was washed with water and ethanol several times to remove the unreacted lithium salt, and dried at 60 °C for 2h.

6-3-2 Structural characterization

LiCoO_2 synthesized at around $800\text{ }^\circ\text{C}$ possesses a layered $\alpha\text{-NaFeO}_2$ structure, whereas synthesis at lower temperatures yields LT-LiCoO_2 , composed predominantly of a spinel structure containing additional lithium, $\text{Li}_2\text{Co}_2\text{O}_4$. The synthesis temperature anticipated LT-LiCoO_2 and this was verified by wide-angle powder X-ray diffraction, Figure 1. Although the diffraction data for HT and LT materials are similar, it is evident, especially on examining the insets in Figure 1, that the material synthesised here is LT-LiCoO_2 . The use of temperatures sufficiently high to promote the formation of HT-LiCoO_2 resulted in a loss of the nanostructure.

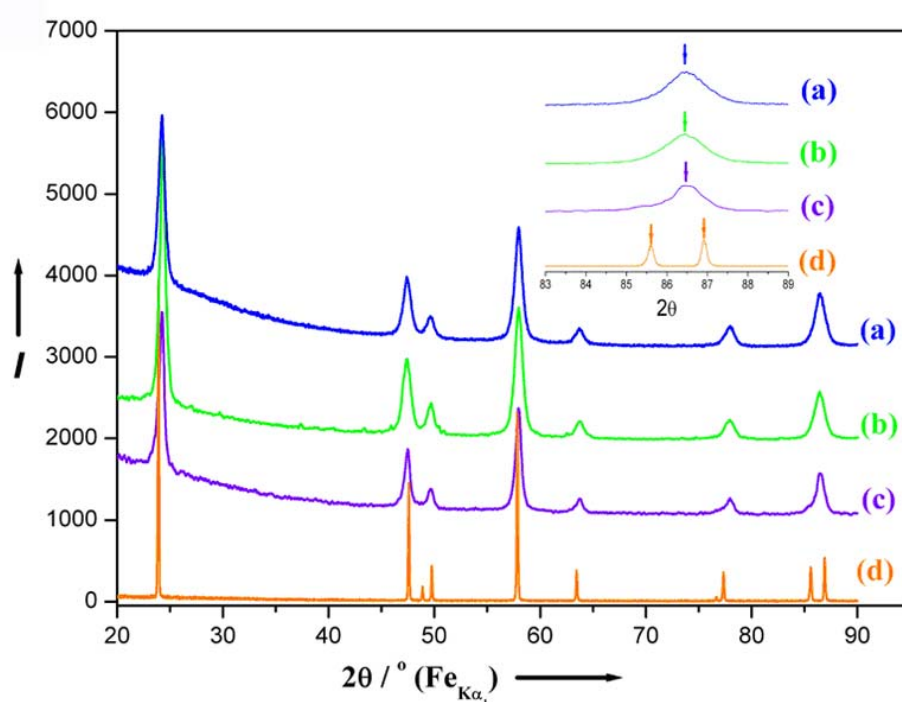


Figure 1. Wide-angle PXR D patterns: (a) LT-LiCoO_2 nanowires; (b) mesoporous LT-LiCoO_2 ; (c) bulk LT-LiCoO_2 ; (d) high temperature LiCoO_2 . Inset is enlarged part of the patterns.

The nanowire morphology of LT-LiCoO_2 prepared from SBA-15 is shown in Figure 2a-c. This morphology dominates throughout the material. Although the wires are continuous, close inspection of high resolution TEM data (Figure 2c) indicate that they are composed of domains that are not structurally coherent. This is different from the single-crystal nature of the Co_3O_4 nanowires. However, importantly, the nanowire morphology of the Co_3O_4 material has been maintained. By TEM analysis, the diameter of LT-LiCoO_2 wires is approximately 10 nm, only slightly larger than the value of 9.5 nm for Co_3O_4 . Turning to mesoporous LT-LiCoO_2 formed from KIT-6, TEM data for this material are shown in Figure 2d-f. It is clear

that the cubic mesoporous Co_3O_4 morphology is maintained and this extends throughout the sample. The diameter of mesoporous LT- LiCoO_2 estimated from the TEM data in shorter dimensions is ~ 8.0 nm, consistent with that for Co_3O_4 (7.8 nm). In contrast to nanowire LT- LiCoO_2 , it is interesting to note that mesoporous LT- LiCoO_2 maintains the single-crystal nature of each particle. The HRTEM image (Figure 2f) indicates the lattice fringes for LT- LiCoO_2 run in the same direction. Further studies will be required to understand the mechanism by which the single crystal structure is maintained during reacting with LiOH.

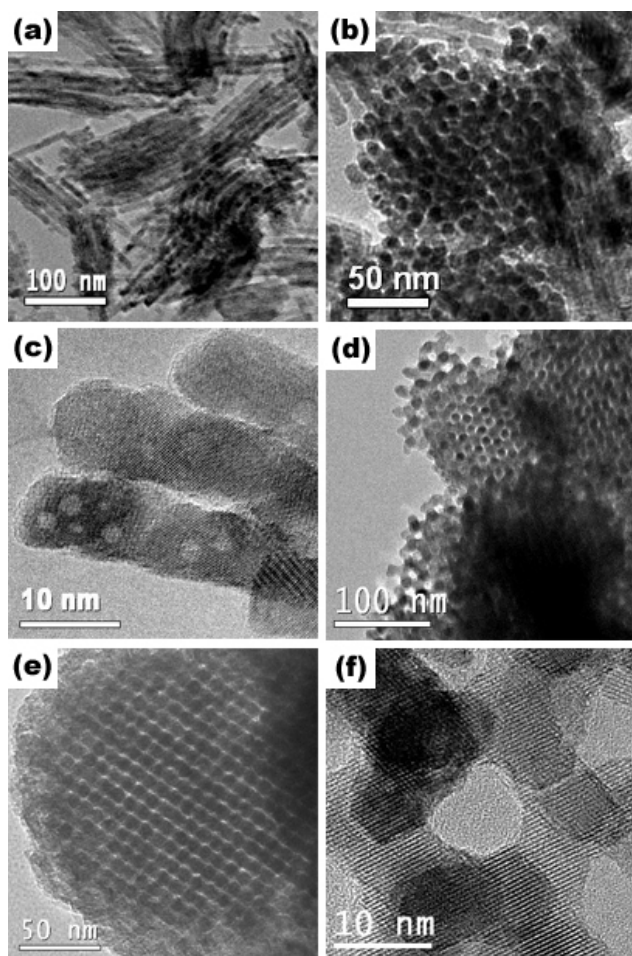


Figure 2. TEM images of LT- LiCoO_2 nanowires: (a) recorded along the wire direction and (b) perpendicular to it; (c) HRTEM image of LT- LiCoO_2 nanowires. TEM images of mesoporous LT- LiCoO_2 : (e) recorded along [111] direction and (f) along [531] direction; (g) HRTEM image of mesoporous LT- LiCoO_2 .

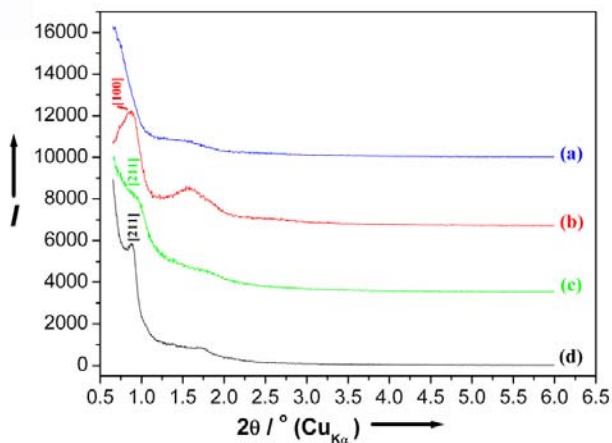


Figure 3. Low-angle PXRD patterns: (a) LT-LiCoO₂ nanowires; (b) Co₃O₄ nanowires; (c) mesoporous LT-LiCoO₂; (d) mesoporous Co₃O₄.

From the TEM data for nanowire LT-LiCoO₂, a lattice parameter a_0 for the hexagonal (P6mm) mesostructure of 108 Å may be obtained. This is in reasonable agreement with the value (117 Å) calculated from the low angle PXRD pattern of the Co₃O₄ nanowires. The low angle PXRD pattern of nanowire LT-LiCoO₂ (Figure 3a) does not possess a well defined peak in the range of 0.6-1.0 degrees, because the nanowire bundles are less well ordered after reaction at 400 °C with LiOH, Figure 2a. In the case of LT-LiCoO₂ formed from KIT-6, a lattice parameter, a_0 , of 226 Å may be extracted for the cubic structure from the TEM data. This is similar to the lattice parameter (235 Å) calculated from the first peak in low angle PXRD pattern of mesoporous LT-LiCoO₂ (Figure 3c). This value is a little smaller than the parameter a_0 for mesoporous Co₃O₄ (241 Å) calculated from Figure 3d. This is due to the pore structure shrinkage accompanying the solid-state reaction.

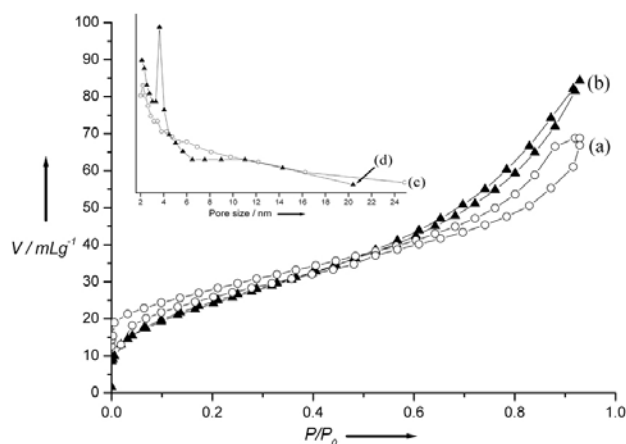


Figure 4. Nitrogen adsorption-desorption isotherms of LT-LiCoO₂: (a) nanowire and (b) mesoporous. The inset shows the pore size distributions of LT-LiCoO₂: (c) nanowire and (d) mesoporous.

N_2 adsorption-desorption isotherms (Figure 4a, b) for both forms of nanostructured LT-LiCoO₂ show type IV isotherms with an H₁ hysteresis loop, confirming the mesoporosity. The specific surface area of nanowire and mesoporous LT-LiCoO₂ estimated from the Brunauer- Emmett-Teller (BET) method is 70 m²g⁻¹ and 92 m²g⁻¹, respectively. In the case of the LT-LiCoO₂ nanowires, the size of the pore between the wires exhibits a wide distribution (Figure 4c, insert), indicating a disordered pore structure, consistent with the absence of a low angle PXRD peak (Figure 3a) and with the TEM images (Figure 2a, b); the more ordered Co₃O₄ nanowires show a narrow distribution around 3.78 nm. The loss of order between the wires in LT-LiCoO₂ may be due to the narrow bridges between the wires breaking up on reaction with LiOH. The N₂ uptake in high relative pressure range confirms the disordered nanostructure. In the case of mesoporous LT-LiCoO₂, the pore size distribution (Figure 4d, insert) is narrow with a peak at 3.67 nm, which is close to the value for mesoporous Co₃O₄ (3.8 nm), consistent with the parameter of the mesostructure for mesoporous LT-LiCoO₂.

6-3-3 Electrochemical properties

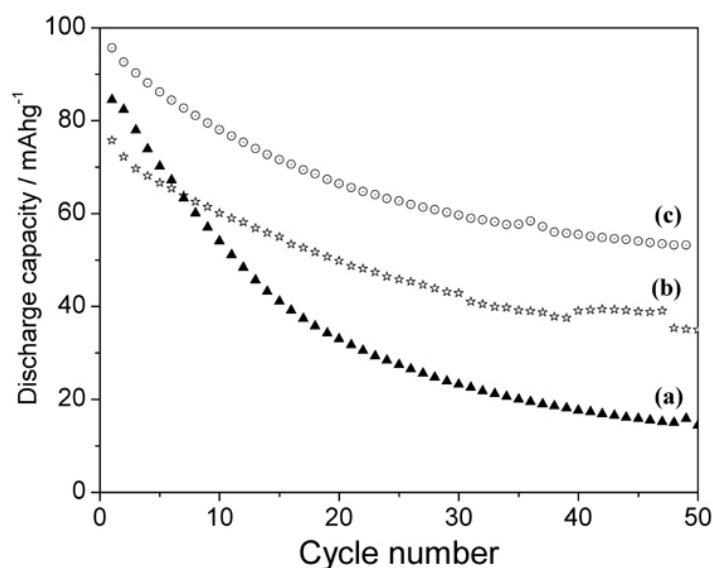


Figure 5. Discharge capacities of (a) bulk LT-LiCoO₂ (▲); (b) LT-LiCoO₂ nanowires (☆); (c) mesoporous LT-LiCoO₂ (⊙).

The electrochemical behaviour of these Li intercalation materials (LT-LiCoO₂) and their comparison with nanoparticles are shown in Figure 5. The surface area of the nanoparticulate LT-LiCoO₂, prepared from CoCO₃ and Li₂CO₃, was 42 m²g⁻¹. The cells were first charged to remove lithium from the electrodes. Figure 5 reports the discharge capacity for the first and subsequent cycles, where cycling was carried out at a constant rate of 30 mA g⁻¹ between potential limits of 3.0 V and 4.2 V. The first discharge capacity for

mesoporous LT-LiCoO₂ is some 20 mAhg⁻¹ higher than the equivalent nanowire material. The initial discharge capacity of normal LT-LiCoO₂ lies between the two nanostructured materials. The fade of discharge capacity on cycling is the same for both nanostructured forms of LT-LiCoO₂, however the fade is markedly less than that of normal LT-LiCoO₂. The capacity of the nanostructured materials reduces by around 45% after 50 cycles whereas this figure is 75% for normal LT-LiCoO₂. The superior capacity retention for the nanostructured materials indicates that the structural transformations that accompany cycling are better accommodated as a result of the nanostructured morphology.

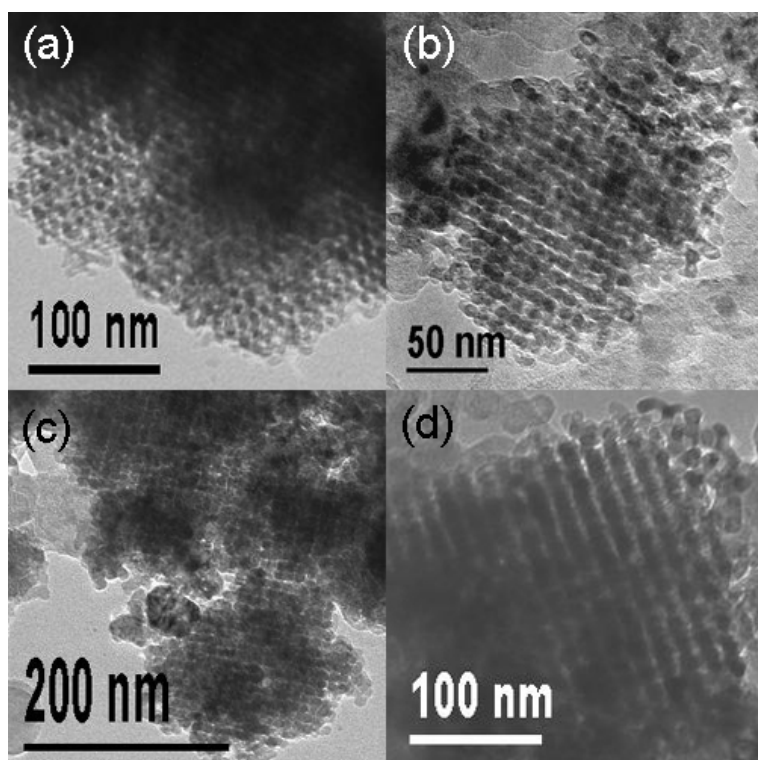


Figure 6. TEM images for mesoporous LT-LiCoO₂ (a-b) after 50 cycles, end of charge; (c-d) after 50 cycles, end of discharge.

Electrode materials were recovered from the cells and re-examined by TEM. The TEM images for mesoporous LT-LiCoO₂ at the states of fully charged and discharged confirm that the ordered mesostructure was maintained after lithium intercalation/deintercalation many times. Although LT-LiCoO₂ is not itself a likely commercial electrode, the flexibility of the mesostructure makes mesoporous Li-containing transition metal oxide important as a positive electrode material for high rate applications.

6-3-4 Conclusions

It has been shown that lithium containing nanostructured materials may be prepared by a hard templating route, by first forming the transition metal oxide and then reacting this

with a lithium source, with preservation of the nanostructure. Both one-dimensional nanowire LT-LiCoO₂ (based on SBA-15) and three-dimensional mesoporous LT-LiCoO₂ (based on KIT-6) have been synthesized with highly crystalline structures. Electrochemical data demonstrates that the mesostructured materials exhibit superior capacity retention on cycling compared with nanoparticulate LT-LiCoO₂. TEM data confirm the maintenance of ordered mesopores after 50 cycles.

6-3-5 References

- ¹ A. S. Arico, P. Bruce, B. Scrosati, J. M. Tarascon, and W. Van Schalkwijk, *Nature Materials*, 2005, **4**, 366.
- ² B. Z. Tian, X. Y. Liu, L. A. Solovyov, Z. Liu, H. F. Yang, Z. D. Zhang, S. H. Xie, F. Q. Zhang, B. Tu, C. Z. Yu, O. Terasaki, and D. Y. Zhao, *Journal of the American Chemical Society*, 2004, **126**, 865.
- ³ F. Jiao and P. G. Bruce, *Angewandte Chemie-International Edition*, 2004, **43**, 5958.
- ⁴ M. Antonietti and G. A. Ozin, *Chemistry-a European Journal*, 2004, **10**, 29.
- ⁵ Y. N. Xia, P. D. Yang, Y. G. Sun, Y. Y. Wu, B. Mayers, B. Gates, Y. D. Yin, F. Kim, and Y. Q. Yan, *Advanced Materials*, 2003, **15**, 353.
- ⁶ B. Z. Tian, X. Y. Liu, H. F. Yang, S. H. Xie, C. Z. Yu, B. Tu, and D. Y. Zhao, *Advanced Materials*, 2003, **15**, 1370.
- ⁷ F. Jiao, B. Yue, K. K. Zhu, D. Y. Zhao, and H. Y. He, *Chemistry Letters*, 2003, **32**, 770.
- ⁸ P. D. Yang, D. Y. Zhao, D. I. Margolese, B. F. Chmelka, and G. D. Stucky, *Nature*, 1998, **396**, 152.
- ⁹ F. Jiao, A. Harrison, J. C. Jumas, A. V. Chadwick, W. Kockelmann, and P. G. Bruce, *Journal of the American Chemical Society*, 2006, **128**, 5468.
- ¹⁰ Y. Q. Wang, C. M. Yang, W. Schmidt, B. Spliethoff, E. Bill, and F. Schuth, *Advanced Materials*, 2005, **17**, 53.
- ¹¹ F. Jiao, K. M. Shaju, and P. G. Bruce, *Angewandte Chemie-International Edition*, 2005, **44**, 6550.

Chapter 7 Ordered three-dimensional arrays of monodispersed Mn₃O₄ nanoparticles with a core-shell structure

Only a few three dimensionally ordered transition metal oxide nanoparticulate arrays, such as Fe₃O₄, Fe₂O₃, and CoO, have been reported previously.¹⁻⁷ Manganese oxides, are particularly important because they find uses in many applications.^{1, 4, 7} Important earlier work demonstrated that monodispersed manganese oxides, MnO and Mn₃O₄, with a regular shape and narrow particle size distribution, could be prepared.^{1,4,7} However, there are no reports of three-dimensionally ordered Mn₃O₄ arrays. Here, the first synthesis of monodispersed Mn₃O₄ nanoparticles that spontaneously self assemble into three-dimensional ordered arrays with cubic symmetry is demonstrated. Furthermore, these particles possess a core-shell structure composed of a core of Mn₃O₄ surrounded by a thin shell of MnO₂. The core-shell structure has a profound effect on the magnetic properties of the Mn₃O₄ nanoparticles which show behaviour similar to that of a spin-glass rather than the anticipated superparamagnetism for nanoparticles.⁴

The higher surface area to volume ratio of nanoparticles compared with particles of micron dimensions makes the presence of a core-shell structure of much greater significance for the physical properties of nanomaterials compared with their bulk counterparts. However, the techniques that are invariably used to characterize nanomaterials; transmission electron microscopy, powder X-ray diffraction and N₂ adsorption, are not well suited to identify a shell, especially if thin or amorphous. Characterizing core-shell structures presents a greater challenge, necessitating the use of a combination of bulk and surface methods. While the deliberate synthesis of core-shell structured nanoparticles is often difficult, it is conversely true that the dominance of TEM and PXRD as characterization tools for nanomaterials may have resulted in core-shell structures going undetected. Indeed, a re-examination of nanoparticulate materials, especially where physical properties may have proved difficult to interpret based on homogeneous nanoparticles, is to be recommended.

7-1 Experimental section

The procedure for synthesizing Mn₃O₄ nanoparticles was developed by modifying a procedure reported previously.⁴ In a typical synthesis, a mixture of 1 gram (3.74 mmol)

of Mn (II) (acetylacetonate)₂ (Aldrich) and 20 ml of the alkyl amine, oleylamine ($\geq 70\%$, Fluka), was placed in a 3-neck 250 ml flask and heated rapidly (15 min to 210 °C) with continuous stirring under air. The colour of the mixture turned from yellow to dark brown. The temperature was maintained at 210 °C for 5 h and the mixture then cooled to room temperature. Following addition of 30 ml of ethanol the product was centrifuged and the liquid separated off. This process was repeated twice to remove the remaining unreacted surfactant. The final product was again dispersed in 10 ml of ethanol in an ultrasonic bath for 3 minutes, followed by drying at 50°C for 2 days.

The isolated particles and the arrays were examined by TEM. In the former case, a small amount of powder was dispersed in hexane and the mixture dropped onto a carbon coated TEM grid, followed by evaporation of the hexane at room temperature. In the latter case, a small amount of powder was lightly ground with some ethanol and then a drop of the mixture was placed on the TEM grid.

The XPS data were collected using a VG ESCALAB II spectrometer with an operating pressure of 1×10^{-9} mbar and unmonochromatised AlK_{α} radiation (1486.6 eV). The sample area was of 3 mm diameter. Peaks were recorded with a constant step energy of 0.05 eV, and a pass energy of 20 eV. The binding energy scale was calibrated with the C1s line of carbon at 284.6 eV.

7-2 Results and discussion

Mn₃O₄ nanoparticles, prepared as described in the experimental section, were examined by TEM (Figure 1). The monodispersity of the particle size is evident in Figure 1a and is repeated throughout the entire sample. The particles have an average size of 7.8 ± 0.5 nm, based on TEM analysis. High-resolution TEM (HRTEM) studies of individual particles (Figure 1b) revealed their single crystal nature and the lattice spacings marked on the figure correspond well with the [200] and [103] d-spacings, 0.288 nm and 0.277 nm respectively, obtained for Mn₃O₄ from the JCPDS database (JCPDS No. 24-734). Selected area electron diffraction (SAED) (Figure 1d, inset) shows clear diffraction rings, which can be indexed on the Mn₃O₄ spinel structure, in agreement with the HRTEM results. Although no surface layer/coating on the Mn₃O₄ nanoparticles could be unambiguously observed by HRTEM analysis, evidence that the surface of Mn₃O₄

nanoparticles are coated with a thin MnO_2 layer, i.e. the particles have a core-shell structure, is discussed later.

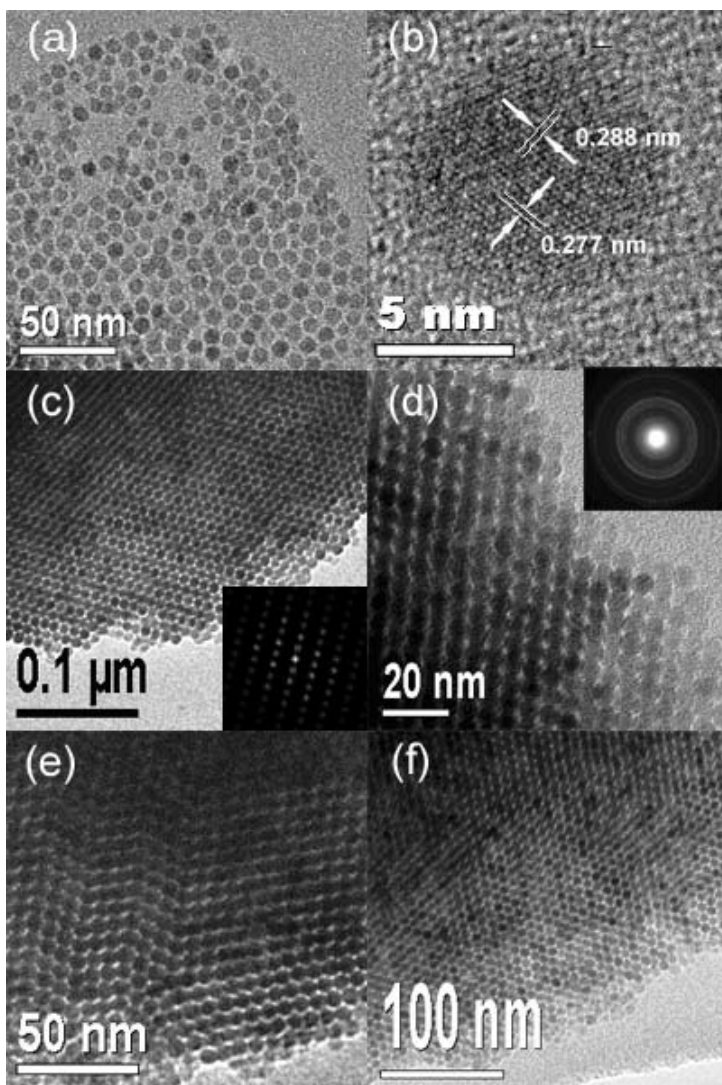


Figure 1. TEM images for (a) isolated Mn_3O_4 nanoparticles, (b) HRTEM image for a single Mn_3O_4 nanoparticle, (c) and (d) shows TEM images recorded from different regions of highly ordered Mn_3O_4 nanoparticle arrays. Fourier transform image of (c) is shown in (c) inset. SAED pattern is shown in (d) inset.

The formation of monodispersed nanoparticles depends on controlling the process of nucleation and growth. Monodispersity can be induced by ensuring homogeneous nucleation followed by diffusion controlled growth. Heating $\text{Mn}(\text{acac})_2$ in air at 210°C , but in the absence of the oleylamine resulted in large Mn_3O_4 particles, distributed over a range of particle sizes, thus confirming that the alkyl amine plays a critical role in

forming monodispersed nanoparticles.⁸ Heating $\text{Mn}(\text{acac})_2$ to its decomposition temperature while being vigorously stirred in oleylamine ensured multiple nucleation. Diffusion of growth species through the highly viscous oleylamine solution to the many growing crystallites will be slow, thus limiting crystallite growth. These conditions are favourable for the growth of monodispersed particles, as observed.

Examination of the Mn_3O_4 material without dispersion in hexane revealed that the Mn_3O_4 particles had spontaneously self-assembled into highly ordered three-dimensional close packed arrays, Figures. 1c-f and Figure 1c inset. Studying the arrays from different directions established that the predominant symmetry adopted by close packing the approximately spherical particles was cubic, although there is clear evidence of stacking faults and even some minor regions which exhibit hexagonal packing (Figure 1e-f). Although energetics clearly dictate that the spherical particles adopt a close packed arrangement, there is no evidence for alignment of the crystallographic directions between different particles, as is evident in the selected area electron diffraction, insert Figure 1d, which exhibits powder diffraction like rings, not single crystal behaviour. Examination of many regions of the material demonstrated that the 3D ordered arrays exist throughout.

Confirmation that the material is Mn_3O_4 , with the normal spinel structure, was obtained by powder X-ray diffraction, Figure 2. Excellent agreement between the diffraction pattern for the nanocrystalline arrays and bulk Mn_3O_4 is evident. The peaks associated with the former pattern are of course broader due to the smaller particle size. Application of the Sherrer formula relating peak width to the particle size, gave a value for the latter of 8.1 nm, in good agreement with the value obtained from TEM data (7.8 nm). Note that the Sherrer formula assumes isotropic particles, an assumption that is accurate in the case of the cubic spinel.

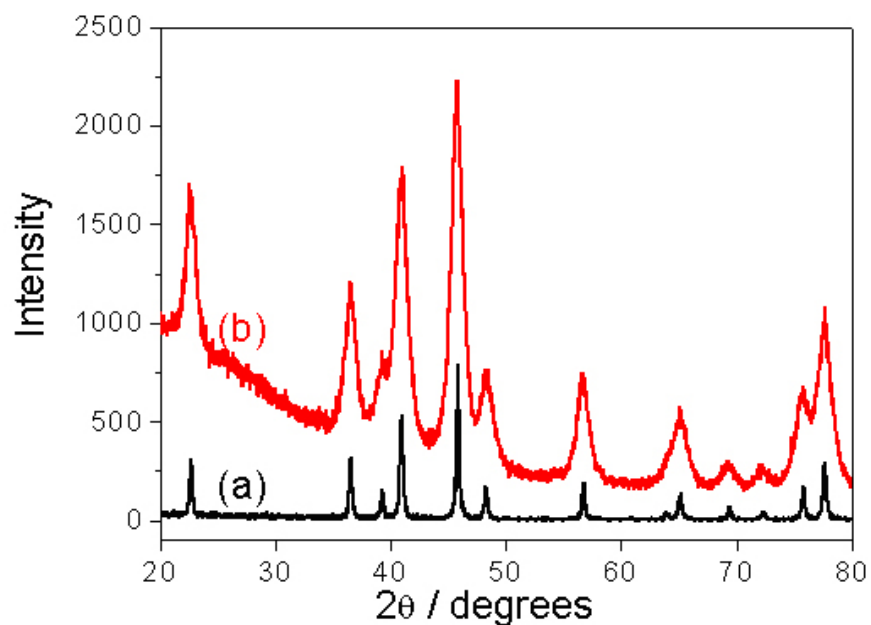


Figure 2. PXRD patterns for (a) bulk Mn_3O_4 and (b) Mn_3O_4 nanoparticle array.

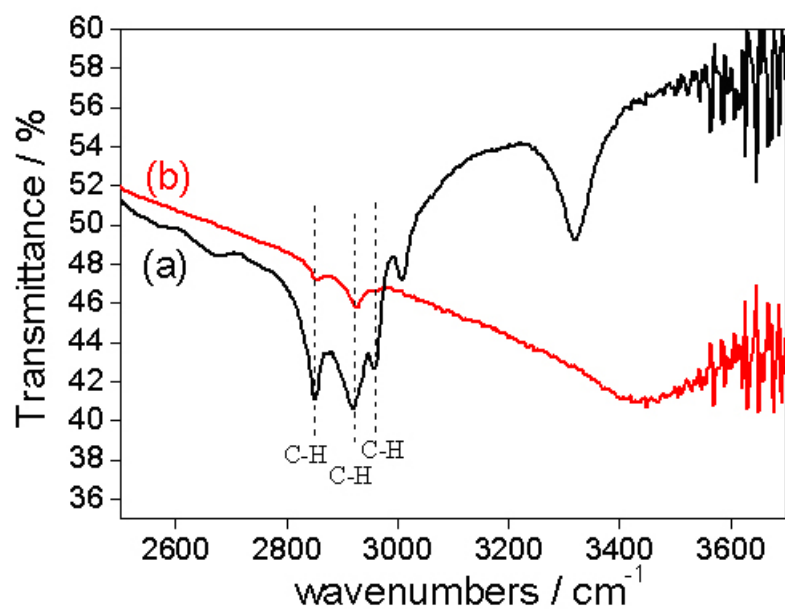


Figure 3. FTIR spectra for (a) oleylamine and (b) Mn_3O_4 nanoparticle array.

The ease with which the arrays could be dispersed in non-polar solvents, such as hexane, suggested that the surface of the particles was capped by the alkyl amine surfactant, thus presenting a hydrophobic exterior. To investigate this, FTIR spectra were collected on the array, as shown in Figure 3, which also includes the spectrum of the oleylamine for comparison. Examination of these results revealed that the major peaks of the oleylamine are also present in the spectrum collected from the array, consistent with

the presence of the alkyl amine on the surface of the particles. Whereas the C-H vibrations of the oleylamine and the array match very well, there is a shift in the NH₂ vibrations from 3319cm⁻¹ for the oleylamine to 3446cm⁻¹ for the Mn₃O₄ array.⁹⁻¹¹ Such a shift is consistent with co-ordination of the Mn by the NH₂ group of the alkyl amine, similar shifts have been noted for other alkyl amine based ligands coordinating transition metal ions.¹¹ Further confirmation for the presence of the alkyl amine in the array was obtained by CHN analysis, which yielded an N content of 0.56 wt%.

The dc magnetisation measurements on the Mn₃O₄ array, Figure 4, revealed some form of magnetic transition a little above 40 K: there is a splitting of the fc and zfc response below about 44(1) K, and the zfc data show a maximum at 36.0 K. Bulk Mn₃O₄ is known to order magnetically at T_c = 42 K to produce a collinear ferrimagnetic array and then on further cooling, a spiral spin structure followed by a canted spin array.¹²⁻¹⁴ Nanoparticulate forms of the material also show a spontaneous moment below a blocking temperature, T_B, somewhat lower than 42 K.⁴ Values of 36, 40 and 41K have been reported for T_B for particle sizes of 6, 10 and 15 nm respectively.⁴

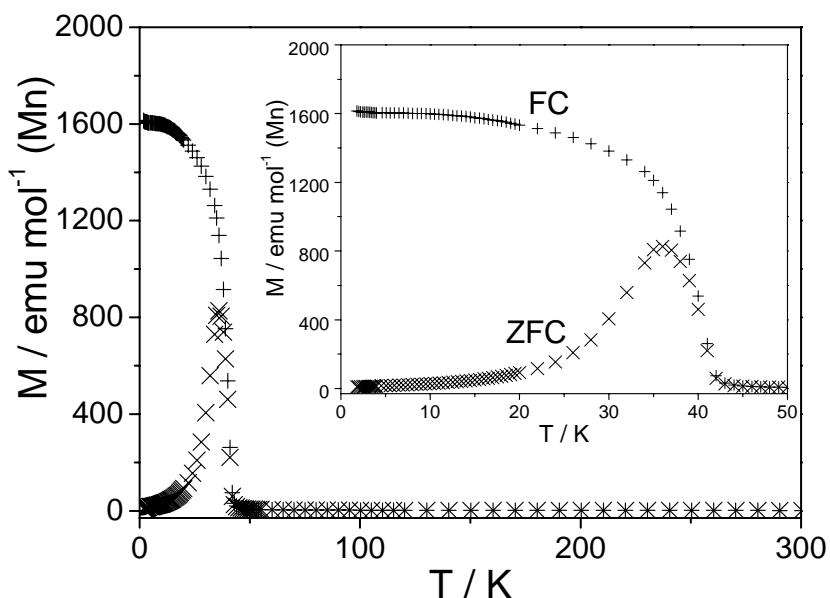


Figure 4. DC magnetisation of Mn₃O₄ nanoparticles measured after cooling in zero field (zfc, ×) then in a field of 0.01 T (fc, +). The inset reveals the responses near the fc-zfc splitting in greater detail.

Given that the present work represents the first report of a 3D array of Mn_3O_4 nanoparticles, it is interesting to investigate whether there is any evidence that the nanoparticles are magnetically isolated (in which case superparamagnetism is anticipated) or if there is magnetic interaction between them (especially if the surface coverage by the alkyl amine was incomplete). Here the AC susceptibility provides further insight. Figure 5 shows the change in the real part of the ac susceptibility with probe frequency, ν , and temperature, revealing an increase in T_B as ν increases.

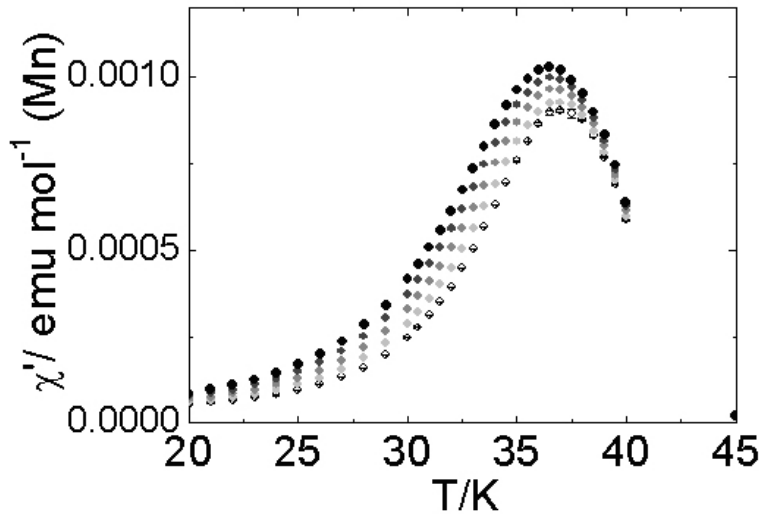


Figure 5. Real part of the AC susceptibility of the Mn_3O_4 nanoparticle array measured at frequencies ranging from 1 Hz (closed circles) through 6, 40 and 250 to 1588 Hz (open circles).

The relation between T_B and ν for a superparamagnet is expected to exhibit an Arrhenius form:^{15, 16}

$$\nu = \nu_0 \cdot \exp(-E_a/RT_B)$$

where ν_0 is a characteristic relaxation time, commonly in the range 10^{-9} - 10^{-13} s for isolated, superparamagnetic particles, and E_a is usually considered to relate to an activation barrier for magnetization reversal. A least-squares fit to this relation is displayed in Figure 6, which shows the relation between $\ln \nu$ and $1/T_B$, where T_B corresponds to the maximum in χ' . Optimized parameters are $\nu_0 = 10^{178(4)}$ s and $E_a/R = 17620$ (394) K. Both these are unphysical for a superparamagnet; rather, they are compatible with those found in spin glass systems, and interacting magnetic nanoparticles.^{17, 18}

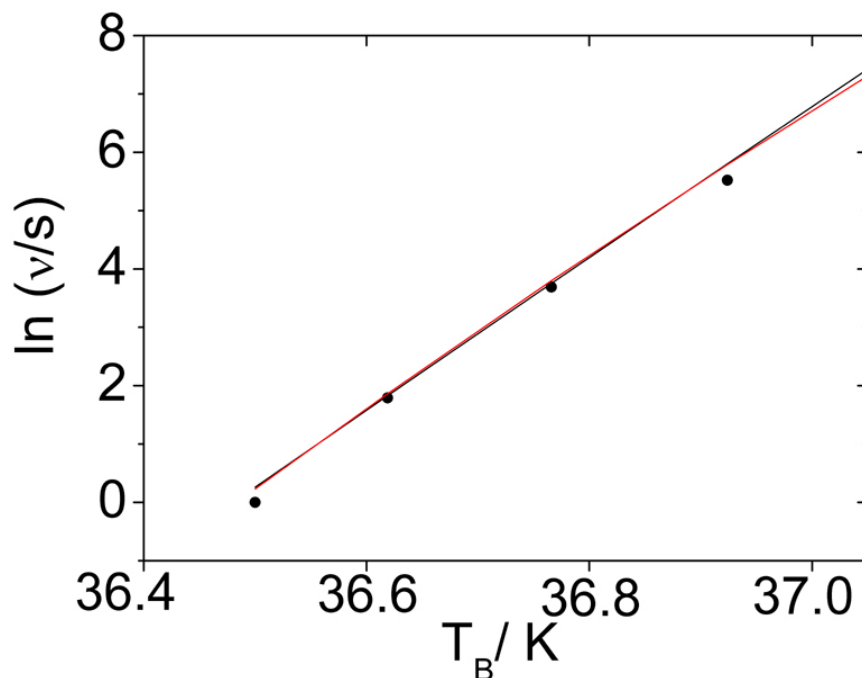


Figure 6. Relation between the frequency of the measurement, ν , and the blocking temperature, T_B , with a least-squares fit to an Arrhenius expression (black line) and Vogel-Fulcher Law (red line).

The frequency dependence of T_B for such systems is most commonly analyzed using the phenomenological Vogel-Fulcher expression, which is taken from the glass literature:

$$\nu = \nu_0 \cdot \exp(-E_a/R(T_B - T_0))$$

The parameter T_0 is sometimes taken to represent the inter-particle coupling strength, and is smaller – usually considerable smaller – than T_B .¹⁸ Least-squares fitting of this expression for the data taken on the array, Figure 6, revealed a very strong correlation between the variables ν_0 , E_a and T_0 , though the following values were found for a free fit of all variables: $\nu_0 = 10^{35(1)}$ s, $E_a/R = 625(13)$ K and $T_0 = 29(7)$ K. Physically reasonable values of ν_0 and E_a/R are only found when T_0 approaches T_B , indicating that the magnetic forces acting on the particles are comparable in strength to those within the particles. It is unlikely that such forces could arise from coupling between the particles, given the surface coating of amines, but it could indicate coupling between a core of Mn_3O_4 , and a shell of a chemically modified form of the core material. The PXRD,

HRTEM and SAED results revealed no evidence for any other crystalline material except Mn_3O_4 .

To investigate whether a shell of different material is present, X-ray photoelectron spectroscopy (XPS) was carried out. Bulk Mn_3O_4 and $\beta\text{-MnO}_2$ were also measured for comparison. The Mn 2p_{3/2}, Mn 2p_{1/2}, and O 1s binding energies for all three samples are shown in Table 1. It is evident that the manganese atoms at the surface of the Mn_3O_4 nanoparticle array have binding energies close to those of bulk MnO_2 , instead of bulk Mn_3O_4 . A peak associated with the N 1s arising from the RNH_2 molecules on the surface was also observed. We propose that the particles are composed of a core of Mn_3O_4 encapsulated in a shell of MnO_2 to which the RNH_2 molecules are attached. Given that the MnO_2 shell is not observed by PXRD, SAED or HRTEM, we conclude that the MnO_2 layer must be thin (<1 nm) and anticipated to be disordered. As a result, the shell is likely to have significant degrees of spin disorder and also to couple to the core phase through significant superexchange interactions. An increasing number of magnetic core-shell systems, or granular materials, with similar types of components are being characterized, and are generally found to have some degree of spin-glass character as discussed here.¹⁹⁻

21

Samples	peak position / eV		
	Mn 2p ^{3/2}	Mn 2p ^{1/2}	O 1s
bulk Mn_3O_4	641.2	652.7	529.6
bulk $\beta\text{-MnO}_2$	642.5	653.9	529.5
Mn_3O_4 nanoparticle array	642.2	653.7	530.1

Table 1. XPS binding energy for bulk Mn_3O_4 , bulk $\beta\text{-MnO}_2$ and Mn_3O_4 nanoparticle array.

7-3 Conclusions

An ordered (predominantly cubic) three-dimensional array of monodispersed Mn_3O_4 nanoparticles (diameter ~ 8 nm) with a core-shell structure has been prepared for the first time, and by a one-step thermal decomposition of $\text{Mn}(\text{acac})_2$ in oleylamine. PXRD, HRTEM, and XPS results confirmed that these particles have a highly crystalline Mn_3O_4 core encapsulated within a thin shell of MnO_2 . FTIR data indicate that the shell is

capped by oleylamine. The self-assembled three-dimensional arrays exhibit interesting behaviour similar to a spin-glass material rather than the anticipated superparamagnetic behaviour for isolated nanoparticles. Such a difference may be due to the strong interaction between core (Mn_3O_4) and shell (MnO_2).

7-4 References

- ¹ S. L. Brock, O. Giraldo, S. L. Suib, D. Potter, V. Urban, P. Thiyagarajan, and T. Ressler, *Abstracts of Papers of the American Chemical Society*, 1998, **216**, 015.
- ² J. W. Cheon, N. J. Kang, S. M. Lee, J. H. Lee, J. H. Yoon, and S. J. Oh, *Journal of the American Chemical Society*, 2004, **126**, 1950.
- ³ M. D. Mukadam, S. M. Yusuf, P. Sharma, and S. K. Kulshreshtha, *Journal of Magnetism and Magnetic Materials*, 2004, **272-76**, 1401.
- ⁴ W. S. Seo, H. H. Jo, K. Lee, B. Kim, S. J. Oh, and J. T. Park, *Angewandte Chemie-International Edition*, 2004, **43**, 1115.
- ⁵ P. Wang, S. M. Zakeeruddin, R. Humphry-Baker, J. E. Moser, and M. Gratzel, *Advanced Materials*, 2003, **15**, 2101.
- ⁶ J. Y. Ying, C. P. Mehnert, and M. S. Wong, *Angewandte Chemie-International Edition*, 1999, **38**, 56.
- ⁷ Y. N. Xia, P. D. Yang, Y. G. Sun, Y. Y. Wu, B. Mayers, B. Gates, Y. D. Yin, F. Kim, and Y. Q. Yan, *Advanced Materials*, 2003, **15**, 353.
- ⁸ M. F. Casula, Y. W. Jun, D. J. Zaziski, E. M. Chan, A. Corrias, and A. P. Alivisatos, *Journal of the American Chemical Society*, 2006, **128**, 1675.
- ⁹ M. Rajamathi, M. Ghosh, and R. Seshadri, *Chemical Communications*, 2002, 1152.
- ¹⁰ M. J. Hostetler, J. J. Stokes, and R. W. Murray, *Langmuir*, 1996, **12**, 3604.
- ¹¹ S. Mandal, S. R. Sainkar, and M. Sastry, *Nanotechnology*, 2001, **12**, 358.
- ¹² G. B. Jensen and O. V. Nielsen, *J. Phys. C*, 1974, **7**, 409.
- ¹³ K. Dwight and N. Menyuk, *Phys. Rev. B*, 1960, **199**, 1470.
- ¹⁴ I. S. Jacobs, *J. Phys. Chem. Solids*, 1959, **11**, 1.
- ¹⁵ L. Neel, *Ann. Geophys.*, 1949, **5**, 99.
- ¹⁶ W. F. Brown, *Phys. Rev.*, 1963, **130**, 1677.

- ¹⁷ J. L. Dormann, J. R. Cui, and C. Sella, *Journal of Applied Physics*, 1985, **57**, 4283.
- ¹⁸ S. Shtrikman and E. P. Wohlfarth, *Physics Letters A*, 1981, **85**, 467.
- ¹⁹ S. Gangopadhyay, G. C. Hadjipanayis, B. Dale, C. M. Sorensen, K. J. Klabunde, V. Papaefthymiou, and A. Kostikas, *Physical Review B*, 1992, **45**, 9778.
- ²⁰ A. Hernando, *Journal of Physics-Condensed Matter*, 1999, **11**, 9455.
- ²¹ N. S. Gajbhiye and S. Bhattacharyya, *Nanotechnology*, 2005, **16**, 2012.

Chapter 8 Conclusions

The first examples of two-dimensionally and three-dimensionally ordered mesoporous Fe_2O_3 with amorphous walls have been synthesized using decylamine as template and iron (3+) ethoxide as precursor. N_2 adsorption-desorption and HRTEM data show that the walls of both materials are highly microporous. Mössbauer data indicate both materials show superparamagnetic behaviour.

The hard templating method offers a novel approach to synthesize mesoporous transition metal oxides with highly crystalline walls. Mesoporous $\alpha\text{-Fe}_2\text{O}_3$, Co_3O_4 , $\beta\text{-MnO}_2$, and Mn_2O_3 with highly crystalline walls and ordered mesoporous structures have been prepared for the first time by using the hard templating method based on mesoporous silicas (SBA-15 and KIT-6) as the hard templates.

The magnetic behaviour of mesoporous $\alpha\text{-Fe}_2\text{O}_3$ with crystalline walls is unique and different from mesoporous $\alpha\text{-Fe}_2\text{O}_3$ with disordered/amorphous walls and nanoparticles with a size less than 8 nm. Mesoporous $\alpha\text{-Fe}_2\text{O}_3$ with disordered walls and nanoparticulate $\alpha\text{-Fe}_2\text{O}_3$ exhibit no long range magnetic order, absence of a Morin transition and the presence of superparamagnetic behaviour. Despite the wall thickness of mesoporous $\alpha\text{-Fe}_2\text{O}_3$ with crystalline walls being less than 8 nm, long range magnetic ordering persists due to interactions between Fe^{3+} ions along the walls. The material exhibits weakly ferromagnetic susceptibility and Bragg peaks in the powder neutron diffraction data corresponding exactly to the WF phase of bulk $\alpha\text{-Fe}_2\text{O}_3$. However, the confined dimensions are sufficient to suppress the Morin transition present in bulk $\alpha\text{-Fe}_2\text{O}_3$.

It has been shown that mesoporous $\beta\text{-MnO}_2$ with crystalline walls can accommodate reversibly a large amount of lithium (0.92 Li/Mn) on intercalation, with 81% capacity retention on increasing the rate 20 fold after 50 cycles. This is in a sharp contrast with bulk crystalline $\beta\text{-MnO}_2$ which accommodates little or no Li on electrochemical intercalation. The ordered mesoporous structure is preserved on cycling as is the $\beta\text{-MnO}_2$ (rutile) crystal structure of the walls, unlike chemical intercalation into bulk $\beta\text{-MnO}_2$ or electrochemical reaction with nanoparticulate $\beta\text{-MnO}_2$, both of which convert rapidly to LiMn_2O_4 spinel. The origin of this behaviour lies in the ability of the

thin walls (< 8 nm) walls to accommodate the strain of the significant structure expansion on Li intercalation without having to change structure from rutile to spinel.

Both hard and soft templating methods have their limits. By introducing post-templating reactions, the first examples of mesoporous Fe_3O_4 , $\gamma\text{-Fe}_2\text{O}_3$ and Mn_3O_4 have been prepared by reducing template free mesoporous Fe_2O_3 and Mn_2O_3 in a H_2 atmosphere, thus converting the walls from Fe_2O_3 and Mn_2O_3 to the spinels Fe_3O_4 and Mn_3O_4 respectively, without affecting the mesostructure. Such post-templating method offers an alternative approach to synthesize novel nanostructured materials that are difficult to prepare directly. By extending this philosophy, the first example of lithium containing mesoporous transition metal oxides, LT- LiCoO_2 , was prepared by synthesizing mesoporous Co_3O_4 , then reacting with LiOH to avoid the reaction with the silica template. Electrochemical data demonstrated that mesoporous LT- LiCoO_2 exhibits superior electrochemical behaviour compared with nanoparticulate LT- LiCoO_2 .

Nanoparticulate Mn_3O_4 arrays with a core-shell structure have been synthesized using oleylamine as surfactant by a thermal decomposition method. The nanoparticles with a core of crystalline Mn_3O_4 and a shell of MnO_2 (particle size 7 nm) were shown to self-assemble into three-dimensional ordered arrays. Unique magnetic properties have been demonstrated. The material exhibits a spin-glass like behaviour rather than the superparamagnetic behaviour, expected for nanoparticulate Mn_3O_4 .

Publication List

- [1] Factors Influencing the Rate of the Fe_2O_3 Conversion Reaction
F. Jiao, J. L. Bao, P. G. Bruce, *Electrochem. Solid-state Lett.* **2007**, *10*, A264.
- [2] Mesoporous Mn_2O_3 and Mn_3O_4 with crystalline walls
F. Jiao, A. Harrison, A. H. Hill, P. G. Bruce, *Adv. Mater.* **2007**, *19*, 4063.
- [3] Ordered three-dimensional arrays of monodispersed Mn_3O_4 nanoparticles with a core-shell structure and spin-glass behaviour
F. Jiao, A. Harrison, P. G. Bruce, *Angew. Chem. Int. Ed.* **2007**, *46*, 3946.
- [4] Mesoporous crystalline $\beta\text{-MnO}_2$ a reversible positive electrode for rechargeable lithium batteries
F. Jiao, P. G. Bruce, *Adv. Mater.* **2007**, *19*, 657.
- [5] Mesoporous and nanowire Co_3O_4 as negative electrodes for rechargeable lithium batteries
K. M. Shaju, F. Jiao, A. Debart, P. G. Bruce, *Phys. Chem. Chem. Phys.* **2007**, *9*, 1837.
- [6] Mesoporous solids synthesized by post-template reduction/oxidation: ordered mesoporous Fe_3O_4 and $\gamma\text{-Fe}_2\text{O}_3$ with crystalline walls
F. Jiao, J. C. Jumas, M. Womes, A. V. Chadwick, A. Harrison, P. G. Bruce, *J. Am. Chem. Soc.* **2006**, *128*, 12905.
- [7] Ordered mesoporous Fe_2O_3 with crystalline walls
F. Jiao, A. Harrison, J. C. Jumas, A. V. Chadwick, W. Kockelmann, P. G. Bruce, *J. Am. Chem. Soc.* **2006**, *128*, 5468.
- [8] Synthesis of nanowire and mesoporous low temperature LiCoO_2 by a post templating reaction
F. Jiao, K. M. Shaju, P. G. Bruce, *Angew. Chem. Int. Ed.* **2005**, *44*, 6550.
- [9] Two and Three Dimensional Mesoporous Iron Oxides with Microporous Walls
F. Jiao, P. G. Bruce, *Angew. Chem. Int. Ed.* **2004**, *43*, 5958.

List of Abbreviations and Acronyms

PXRD, powder X-ray diffraction

TEM, transmission electron microscopy

SBA-15, a type of mesoporous silica with one dimensional pore structure

KIT-6, a type of mesoporous silica with three dimensional pore structure

LT-LiCoO₂, low temperature form LiCoO₂